UNIVERSITÉ LIBRE DE BRUXELLES

Faculté des sciences

Laboratoire de glaciologie

ULB

The Dynamics of Ice as seen by interferometric SAR: A case study of Antarctic Ice Shelves in Dronning Maud Land ?

Mémoire présenté par

Sophie BERGER

en vue de l'obtention du grade académique de

Master en Sciences et Gestion de l'Environnement,

Finalité Sciences de l'Environnement

Promoteur : Prof F. Pattyn

Co-promoteur : Dr R. Drews

Année académique : 2012 – 2013

Abstract

Ice shelves, which are mainly found in Antarctica consist of floating extensions of ice sheets. They provide an interface for the interactions between the ice sheet and the ocean. Although they present their own flow dynamics, ice shelves remain attached to the grounded ice, thus regulate ice discharge of the ice sheet into the ocean. The control ice shelves exert on inland ice is called the *Buttressing effect*. A mass loss of ice shelves induces a loss of buttressing, which enables a greater discharge of ice into the ocean and contributes to the sea level rise. In a warming world, studying ice shelves and their dynamics become essential if we want to quantify the Antarctic contribution to the future sea level rise.

This thesis is a satellite-based SAR interferometry study of the ice shelves in the region of Dronning Maud Land, Antarctica. SAR interferometry (InSAR) is an imaging technique that compares phase information from images taken at different times to measure surface displacements between the different acquisitions. Based on SAR data from the ERS 1/2 tandem mission (1995-1996), an horizontal flowfield covering the Roi Baudouin Ice shelf was computed with a 50m resolution. Shear-strain rates were also derived from the flowfield. Results show that the *pinning point*, near the ice shelf front plays a fundamental role in ice shelves dynamics, as it constraints and diverts the ice-flow. The role and location of pinning points are found to greatly contribute in explaining differences in flow regimes between the Roi Baudouin and two neighbouring ice shelves.

Finally, the thesis focuses on other interferometric data in Dronning Maud Land to identify other pinning points and investigate on their temporal variability, in link with tides.

Résumé

Les *ice shelves*, que l'on trouve principalement en Antarctique, sont des extensions flottantes d'une calotte glaciaire. Elles constituent l'interface entre la calotte et l'océan. Si elles présentent une dynamique d'écoulement propre, les ice shelves sont cependant couplés au reste de la calotte et de ce fait elles jouent un rôle de régulation des transferts de glace du continent vers l'océan (*Buttressing Effect*). La perte de masse des ice shelves induit une diminution du buttressing et donc une accélération des transferts de glace vers l'océan, ce qui contribue à l'augmentation du niveau marin. Ainsi, l'étude de la dynamique des ice shelves est essentielle pour pouvoir prédire et quantifier la contribution future de l'Antarctique à l'augmentation du niveau marin, dans un monde qui se réchauffe.

Ce mémoire étudie la dynamique des ice shelves par interférométrie SAR dans la région de Dronning Maud Land en Antarctique, à partir d'image satellitaire de la mission tandem ERS1/2 (1995-1996). L'interférométrie SAR ou InSAR est une technique de télédétection active qui exploite les différences de phase entre des images radar (SAR) acquises à des moments différents pour déterminer les déplacements survenus entre les différentes acquisitions. Se servant de cette technique, une carte du champ de vitesse horizontal a été dérivée à haute résolution (50m) pour l'ice shelf Roi Baudoin. De ce champ de vitesse, les vitesses de déformation par cisaillement de l'ice shelf ont également été déduites et analysées. Les résultats montrent que le *pinning point* près du front de l'ice shelf joue un rôle fondamental dans la dynamique de ce dernier puisqu'il contraint et réoriente son flux. Ce sont le rôle et la position des pinning points qui permettent d'expliquer les différences de vitesses observées entre l'ice shelf Roi Baudoin et deux ice shelves voisins.

Une partie du mémoire est en outre consacrée à l'étude de la qualité des résultats, des sources d'erreurs et des limitations de l'InSAR.

Enfin, ce mémoire analyse des données interférométriques d'autres parties de la région de Dronning Maud Land afin de repérer d'autres pinning points et d'enquêter sur leur variabilité temporelle, sous l'effet des marées.

Acknowledgments/Remerciements

First and foremost I offer my sincerest gratitude to my supervisor, Reinhard Drews, who has supported me throughout my thesis with his patience and knowledge. Without him this thesis would not have been completed or written. One simply could not wish for a better or friendlier supervisor.

I also thank Prof. Frank Pattyn for the support he provided when it was needed whilst allowing me the room to work in my own way.

I am grateful to the InBev Baillet Latour Antarctica Fellowship and International Polar Foundation, which enabled the existence of the project Be:Wise and provided this thesis with valuable data. I would also like to thank the European Space Agency for providing ERS SAR data through the project CP.10754.

Je remercie le Prof Anne De Wit pour avoir su me donner, sur la fin, un "petit coup de pouce" inattendu mais tellement nécessaire, ainsi que le Prof. Jean-Louis Tison pour avoir su se montrer compréhensif.

Je tiens aussi à remercier toute l'équipe du laboratoire de glaciologie pour le bon accueil fait aux mémorants. Merci tout particulièrement à Brice, toujours à l'écoute et disponible pour aider les autres.

En plus de cela, j'aimerais remercier vivement mes deux relecteurs, Nicolas et Florence, pour le temps qu'ils ont consacré à ce mémoire.

Une pensée particulière est adressée à mes camarades de sciences de l'environnement et mes "collègues de bureau" que j'ai côtoyés quotidiennement et dont la bonne humeur a égayait les journées. J'aimerais exprimer ma gratitude à Carelle pour l'assistance dont elle a fait preuve sur la fin.

Enfin, j'adresse mes plus sincères remerciements à ma famille, mes colocs et mes amis qui m'ont aidée, soutenue et encouragée au cours de la réalisation de ce mémoire.

Contents

List of Figures

List of Tables

List of Acronyms

ALOS   Advanced Land Observing System (satellite)

ASAR   Advanced Synthetic Aperture Radar (sensor)

Be:Wise   Buttressing effect: Why ice shelves are essential? (research project)

BP   Before Present

DEM   Digital Elevation Model

DIFF&GEO DIFFerential interferometry and GEOcoding (Gamma module)

DInSAR   Differential Interferometric SAR

DISP   DISPlay (Gamma module)

DML   Dronning Maud Land (region)

ERS   European Remote Sensing

ESA   European Space Agency

GCP   Ground Control Point

GIS   Geographical Information System

GLAS   Geoscience Laser Altimeter System (sensor)

GPS   Global Positioning System

GMT   Generic Mapping Tool (software)

ICESat   Ice, Cloud and land Elevation Satellite

InSAR   Interferometric SAR

IPCC   Intergovernmental Panel on Climate Change

ISP   Interferometric SAR Processor (Gamma module)

LOS   Line of Sight

MCF   Minimum Cost Flow (function)

MSP   Modular SAR Processor (Gamma module)

PALSAR   Phase Array Type L-band Synthetic Aperture Radar (sensor)

Radar   Radio Detection And Ranging

RAMP   Radarsat Antarctic Mapping Project

RAR   Real Aperture Radar

RMSE   Root Mean Square Error

RBI   Roi Baudouin Ice shelf

SAR   Synthetic Aperture Radar

SLC   Single Look Complex

SNR   Sound to Noise Ratio

SRA   Satellite Radar Altimeter (sensor)

Chapter 1

Introduction

The earth, our environment, can be understood as a set of different envelopes in interaction with each other: the atmosphere, the hydrosphere, the lithosphere, the biosphere and the cryosphere. This thesis has a particular interest in one of them: the *cryosphere*. The cryosphere is the portion of the earth's surface where water is under frozen state. It encompasses elements such as ice sheets, snow covers, glaciers (cf. table 1.1). The cryosphere plays an important role in the global climate system through linkages and feedbacks with the other parts of the earth system. It is not only linked to the hydrosphere by locking up or releasing substantial amount of fresh water when water freezes or ice melts, and hence influences the global oceanic (thermohaline) circulation; but it also affects atmospheric processes such as clouds and precipitations (Barry and Gan, 2011).

This study, for its part, focuses on Antarctic ice sheet and more specifically on ice shelves. An *ice sheet* is a perennial mass of glacier ice and snow that stretches out a surrounding terrain greater than 50,000 km^2 (Graham, 2011). There are currently two remaining ice sheets: one in Antarctica and one in Greenland. These two ice sheets represent nevertheless the largest bodies of fresh water on earth. A schematic ice sheet is presented on figure 1.1. Ice originates from gradual transformation of snowfall in accumulation zones[1], ice then flows, driven by gravity, to ablation zones where ice either melts and runoffs or goes into sea, forming, in most cases, floating extensions called *ice shelves*. Once in the ocean, the ice starts melting in contact with warmer water. Ice masses can also detach. The latter process is known as *icebergs calving*.

In its last report (Lemke et al., 2007), the Intergovernmental Panel on Climate Change

---

[1] *accumulation zones*: zones where mass gains are greater than losses, (as opposed to *ablation zones*).

Cryospheric Component	Area $[10^6 km^2]$	Ice Volume $[10^6 km^3]$	Potential Sea Level Rise [m]
Snow on land	1.9-45.2	0.0005-0.005	0.001-0.01
Sea ice	19-27	0.019-0.025	~ 0
Glaciers and ice caps	0.51-0.54	0.05-0.13	0.15-0.37
Ice sheets	14.0	27.6	63.9
Greenland	*1.7*	*2.9*	*7.3*
Antarctica	*12.3*	*24.7*	*56.6*
Ice shelves	1.5	0.7	~ 0
Seasonally frozen ground	5-48.1	0.006-0.065	~ 0
Permafrost	22.8	0.011-0.037	0.03-0.10

Table 1.1: The different components of the cryosphere and their importance in terms of area, volume and potential sea level rise (from Lemke et al., 2007, p.342). The values presented are the annual minimums and maximums for snow, sea ice and seasonally frozen ground; the smallest and largest estimates for glaciers and ice caps and the annual mean for the other components. The potential sea level rise estimation makes the assumptions of a 3.62×10^8 km^2 oceanic area, a 917 $kg.m^{-3}$ ice density, a $1,028$ $kg.m^{-3}$ seawater density and a substitution of grounded ice by seawater below sea level.

(IPCC) emphasized the important role played by Antarctic and Greenland ice sheets in sea level rise, as a response to climate change. The future behaviour of ice sheets is actually said to be the greatest uncertainty in sea level projections (Cazenave, 2006). A complete melt of these two ice sheets could induce a sea level rise of 64m (Bamber et al., 2001, Lythe et al., 2001), but even smaller changes in their mass balance would strongly affect the future sea level. During previous warmer climates, such as the last interglacial (the Eemian $\sim$ 125,000 yr BP[2]), the sea level was 6 to 9 meters higher than today (Kopp et al., 2009, Dutton and Lambeck, 2012) partly because of the Greenland and Antarctic ice sheets. According to a recent study (NEEM community members, 2013), the Greenland ice sheet did only contribute in a minor fashion, and the bulk of ice loss must have come from Antarctica. This suggests that the Antarctic ice sheet is more dynamic than previously thought.

With a volume of $24.7 \times 10^6 km^3$ of ice, Antarctic ice sheet, in the South Pole, is by far the main reservoir of ice on earth (with a huge potential contribution to sea level rise). Unlike Greenland, mass loss from surface melting is negligible (Shepherd and Wingham, 2007, Lemke et al., 2007) and no widespread surface melt is currently expected in Antarctica (Alley et al., 2005). It implies that dominant mass loss of the Antarctic ice sheet happens in contact with the ocean. In this context a better understanding of the ice sheet dynamics-especially at the interface between continent and ocean (ice shelves) is essential for our ability to predict climate change effect on Antarctic ice sheet and thus, indirectly on sea level rise.

---

[2]BP= years Before Present where *present* is defined as AD 1950.
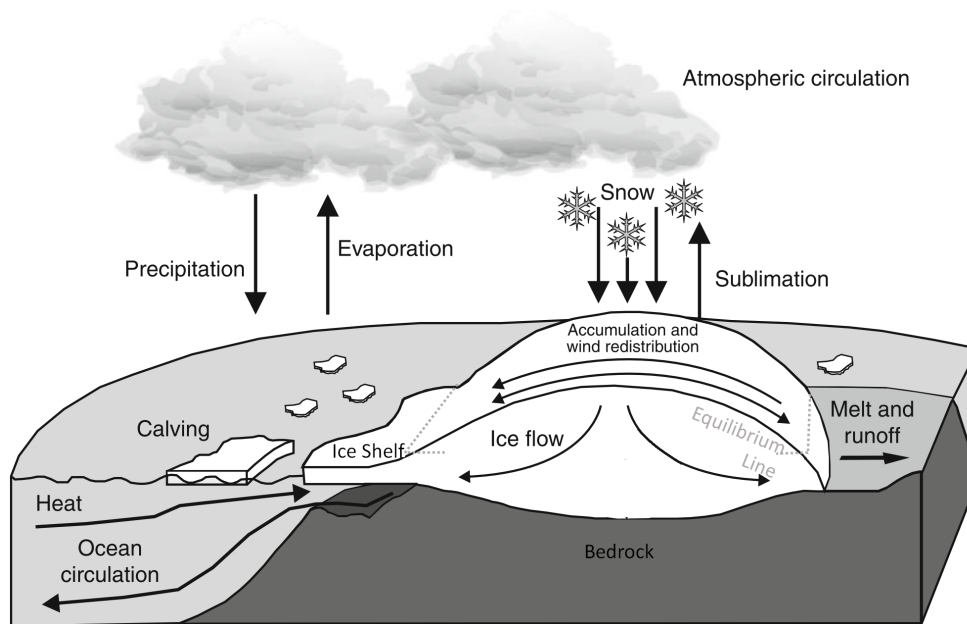
Figure 1.1: Schematic ice sheet (adapted from Graham, 2011, p.594). An ice sheet is strongly linked to the atmosphere and the ocean. Atmospheric snow precipitations feed the ice sheet in accumulation zones, the snow is transformed to ice and flows to ablation zones. Once there, ice either melts and runoffs or is discharged into sea, where the ice begins to float and forms ice shelves. From ice shelves, ice finally melts in contact with warmer water or is calved into the ocean.

An *ice shelf* is a sheet of thick ice[3] that floats on the ocean but remains attached to the grounded ice of the ice sheet (see figure 1.1). Ice shelves form when continental ice streams, very fast currents of ice within ice sheet, flow into the ocean. Because it has lower density than water, ice begins to float. The boundary between the grounded ice and the floating ice shelf is called the *grounding line* (denoted as *GL* in figure 1.2). Due to lower friction with the ocean than with the bedrock, ice of shelves has a tendency to move forward, spreading horizontally and thinning under its own weight (Barry and Gan, 2011, Lemke et al., 2007). This tendency can be partly countered by the friction with embayment side of the ice shelf; or with topographic highs of the sea floor. These topographic highs are called *ice rises*, if they are dozen kilometres large, or *pinning points/ice rumples* if smaller, and they both locally ground the ice shelf, slowing it down. In term of ice dynamics, due to their size, an ice rise diverts the flow around its perimeter whereas a pinning point diverts the flow over itself (Schmeltz et al., 2001). It should be noted that the denomination of ice rise is also given to topographic highs extending seaward the ice sheet into the ice shelf. To avoid any confusion we call the latter kind, peninsula-ice rise as opposed to island-ice rise (totally isolated from the ice sheet). The role of a pinning point is illustrated in figure 1.2. As they

---

[3]Ice shelf thickness can range from less than 100m to more than 2,000 m (Jenkins, 2011).

(a) Ice shelf with pinning point.   (b) Ice shelf without pinning point.
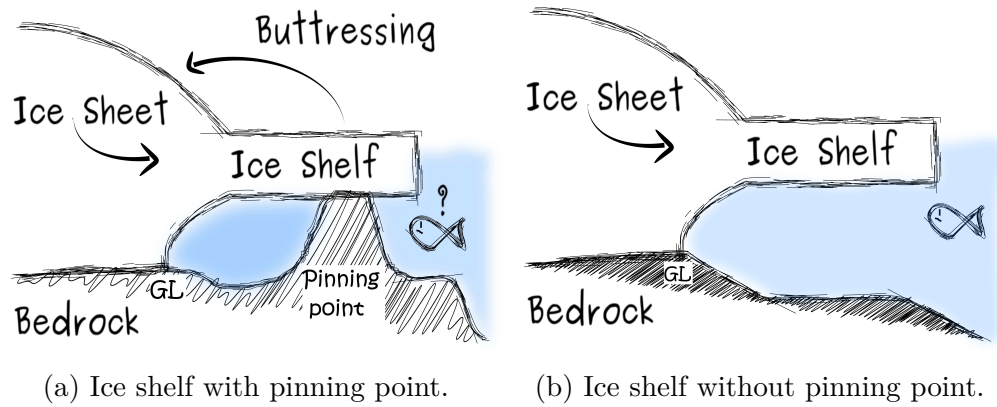
Figure 1.2: Ice shelves with and without grounded feature (pinning point). The pinning point (1.2a) restrains the flow of the ice shelf and thus the ice discharge from the continent. This is called the buttressing effect. While without pinning point, the buttressing is lowered and more continental ice is transferred to the ocean. A pinning point could, for instance, be degrounded by sea level rise or ice shelf thinning. The transition between the ice sheet and the ice shelf is denoted as "GL" for Grounding Line.

are smaller, pinning points can possibly be *ephemeral*, which means that the tidal uplift can "deground" the ice shelf from the pinning point.

Most ice shelves are found in Antarctica, where they occupy overall 1.5×10^6 km^2, which represents 11% of the continent. Ice shelves are important for two reasons. First, they constitute the interface of the ice sheet with the ocean. We have seen above that once in contact with the hydrosphere, the ice is transferred to the ocean either by basal melting or by iceberg calving. By these two processes, ocean has therefore control over extent and thickness of the ice shelves (Jenkins, 2011). Ice shelves are also essential because of their implication for the global sea level. Although a mass loss of ice shelves does not affect sea level directly (the ice is already floating), it does have an indirect impact on sea level rise. Ice shelves are indeed attached to grounded ice sheet, so that they restrain the flow from inland ice. This phenomenon is called the **buttressing effect**. The amount of buttressing exerted on the inland ice-flow depends on drag between the ice shelves and their embayment side or their re-grounding point (ice rise and pinning points) (Lemke et al., 2007). This means that if ice shelves thin or shorten, it will lead to a reduction in the restraint they exert on the flow of inland ice, causing a speed-up of their tributary glaciers and thus an accelerated discharge of grounded ice into the ocean (Dupont and Alley, 2005, Jenkins, 2011). This is even true in case of small ice shelves (Dupont and Alley, 2006). In the end the whole process will greatly contribute to the sea-level rise. For the past couple of decades, an important tool for monitoring ice flow and dynamics has emerged : satellite-based SAR interferometry

Satellite-based SAR interferometry   Satellite-based SAR interferometry (InSAR), is a powerful tool able to provide comprehensive measurements of flow. InSAR is an imaging technique that exploits phase information (interferometry) from radar (SAR images taken at different times, to measure sub-centimetres changes at the earth's surface, which corresponds to ice flow, in our case. Satellite SAR sensors are very valuable, especially for polar studies, because of their ability to capture remotely properties of the surface, and to do it during day- and nighttime and in nearly all-weather conditions.

Goals of this study   The goals of the study are multiple :

- Master automated SAR interferometry processing.

- Identify the critical steps of the InSAR processing as well as the main internal and external sources of error.

- Derive a high resolution horizontal flowfield of an ice shelf and identify ice shelves particularities essential for the processing.

- Have a better understanding of the role played by the pinning points in ice shelves dynamics, especially compared to the role of the lateral friction.

- Identify numerous pinning points in the area of interest and investigating on their temporal variability.

From the list presented above, we can distinguish two kinds of goals: those related to the Interferometric SAR (InSAR) processing and those related to the ice shelf dynamics.

Area of interest   This thesis is a study of the ice shelves in *Dronning Maud Land (DML)*. This area of investigation roughly consists of 2,000 km coastlines in East Antarctica, between [-75,-70]° in latitude and [-25,30]° in longitude. Several research stations are found in the region of Dronning Maud Land, including the Belgian Princess Elisabeth research base. Besides a more global study of the ice shelves of this region, we focused our analysis on the *Roi Baudouin Ice shelf (RBI)* which is a 100 km long and 65 km large ice shelf, located between -71 and -70° of latitude and 24-27 ° of longitude (East). For the Roi Baudouin Ice shelf, horizontal velocities were derived with InSAR. This specific ice shelf is fed by a very fast ice stream, *the West Raghnild glacier*, and laterally confined by an island-ice rise

(*Derwael* ice rise) in the east and by a peninsula-ice rise in the west (*FranKenny* ice rise)[4]. In addition to these two ice rises, RBI is also constrained by one small pinning point (not really visible in figure 1.3) that roughly seems to correspond to the edge of the ice shelf. The entire studied area is pointed out in figure 1.3
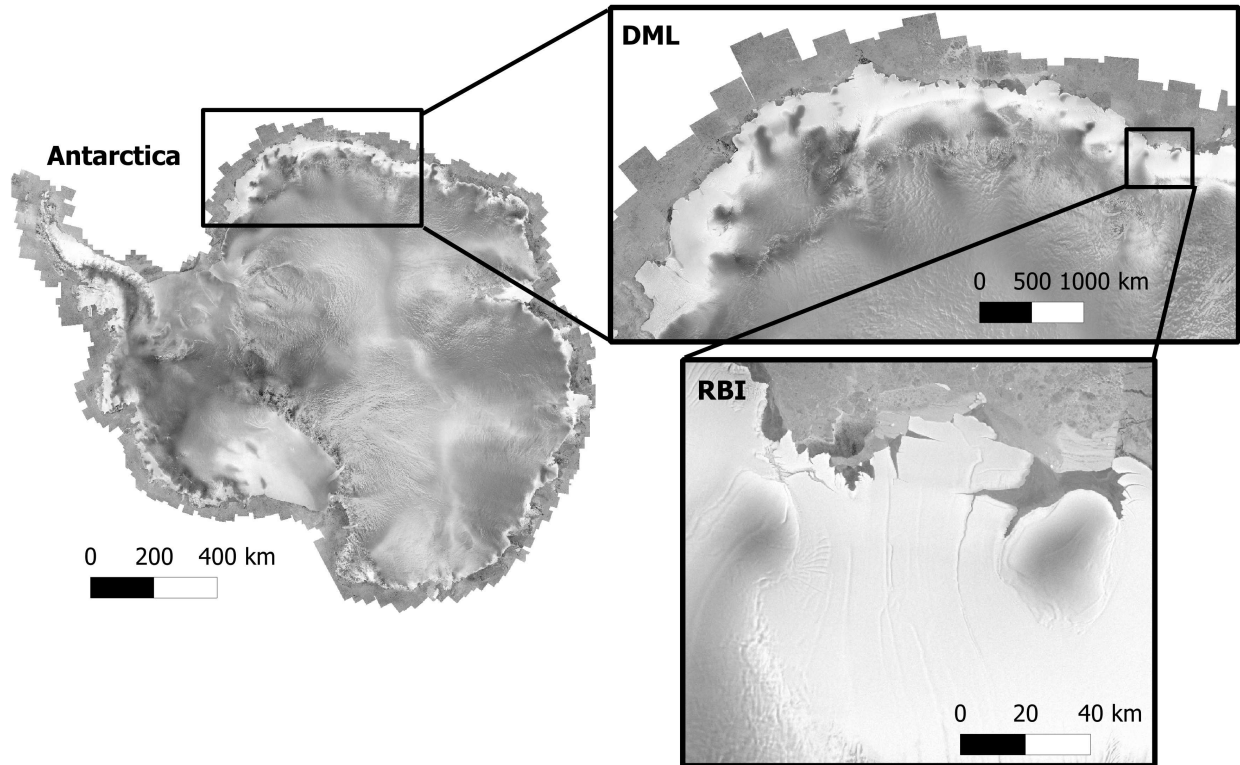
Figure 1.3: <u>Area of investigation</u>. The map in background is the mosaic from Radarsat Antarctic Mapping Project (RAMP) (Jezek and RAMP Product Team, 2002). The first zoom corresponds to Dronning Maud Land (DML), the general studied area while the second zoom corresponds to Roi Baudouin Ice shelf (RBI), which is an ice shelf concerned with a further detailed study.

---

[4]FranKenny is not the official name of the ice rise but it corresponds to the name given to it in a recent paper (Matsuoka et al., 2012). For convenience, we decided to keep this name.

Roadmap The thesis is structured as follows. This introductory chapter presents the basic principles of ice dynamics together with all the important related terms and specifies the goals and area of investigation. We then continue with three methodology-related chapters. The first one (chapter 2) develops the theoretical basis of Synthetic Aperture Radar interferometry. The aim of this chapter is to provide keys to understand the approach adopted throughout this thesis and its results. This is directly followed by chapter 3 that thoroughly presents the processing steps needed to obtain interferometric products such as interferograms and displacement maps and later explains how to interpret them. This chapter corresponds to the methodology part of the thesis and is completed by a short chapter (chapter 4) that exposes the datasets, the "material" used. After the presentation of the material and the method, we will then be able to expose our various results (chapter 5) followed by a discussion of the latter (chapter 6). In the discussion we will compare our horizontal flowfield, our main product, with similar data of the literature. The second part of chapter 6 is devoted to an in-depth discussion about several elements previously pointed out in the results and tries to meet the objectives of the study. We will also present the limits of our results, including the major processing uncertainties. The last chapter finally present the conclusions and perspectives of our study.

Chapter 2

Satellite interferometry

In this chapter we present the technique used throughout this work - namely the interferometry to Synthetic Aperture Radar images. We briefly present the basics of radar, explain the Synthetic Aperture Radar (SAR) technique and finally focus on Interferometric SAR (InSAR).

2.1 Radar

Radar stands for Radio Detection And Ranging. Radar imaging is a technique of active remote sensing: a sensor on a satellite (or on an airborne platform) illuminates a target on the ground by emitting a pulse of electromagnetic energy downwards. The wave passes through the atmosphere to reach the earth's surface and interacts with it. Part of this signal is backscattered to the receiving antenna which records the power of the returned echo.

The round-trip travel time of the backscattered signal can be used to deduce the distance between the sensor and the target, while the amplitude of the echo enables to generate a two-dimensional image of the target area (Bürgmann et al., 2000) (in which each pixel is associated to a backscattering coefficient of the corresponding area). The radar uses microwave which is defined with a wavelength greater than one millimetre. European Remote Sensing (ERS) satellites 1 and 2, the satellites carrying the sensor used in this study send pulses with a 5.6 cm wavelength (in the C band of the microwave spectrum) (cf. section 4.1).

Spaceborne imaging radars present many advantages (Høgda et al., 2011) :

- The satellite altitude enables to image large areas on earth and to do it frequently

(the typical repeat cycle of the ERS system is 35 days).

- Active remote sensing systems are independent of daylight.

- Atmospheric conditions (such as could cover, smoke aerosols, dust etc.) hardly affect microwave regions (Chuvieco and Huete, 2010).

This kind of observations is therefore perfectly suitable for Polar Regions where the cloud cover is frequent, and daylight lacks in winter.

Remark Note that *backscattering* and *reflection* are different concepts (Zhou et al., 2009). A surface such as calm water could, for instance, presents weak backscattering coefficients and thus appear in dark in an intensity radar image (because the receiving antenna collects very little energy back), whereas the real amount of reflected energy is much higher. Calm water surfaces are indeed very reflective but in a specular way, that means that the incident energy is mainly reflected in one direction that does not correspond to satellite's one.

2.2 Synthetic Aperture Radar

Synthetic Aperture Radar (SAR) is a kind of radar sensor that "*combines signal processing techniques with satellite orbit information to produce a much-higher-resolution (tens of meters) radar image*" (Bürgmann et al., 2000, p.170). Actually, virtual antennas are artificially synthesized by combining echoes in order to enhance azimuth (along-track)[1] and range (across-track.)[2] resolutions. SAR technique benefits from Doppler Effect of the moving platform, i.e. the change in radiation frequency due to relative movement between the sensor and the observed surface. In what follows we give a rough presentation of SAR principles, without entering too much into technical details. In the beginning of the section, the acquisition geometry of SAR imaging is presented and defines important geometric terms required afterwards. The second part of the section is then devoted to the particularities of SAR imaging: the resolution, the information given by one SAR image, etc. For a deeper understanding of SAR characteristics, we refer the reader to more complete and specific textbooks such as Curlander and McDonough (1991), Cumming and Wong (2005).

---

[1] Along-track: direction parallel to the motion of the platform

[2] Across-track : direction perpendicular to the motion of the platform.
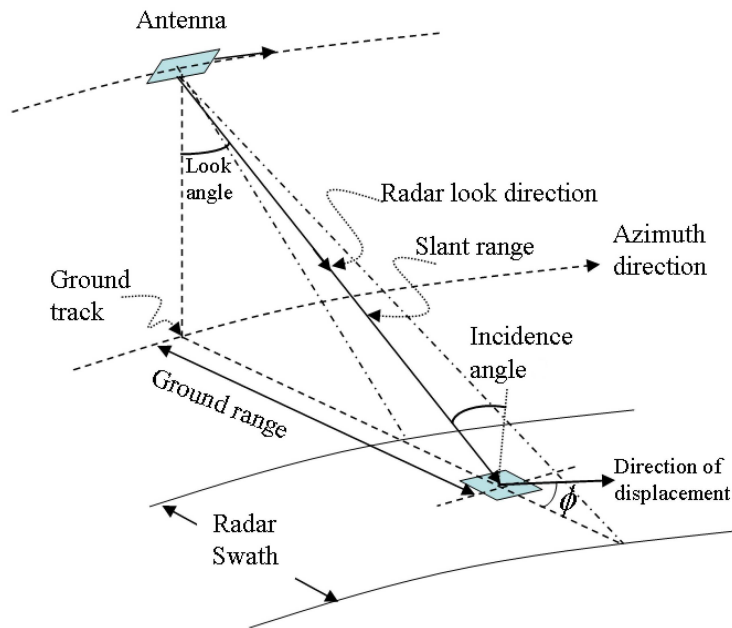
Figure 2.1: Acquisition geometry of a SAR system (Zhou et al., 2009, p.1878). It is a side-looking system characterized by a look-angle and three main directions: slant range (line of sight) direction, its projection on ground range (across-track), and azimuth (along-track).

2.2.1 Geometry of SAR imaging

Several geometric elements intervene in a typical SAR acquisition scene (figure 2.1). A SAR satellite usually has an orbit altitude of hundreds of kilometres (ERS satellites are 780 km high) and carries an antenna pointed to earth's surface with a fixed angle relative to the nadir[3], namely the *look angle* (or *off-nadir*). The look angle is about 23° for ERS 1-2. Although the *incidence* angle with respect to upward vertical is greater than the look angle (because of the earth's curvature), we usually consider them to be equal under the flat-earth assumption (Ferretti et al., 2007). The radar look direction denoted as *Line of Sight (LOS)* is called the *slant range* in the viewing geometry. The along-track and across-track directions of the satellite almost correspond to the *azimuth* and *range* axes on the ground (Furuya, 2011).

Finally the *swath* corresponds to the ground area imaged by the detector. Its typical width is about 50 to-100 kilometres (Bamler and Hartl, 1998, Furuya, 2011). The swath can be seen as set of successive satellite *footprints* put together. A footprint is indeed, the ground area illuminated at a specific time. ERS satellites have a footprint of 5 km and 100 km in azimuth and ground range directions, respectively (Ferretti et al., 2007).

---

[3]nadir: the downward vertical axis between a target and a sensor.

Remark We should nevertheless keep in mind that this whole description only stands for *stripmap* mode of SAR instruments, which is the standard imaging mode used in this study. It achieves high spatial resolution thanks to a fixed look angle while a more recent mode, *ScanSAR* allows to cover wider areas by varying the off-nadir angle to the detriment of spatial resolution.

2.2.2 Complex SAR image

Now that the basics of the viewing geometry of SAR systems have been explained, we can focus on the particularities and properties of SAR data themselves. The raw data acquired with a SAR sensor are impossible to visually interpret. The first interpretable SAR images are Single Look Complex (SLC) images. The conversion of raw SAR data to SLC images requires a bit involved processing algorithms (Furuya, 2011). As in optical passive remote sensing, a SAR (or a SLC) image can be seen as a rectangular grid of assembled picture elements: the *pixels*. Each pixel represents a small portion of the earth's surface that is called a *ground resolution cell* or sometimes also *ground pixel*. A SAR scene is therefore a two-dimensional array where the rows can be assimilated to azimuth locations and columns to ground-range (Ferretti et al., 2007). According to Raney (2005, p.937), *spatial resolution* is "*the minimum separation between two small and similar side-by-side reflectors such that they appear discretely in the image to be two, rather than merged into one.*" The better resolution a scene has, the smaller the pixels and resolution cells and the more precise this scene will be on the image.

A) Resolution

Radar remote sensing systems are characterized by differentiated spatial resolution relative to range and azimuth directions. This implies that the size of the pixels depends on the direction (for instance an ERS resolution cell measures about 20 m in range and 5m azimuth directions). Let us see now, what are the mechanisms behind the resolutions in range and azimuth.

Range resolution In a radar system using simple pulse (as depicted in figure 2.2 (a)), the sensor discriminates two near targets (in ground- and slant- range directions), only if the distances separating them allows to distinguish their returned pulses. If two targets are too close, their echoes will overlap and they will not be discriminated on the received pulse. This minimal distance detected in range direction is called the range resolution. If we take two objects separated by a distance Δr, the time difference (Δt) between transmission and
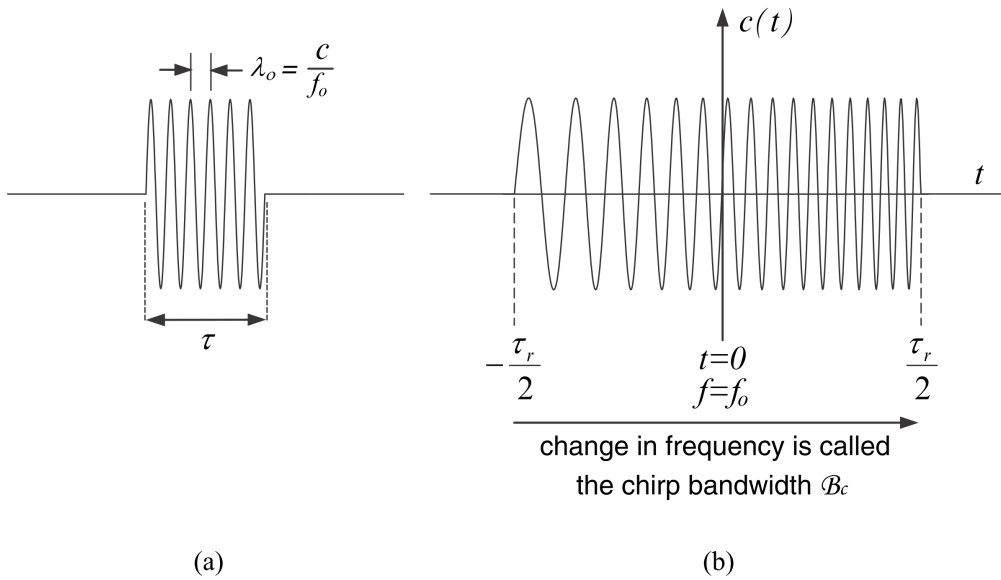
Figure 2.2: Different waveforms of microwave pulses (Richards, 2009, p.55) (a) simple pulses, found in basic radar systems. (b) Chirped pulses have been introduced to improve range resolution. It enables a better target discrimination by modulating the frequency of the sent signal.

reception of two signals can be expressed as $\Delta t = \frac{2\Delta r}{c}$, where c corresponds to the speed of light (3.10^8 m/s). The factor 2 is due to the round-trip. This means that to avoid pulses overlap, the distance between the two objects has to be greater than half the duration of a pulse (τ on figure 2.2 (a)). In other words, the slant-range resolution ($r_{s.r}$) for a basic radar system is $r_{s.r} = \frac{c\tau}{2}$. Hence, to improve resolution, τ the temporal length of the pulse needs to decrease. Unfortunately, by doing that we also reduce the energy carried by the pulse and thus the target detection sensitivity (Richards, 2009). Simple solution to solve this problem exists: the frequency of the transmitted pulse is linearly modulated to form a *chirp* (cf. figure 2.2(b)). This enables to get a much higher resolution because overlapping echoes can be discriminated thanks to differences in frequency. SAR imaging systems use such a technique to improve range resolutions. In this case, slant range resolution can be expressed as follows (Richards, 2009, Chuvieco and Huete, 2010, Furuya, 2011, Marino, 2012):

$$r_{s.r} = \frac{c}{2\mathcal{B}_c} \tag{2.1}$$

where the term $\mathcal{B}_c$ is the chirp bandwidth[4]. The ground range resolution can be derived from (2.1):

$$r_{g.r} = \frac{c}{2\mathcal{B}_c \sin\theta} \tag{2.2}$$

The only difference between (2.1) and (2.2) comes from the $\sin\theta$ term (θ being the incidence

---

[4]Chirp bandwidth: the width of the frequency interval of a chirped pulse.

angle) because the ground-range direction is a projection of the slant-range on the horizontal plane.

Azimuth resolution   Although chirped pulses are not specific to SAR imaging, the improvement in azimuth resolutions are intrinsically linked to SAR characteristics. In the classical radar imaging, Real Aperture Radar (RAR), resolution in along-track depends on the slant-range distance to the target (R_0), the wavelength (λ) and the length of antenna with respect to azimuth direction (l_a). The relation takes the following form (Chuvieco and Huete, 2010, Marino, 2012, Richards, 2009):

$$r_a^{RAR} = \frac{R_0\lambda}{l_a} \tag{2.3}$$

Owing to the R_0 term, RAR resolution depends on the platform altitude and on the position across the swath. This leads to inefficiency of RAR satellites concerning azimuth resolution because of their orbit altitude and technical limitations of antenna's length. For this reason, Synthetic Aperture Radar (SAR) technique has been implemented. It achieves higher azimuth resolutions with the synthesis of an *apparently* long antenna (the *aperture*) thanks to Doppler Effect, i.e. the use of the forward linear motion of the satellite that provokes a shift in radiation frequency. The illumination time of a particular spot on the ground defines the length of a synthetic aperture, L_A (Richards, 2009). In a SAR system, a point on the ground is not illuminated with just one single pulse but with a sequence of pulses. As a consequence the collection of all the acquisitions of the same point is equivalent to having performed a single acquisition with an antenna array whose length (i.e. aperture) equals the footprint (Marino, 2012). A broader beam (beamwidth = Θ) in azimuth enables to increase the duration of illumination of spot on the ground and thus, to improve azimuth resolution. We see in figure 2.3 that Θ is inversely proportional to l_a, the real length of antenna. As a result the shorter the real antenna length, the longer the synthesized aperture and the better the resolution. After data compression and complicated formation of image, the SAR azimuth resolution becomes (Richards, 2009, Furuya, 2011, Marino, 2012):

$$r_a^{SAR} = \frac{l_a}{2} \tag{2.4}$$

Contrary to RAR, along-track resolution in SAR is thus directly proportional to the physical antenna length.
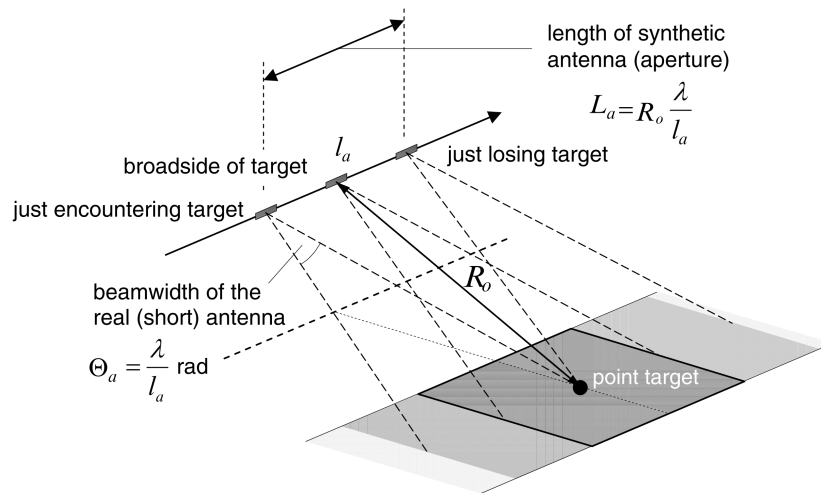
Figure 2.3: The concept of antenna synthesis in a SAR system (Richards, 2009, p.62) (footprint has been simplified to a rectangle).

Some final remarks on resolution

- If the incidence angle equals zero, i.e. $\theta = 0$, there is no ground-range resolution (since $\sin \theta = 0$). That is why, radar systems are side-looking. But on the other hand, such an acquisition geometry brings about geometric distortions that need to be tackled.

- We can deduce from equations (2.2) and (2.4) that SAR resolutions are independent of the altitude of the moving platform.

- Since ground range resolution is a function of the incidence angle, it induces variation across the swath.

- Finally, in a SAR system, resolution does not depend on the frequencies nor on the wavelengths used but only on chirp bandwidth, incidence angle and antenna length along azimuth (see equations (2.1), (2.2) and (2.4)).

B)   The Single Look Complex image

A Single Look Complex image is the first interpretable image we can get from raw data supplied by a SAR sensor. Unlike usual (optical) remote sensed images, each pixel of an SLC is a complex number (as opposed to integer pixels). A complex number can be divided into two parts: a real one and an imaginary one[5]. This is convenient to represent two independent values with one number. Amplitude and phase of the backscattered signal are indeed gathered together into a unique complex number for which modulus and argument represent *amplitude*[6] and *phase*[7], respectively. Amplitude and phase and information they provide are developed below. However, it is useful to firstly have a word about basic optics.

---

[5]For more information about complex numbers, please refer to appendix A on page 84.

[6]Amplitude: the maximum absolute height value of a periodic wave.

[7]Phase: this is an angle, expressed in radians, that represents a fraction of a wave cycle which has elapsed, relative to the origin (Ballou, 2005).

Optics basics Equation (2.5) shows the general formulation of an electric field linked to a plane electromagnetic wave. This is a sinusoid expression that can be found in numerous textbooks dealing with general physics or optics (e.g. Benson (1996), Cloud (2008), Giancoli (2000))[8]:

$$\vec{E}(\vec{R}, t) = \vec{E}_0 \cos(\vec{k}\vec{R} - \omega t + \phi_0) \qquad (2.5)$$

where $|\vec{E}_0|$ corresponds to the amplitude of the wave, $|\vec{k}| = \frac{2\pi}{\lambda}$ is the wave number (in $rad.m^{-1}$) and depends on the wave vector $\vec{k}$, $\omega = 2\pi f = |\vec{k}|c$ is the angular frequency (in $rad.s^{-1}$, f being the frequency) and ϕ_0 the initial phase offset. Equation (2.5) depends on two variables: $\vec{R}$, the space vector in slant range and t, the time. The whole expression in brackets is called the phase (ϕ):

$$\phi = \vec{k}\vec{R} - \omega t + \phi_0 \qquad (2.6)$$

To exploit phase information, the SAR system has to be *coherent*, i.e. the transmitted pulses must have the same initial phase offset ϕ_0. When we deal with SAR systems, electric field in equation (2.5) is often expressed with the complex exponential form (as for instance in Richards (2009), Zhou et al. (2009))[9]:

$$\vec{E}(\vec{R}, t) = \vec{E}_0 e^{i(\vec{k}\vec{R} - \omega t)} = \vec{E}_0 e^{i\phi} \qquad (2.7)$$

This expression is, due to the properties of the exponential functions, more convenient to use and with values easier to manipulate. Equations (2.5) and (2.7) are very general formulations holding for incident as well as reflected waves.

As it is depicted in figure 2.4, the expression of a wave is held by three independent parameters: the wavelength, the amplitude and the phase. In the following paragraphs, which describe the three parameters mentioned above, we will only consider the backscattered energy at the level of the sensor.

Amplitude As well explained by Zhou et al. (2009, p.1878) "*the amplitude of an* [SLC] *image pixel represents the backscattering capability of the terrain of the corresponding ground*

---

[8]Equation (2.5) can also be expressed with the sine function, the only difference lies in the value of the ϕ_0. Sine and cosine are indeed only separated by a $\frac{\pi}{2}$ offset.

[9]for more details, please refer to Appendix A.

pixel to send the incident energy back to the antenna". It depends more on the roughness of the terrain than on the chemical composition. It is usually visualized with a grey-scale image where brighter pixels means stronger backscattering. Amplitude images look like black-and-white pictures but their acquisition is independent of time and weather. Two things are to keep in mind:

First of all, although amplitude E_0 of an electromagnetic wave cannot be measured directly, it is still possible to deduce it from the beam intensity I that is directly observed by the sensor (Cloud, 2008). The relation between the two values holds like this: $I = (E_0)^2$. In what follows, intensity images are presented rather than amplitude images (for convenience). It just has to be remembered that intensity images display information about amplitude.

And on the other hand, the amplitude value of a pixel results from all the contributions of the elementary scatterers[10] within the resolution cell. As a direct consequence of the superposition of signals reflected by elementary scatterers, *speckle* appears in SAR images. It manifests itself visually as a 'salt and pepper' effect because signals from multiple reflections between scatterers are added to direct backscattering, causing random amplitude variability. This is the imbalance between negative- and positive- sign signals that decides the level of the resulting amplitude (Ferretti et al., 2007). Spatial averaging of the image can be performed to reduce this noise.
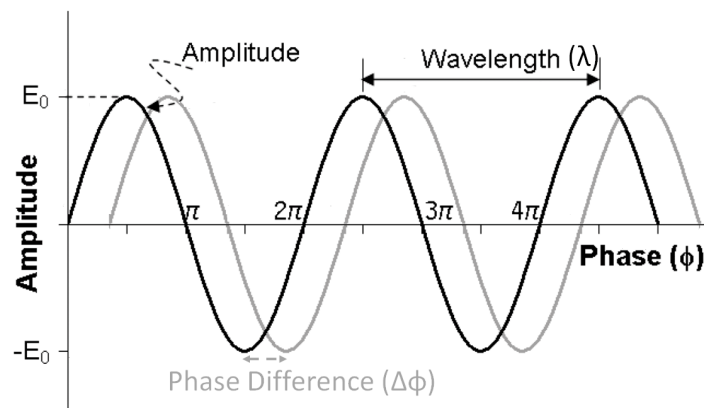
Figure 2.4: Schematic representation of an electromagnetic radiation (adapted from Zhou et al. (2009, p.1879)). The figure shows the relation between amplitude, wavelength and phase in a wave. The **wavelength** depends on the SAR system. The **amplitude** is the square root of intensity of the backscattered echo. And the **phase** is linked to the distance of the wave traveling path. In practice, absolute phase values seem random, but relative phase values are not. Differencing the phases of two waves (related to the same information) removes indeed the random contribution to the phase, leaving a signal that depicts differences in distance. The phase shift between two waves is shown in grey.

---

[10]Elementary scatterers: objects that have a dimension comparable to radar wavelength, so that they are able to scatter the incident wave.

Phase   Amplitude deals with reflection intensity thus, with surface properties whereas phase contains information about geometry between the antenna and the ground targets. For several scatterers, different slant-range distances from the antenna introduce different transmission-reception delays of the pulses, which appears in a phase shift (because of the sinusoidal nature of the signal). The phase records therefore the distance travelled by the signal. There are however two limitations to distance measurements associated with phase.

First, due to the periodic nature of the wave, a phase is expressed in radians angular units and can only take a value between the interval $[-\pi; \pi]$. A normal phase is therefore **wrapped**.

Secondly, the phase images alone are hard to interpret and practically useless because a pixel contains hundreds of elementary targets and each target contributes to the pixel phase value with a complex reflection coefficient (Massonnet and Feigl, 1998). Following these authors, since the wavelength of the radar is much smaller than the ground pixel,[11] the phase of a pixel is the argument of a complex number, itself formed by the summation of hundreds of unknown complex numbers. As a result, the phase alone appears to be random. Nevertheless, phase differentiation enables to eliminate the random contribution to the phase measurement and to provide a measure of relative distance, provided that the elementary targets remain stable (Massonnet and Feigl, 1998).

2.3   SAR interferometry (InSAR)

Interferometric SAR (InSAR) is a technique used to produce ground displacement and topography maps, from **phase information** of several SAR images. InSAR takes advantage of both techniques, SAR imaging and interferometry[12]. As phase depends on travel path, phase difference of two images of the same area could result either from different ranges to the target (different satellite points of view - topographic issue) or from changes at the surface (different times of acquisition - motion retrieval) (Bürgmann et al., 2000).

2.3.1   Historical overview and brief literature review

Before dealing with the practical details of the InSAR technique, a word about historical development of SAR interferometry and about the main developers of this technique could

---

[11] A dozen of meters against 5.6 cm for ERS.

[12] Interferometry: technique that exploits the interference between coherent waves.

be useful. Authors of topic-related reviews (Bürgmann et al., 2000, Massonnet and Feigl, 1998, Rosen et al., 2000) usually agree to say that interferometry was first applied to radar in the early 1970's. It began with earth-based studies of the topography of Venus and the moon (Rogers and Ingalls, 1969, Zisk, 1972) and then continued with airborne radar (Graham, 1974). Satellite-based applications of InSAR started in the late 1980's and were first dedicated to surface topography reconstruction (Goldstein et al., 1988, Li and Goldstein, 1990) by exploiting the difference in phase due to different points of view. According to Bamler and Hartl (1998), Massom and Lubin (2006), the launch of the satellite ERS-1, in 1991, provided a large amount of suitable data for spaceborne interferometry and consequently initiated the development of this study field. A few years later, in 1993, Goldstein et al. and Massonnet et al. first used satellite data to produce surface displacement maps by SAR interferometry. Theses authors initiated thereby a brand new field of application for InSAR: motion retrieval.

This was a piece of history of InSAR, a rapidly evolving and powerful tool that is now widely used to solve diverse geophysical problems, including those of glaciology. Before going on with a more detailed explanation of the technique, some important authors and reviews need to be emphasized. A lot of well-explained review articles exist. Reader wanting a basic overview of the topic is advised to refer to reviews such as Furuya (2011), Høgda et al. (2011), Rott (2009) or Ferretti et al. (2007) while people who desire a more in-depth discussion concerning theory and application of InSAR can find a lot of excellent and often-cited articles. This includes: Bamler and Hartl (1998), Massonnet and Feigl (1998), Bürgmann et al. (2000), Rosen et al. (2000), Simons and Rosen (2007), Zhou et al. (2009)... We should end this very brief state-of-the-art by underlining that Massom and Lubin (2006) wrote a very interesting book. Since it deals with polar remote sensing, it is directly linked to the subject of this thesis and it then offers a very relevant source for specific issues of Polar Regions.

2.3.2   InSAR principles

We begin with a presentation of the interferometric phase and have a word about the interferograms (= the mean to present the interferometric phase). We then present the different contributions to the interferometric phase before finishing the chapter focusing on some limits/complications related to the interferometric phase.

A)   Interferometric phase

As only phase shift between two signals has meaning, phase information can only be exploited in a relative way. To do so we combine the phase information of two images of a scene, taken from slightly different position in space and/or at different times, and we deduce information about the scene. If the different SAR images are acquired simultaneously, from different point of view and with two separated antennas, they are then used for topographic mapping. This kind of interferometry is called *single pass* and the underlying principles are similar to stereoscopy. The other way to exploit phase information is called the *repeat-pass* interferometry. In this case, two images of a same area obtained at different times are analysed, to map surface changes (ice flow velocities in our case). As phase differences are linked to travel-path differences in slant range, the only displacement InSAR can detect, are those in the LOS direction. For this reason, the SAR sensor is completely insensitive to motion in azimuth direction (parallel to the platform motion).

As previously explained, InSAR technique tries to retrieve path differences of two echoes separated in time, based on phase measurements. The relationship between phase differences (called *interferometric phase* or phase shift) and slant range distance holds like this (Zebker et al., 1994, Rosen et al., 2000):

$$\Delta\phi = \frac{4\pi}{\lambda}(R_1 - R_2) = \frac{4\pi}{\lambda}\Delta R \tag{2.8}$$

Equation (2.8) can be split into three different contributions: a 2 factor due to the round-trip of the wave : the wave has to hit the target and to return to the sensor; a 2π factor which corresponds to the number of radians per wavelength (i.e. per wave cycle); and finally the factor $\frac{\Delta R}{\lambda}$ is equivalent to number of wavelengths, ΔR being the relative distance in slant range of the two waves.

B)   Interferogram generation

To understand better what is next, a word about interferograms and their generation is required. Many of these concepts will be detailed later (see section 3.1). We need to address the subject, because an interferogram is the first interpretable interferometric product and the common bond shared by all the fields of InSAR. An *interferogram* is a complex image formed by the cross-multiplying, pixel by pixel, of the first complex SAR image (the master) by the complex conjugate of the second SAR image (the slave) (Ferretti et al., 2007). The

modulus of the resulting complex interferogram corresponds to the amplitude of the master multiplied by the amplitude of the slave, this is therefore a measure of the cross-correlation of the images (Bürgmann et al., 2000); while its imaginary part is the interferometric phase, the phase difference between the master and the slave. In an interferogram, each complex pixel of the image depicts the interferometric phase in a periodic colour cycle, with sometimes magnitude information (correlation between the two SLCs images) mapped to a grey-scale shade. Concerning the phase information, the interferogram can be seen as a contour map of *fringes*, i.e. isophase lines. It is usually displayed in "*a color wheel fashion, where one complete fringe cycle represents a 2π phase shift (i.e. one complete interferometric phase cycle from $-\pi$ to π)* "(Massom and Lubin, 2006, p.54).
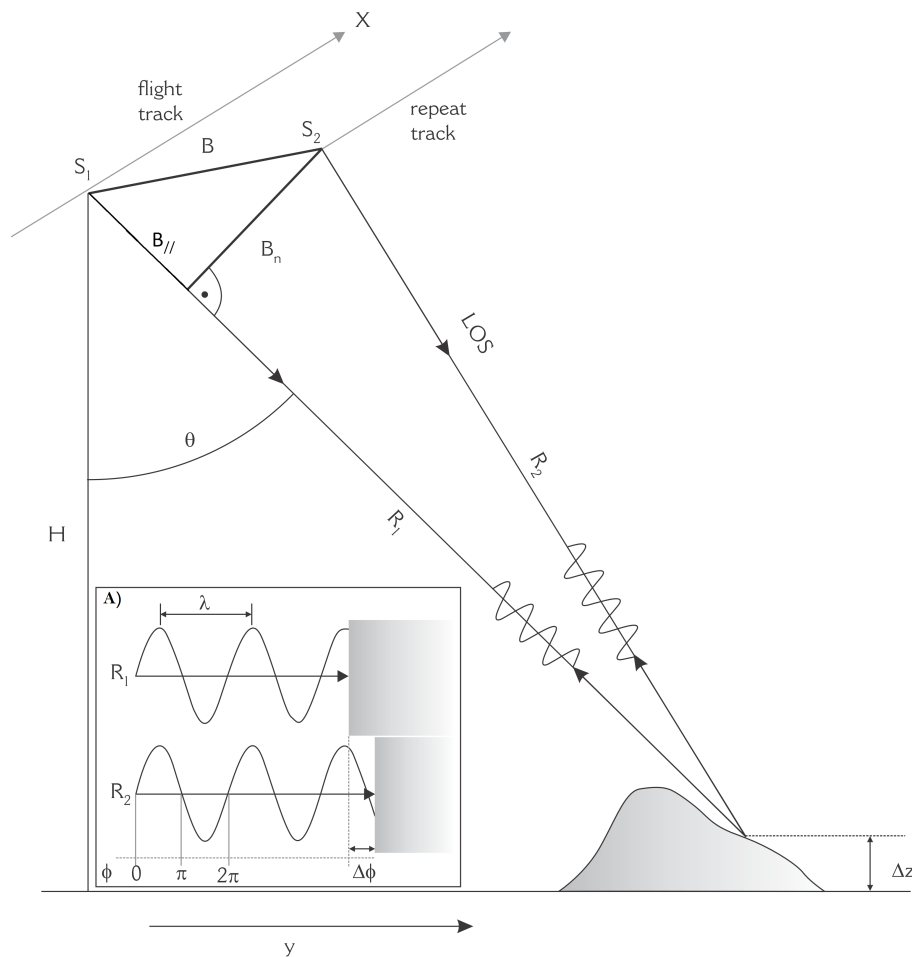
Figure 2.5: Configuration of repeat-track InSAR (adapted from Rott, 2009, p.771). The two images are acquired at different times. S_1 and S_2 = sensor positions; R_1 and R_2 = the geometric slant range distances; B = baseline between the two sensors with $B_{//}, B_n$ = parallel and perpendicular components of baseline, respectively; θ = the satellite look-angle; LOS = Line of Sight. The subfigure A) illustrates the phase shift ($\Delta\phi$) between the two echoes. The path difference measured by $\Delta\phi$ depends on the orbital configuration of S_1 and S_1; the altitude Δz; the relative displacement in slant range; atmospheric wave delay and other kind of noise.

C)   Different contributions to interferometric phase

Let us now consider the figure 2.5 that shows a repeat-track InSAR configuration. We can see that differences in wave travelled distances are caused by different elements. From 2.5 we can identify several contributors to the interferometric phase $\Delta\phi$ (Massonnet and Feigl, 1998, Massom and Lubin, 2006, Rott, 2009, Zhou et al., 2009). Those are summed up in the following equation, and detailed below:

$$\Delta\phi = \Delta\phi_{orbit} + \Delta\phi_{topo} + \Delta\phi_{motion} + \Delta\phi_{atm} + \Delta\phi_{noise} \qquad (2.9)$$

$\Delta\phi_{orbit}$ A major contribution to the interferometric phase is caused by the difference in viewpoint of S_1 and S_2 (the sensor positions) during the image acquisitions. The displacement of the satellites is induced by a shift in orbital trajectory. This effect causes what we call *orbital fringes.*[13] It is possible to remove orbital effect by computing corrections based on a priori knowledge of the spatial baseline (B). If we applied the parallel ray approximation (i.e. $B << R$ allows the assumption $R_1 \parallel R_2$) (Zebker and Goldstein, 1986), the orbital contribution is indeed equivalent to :

$$\Delta\phi_{orbit} = \frac{4\pi}{\lambda}B_{//} \qquad (2.10)$$

$B_{//}$ is the parallel baseline, the component of the baseline B in the slant range direction. From equation (2.10) and with the knowledge of the parallel baseline ($B_{//}$), the removal of the orbital effect is straightforward. This operation is called *flattening.*

$\Delta\phi_{topo}$ The topographic contribution to the interferometric phase originates from the *stereoscopic effect.* The relationship holds like this (Zhou et al., 2009, Høgda et al., 2011):

$$\Delta\phi_{topo} = \frac{4\pi}{\lambda}\Delta z \frac{B_n}{R\sin\theta} \qquad (2.11)$$

where B_n is the perpendicular baseline (the component of B, perpendicular to the slant range direction), Δz is the elevation with respect to a reference surface, θ is the look angle and R is the slant range distance between the target and the sensor. To remove this the topographic contribution we have to synthesize the topographic phase from a Digital Elevation Model (DEM). For an interferometric image pair, it is common to define an

---

[13]As a reminder a *fringe* is a line of equal phase in an interferogram.

altitude or *height of ambiguity*. This parameter represents the shift of altitude needed to produce a 2π phase shift, or, in other words, a topographic fringe (Massonnet and Feigl, 1998). According to Pattyn and Derauw (2002), altitude ambiguity is a way to measure the sensitivity of an interferometric pair to topography. As it is shown it the following equation (Bamler and Hartl, 1998, Massom and Lubin, 2006, Rott, 2009) :

$$H_a = \frac{\lambda}{2} \frac{R \sin \theta}{B_n} \tag{2.12}$$

altitude of ambiguity H_a depends on perpendicular baseline (B_n), SAR look angle (θ) and radar wavelength (λ). We see from (2.12) that longer perpendicular baselines imply higher sensitivity of the interferometric phase to topography.
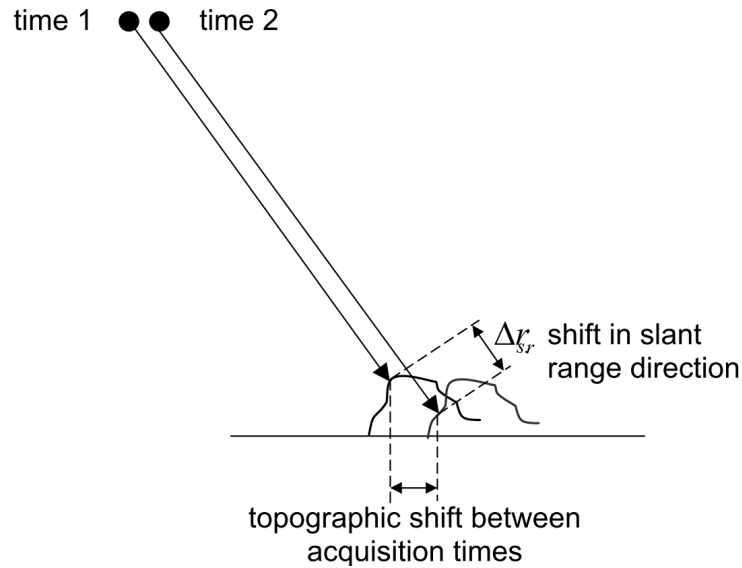
Figure 2.6: <u>Motion detection in LOS direction</u> (adapted from Richards (2009, p.198)). SAR interferometry is only able to detect projection of the displacement (of ice in our case), here denoted as *topographic shift*, in satellite LOS direction. This acquisition geometry is typical of along-track repeat-pass interferometry such as during the ERS tandem mission (see chapter 4).

$\mathbf{\Delta\phi_{motion}}$ is the contribution we wanted to isolate in this study. Motion-induced phase shift happens when a displacement in the slant range occurred between the two image acquisitions (see figure 2.6). From equation (2.8), we deduce that

$$\Delta\phi_{motion} = \frac{4\pi}{\lambda} \Delta r_{s.r} \tag{2.13}$$

where $\Delta r_{s.r}$ denotes the displacement of the scatterers in slant range direction, between the two scenes. This means that the motion sensitivity of an InSAR system depends on the radar wavelength. A 2π phase shift is thus induced by a displacement with a magnitude

of half a wavelength in the LOS direction, which gives a motion of $\frac{5.6}{2} = 2.8$ *cm* in ERS case. If we take a numerical example inspired from one of the scene studied in this thesis, it is possible to compare the sensitivity of ERS system to topography and motion. Given that $B_n = 60$ m, $R = 800$ km, $\theta = 23°$ and $\lambda = 5.6$ cm, a change of 1 m in topography ($\Delta z = 1$ m) brings about phase shift of 2.46° (since $\Delta\phi_{topo} = \frac{4\pi}{5.6\times10^{-2}}1\frac{60}{800\times10^3\sin 23} = 0.0431$ rad), whereas a displacement of 1 m in LOS direction ($\Delta r_{s.r} = 1$ m) causes a phase shift of 12857.14° (because $\Delta\phi_{motion} = \frac{4\pi}{5.6\times10^{-2}}1 = 224.40$ rad). This basic example shows how a SAR sensor is more sensitive to displacement than to topography.

Other contributions The other contributions to the interferometric phase are, in here, gathered under the denomination of *noise*. This category encompasses $\boldsymbol{\Delta\phi_{atm}}$ and $\Delta\phi_{noise}$. The first term is the atmospheric phase shift due to non-identical tropospheric and ionospheric state of the atmosphere that induces signal delays between the two acquisitions (Bamler and Hartl, 1998, Massonnet and Feigl, 1998). "*Tropospheric water vapour and rain cells are dominant sources for this phase error.*"(Bamler and Hartl, 1998, p41). As we were not interested in information concerning the state of the atmosphere, we considered the atmospheric effect to be noise. On the other hand, $\boldsymbol{\Delta\phi_{noise}}$ is caused, among other things, by instrumental artefacts (Massonnet and Feigl, 1998) or by changes in scattering behaviour (e.g. changes in dielectric properties of the ground or random temporal changes between the two scenes acquisition (Bamler and Hartl, 1998)). It is possible to minimize $\Delta\phi_{atm}$ and $\Delta\phi_{noise}$, by selecting suitable interferometric image pairs (Massom and Lubin, 2006).

Motion insolation We can now assume that the interferometric phase, after flattening (the removal of orbital contribution), is only a function of topographic and motion contributions. This is what we see in an interferogram. The next step is then to remove the topographic contribution from the interferogram in order to retrieve ice motion in slant range. To do so there are three possibilities (Massom and Lubin, 2006, Høgda et al., 2011):

1. **The 0 baseline**: From equation (2.11), we see that if the spatial baseline is zero, there is no sensitivity of the interferometric phase to the topography. This case is very particular and hardly met because of technical inability of the satellite to reproduce exactly the same orbit twice.

2. **The use of a Digital Elevation Model (DEM)** : in this case a topographic phase

is simulated from a DEM and removed from the interferogram. This is the technique exploited in the thesis (please refer to chapter 4 for further information about the DEM used).

3. **The use of three coherent SAR images**. This technique assumes that the ice flow remains constant and uses three coherent SAR images to generate two interferograms with equal temporal baselines. One interferogram is "mixed" with phase information on topography and motion whereas the other one presents a "topography-only" phase. To retrieve the motion contribution one has to subtract the topography-only interferogram from the mixed one.

D)   Limits

In here we present the limits associated to phase accuracy and some complication to the interferometric processing.

Phase accuracy   Phase accuracy is mainly affected by phase noise and decorrelation (Høgda et al., 2011). There is a quality measure of the interferometric phase : *the coherence.* The coherence (γ) measures the degree of correlation between two complex SAR images. (Rosen et al., 2000, Simons and Rosen, 2007)

$$|\gamma| = \frac{|\langle E_1 . E_2^* \rangle|}{\sqrt{\langle |E_1|^2 \rangle \langle |E_2|^2 \rangle}} \tag{2.14}$$

where E_1, E_2 are the the backscattered signals received at the respective SAR antennas, $*$ indicates the complex conjugation and $\langle . \rangle$ denotes the statistical expectation, which is in practice determined by spatial averaging around the pixel of interest (Massom and Lubin, 2006). Interferometric coherence ranges from 0 (no correlation) to 1 (perfect phase coherence), lower correlation implies therefore noisier phase. 0.7-1.0 coherence values are usually considered as excellent coherence, 0.5-0.7 good coherence, and 0.3-0.5 noisy but still usable coherence (Massom and Lubin, 2006). When the coherence is lower than 0.3, we consider the two interferometric as decorrelated and no phase information can be extracted. Phase decorrelation includes four uncorrelated sources, which contributes multiplicatively (Zebker and Villasenor, 1992).

$$\gamma = \gamma_{spatial} . \gamma_{temporal} . \gamma_{thermal} . \gamma_{processing} \tag{2.15}$$

- $\boldsymbol{\gamma_{spatial}}$: *spatial* or *baseline* decorrelation occurs when the second pass of the satellite

(to acquire images) does not repeat exactly the first pass. As a result the interferometric baseline is not exactly zero and the SAR scene is viewed from slightly different points of view, which induces decorrelation of the two SAR images.

- $\gamma_{temporal}$ *Temporal decorrelation* is caused when subresolution properties or distribution of imaged scatterers change and modify the backscattered echo as a function of time (Høgda et al., 2011). These changes can be produced by random changes at the surface, such as snow accumulation, or by excessive surface motion of the scatterers (Massom and Lubin, 2006). A third kind of temporal decorrelation is induced by differential atmospheric and ionospheric propagation delay. It should nevertheless be noted that such changes must occur on the surface at the scale of the radar wavelength. Temporal decorrelation act as a limiting factor in for applying SAR interferometry, because if the temporal baseline, the time interval between the two acquisition, is too long, the two SAR images will no longer be correlated and it will not be possible to perform InSAR analysis.

- $\gamma_{thermal}$ *Thermal decorrelation* is related to system noise of the radar, because the radar operates at a non-zero temperature and observes warm objects (Bürgmann et al., 2000).

- $\gamma_{processing}$ *processing errors* also contribute to phase decorrelation and can occur at numerous steps of the processing (Massom and Lubin, 2006) : raw-data processing, co-registration, baseline estimation, phase unwrapping, etc. Processing uncertainties will be discussed with more details in chapter 6.

According to Høgda et al. (2011) most of our errors in measurements by InSAR should not relate to our ability to estimate interferometric phase correctly. They should rather be due to our (in)ability to separate and analyse properly the different contributions of the interferometric phase.

Other complications   Theoretically, once the motion contribution is isolated, it is straightforward to convert phase value into displacement (equation (2.13)), and the knowledge of the temporal baseline of the interferogram enables us to deduce the flow velocities. Unfortunately, to cite Massom and Lubin (2006, p54), a number of additional challenges complicate direct analysis of the observed interferometric phase.

1. By definition the interferometric phase can only be measured *modulo* 2π. However,

the goal of the analysis is to retrieve the absolute phase because it is the only one to be proportional the wave path. To overcome this issue, the phase of each pixel needs to be multiplied by the correct multiple of 2π, this process is known as *phase unwrapping* (cf. section 3.2).

2. Although it is strictly needed for the computation, it is technically difficult to determine accurately the satellites imaging geometry (spatial baseline and orientation) during the recording of the images.

3. After phase unwrapping a constant needs to be added to the interferometric phase to retrieve the absolute value (Rosen et al., 2000). InSAR provides thus relative instead of absolute [ice] motion (and elevation) and the addition of the correct constant value is known as *calibration*.

4. Motion is only given towards the satellite's LOS direction. It is possible, providing the assumption of ice flow parallel to the surface slope, to determine the full three components of velocity by combining 1D flow fields from several observations. These observations have to be made from distinct orbit directions of the satellites (Rosen et al., 2000). This condition is met when we combine descending and ascending satellite passes.

Many of these points will be discussed in detail in the following sections.

Chapter 3

Processing steps: getting a 3D-flowfield from four SLC images

This chapter presents the main steps of the Interferometric SAR (InSAR) processing chain. Based on the theoretical concepts developed in chapter 2, we describe the methods used to get three-dimensional flowfields starting from four Single Look Complexs (SLCs), as it is roughly depicted in figure 3.1. The SLCs are combined in pairs to form two interferograms, using the InSAR technique. The topographic contribution is then removed from the interferograms and two 1D-displacement maps (geocoded) are inferred in different directions, this operation includes the formation of differential interferograms by Differential Interferometric SAR (DInSAR) techniques. A 3D-flowfield[1] is finally derived by combining the two 1D-displacement maps.

The entire data processing was achieved using the commercial *GAMMA SAR and Interferometry Processing Software*[2]. This software is actually a collection of packages that support the entire processing from airborne or spaceborne raw SAR data to finite products. Each package gathers a set of tools dealing with specific aspects of the process. Given that we started from SLC data, only three packages were needed:

- **Interferometric SAR Processor (ISP)**: This module supports the entire steps needed to generate interferometric products starting from SLC data. This encompasses baseline estimation, co-registration, interferogram calculation, coherence esti-

---

[1]To be consistent with figure 3.1, we have kept in here the term *3D-flowfield*. However, in what follows we will only talk about horizontal flowfield, because the vertical motion of ice shelves is mainly influenced by tides (cf. section 3.4).

[2]For the sake of simplicity, the software will be referred as *Gamma*.
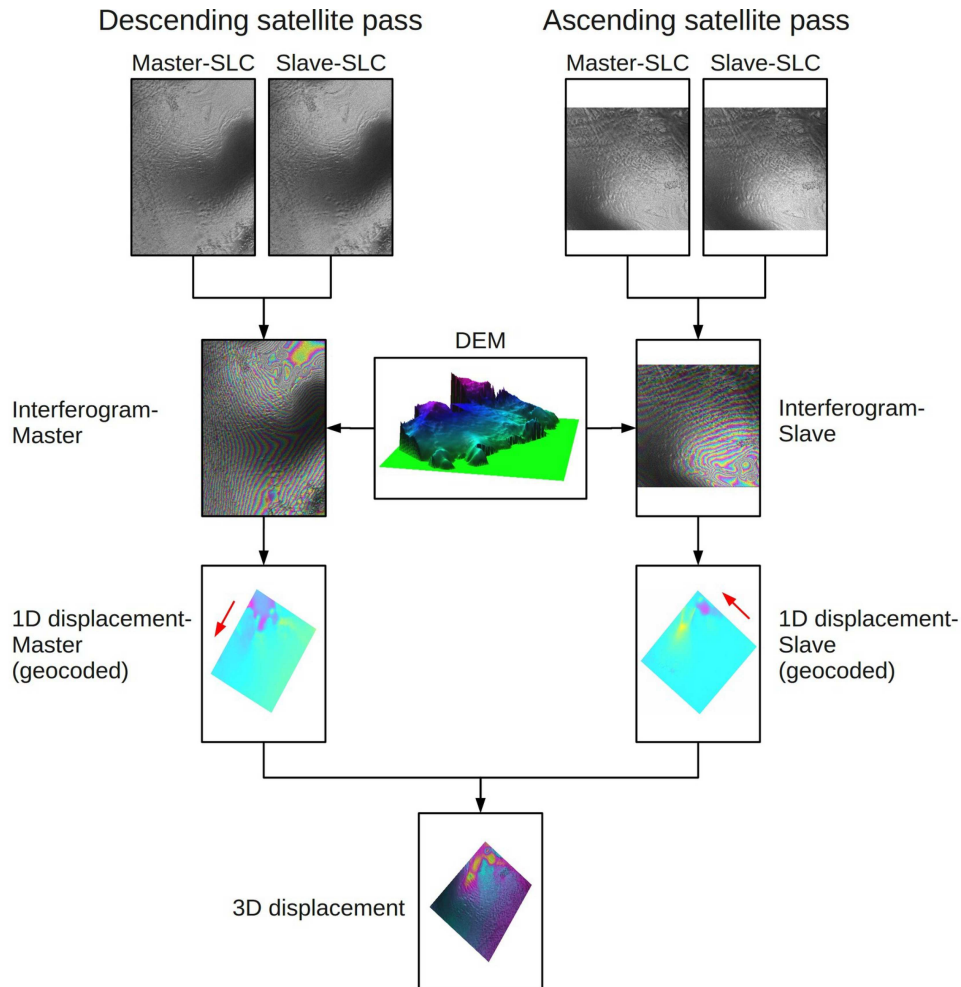
Figure 3.1: Generation of a 3D-flowfield starting from 4 SLC images (Neckel, 2010). The red arrows indicate the satellite flight direction. The process can be divided into three main steps. 1) **InSAR**: Two pairs of SLC images from different satellite passes are combined two by two to form two distinct interferograms denoted as master and slave. 2) **DInSAR**: The contribution of the topography to the phase is removed from the interferograms. Synthetic topographic fringes are synthesized using a DEM, these are then subtracted from the interferometric phase and two 1D-displacement maps (in LOS) are deduced. 3) The two 1D-displacement maps, previously geocoded, are finally combined to retrieve a **3D-displacement** map.

mation, phase unwrapping etc.

- **DIFFerential interferometry and GEOcoding (DIFF&GEO)**: This package provides tools for geocoding,[3] as well as for differential interferometry. The latter aims to retrieve and isolate the motion contribution to the interferometric phase. All in all we could say that it ensures exportability of GAMMA products by converting phase values to geophysical quantities (i.e. displacements) and by making them compatible with Geographical Information Systems (GISs).

- **DISPlay (DISP)**: This module provides support to display products obtained with other packages and convert them into raster(images).

The software was designed to run on workstations with UNIX operating system: it is *command line* oriented and it offers the opportunity to automate the processing chain using shell scripts (see appendix B on page 89).

This chapter follows the structure of figure 3.1. After a few words on the pre-processing, we will focus on the InSAR processing steps, we will then discuss the DInSAR steps needed to separate the motion and the topography (differential interferogram generation) and to retrieve 1D-displacements. Next, we will describe the derivation of three dimensional flow-fields by combining displacement maps. All the processing steps of sections 3.1 and 3.2 are schematised in figure 3.2. Finally, we will discuss the particularities of the floating ice shelves and their influence on the processing.

Remark "*Interferometric processing and differential interferometric processing are strongly interlinked in the sense that several steps of the interferometric processing are applied when generating differential interferograms (e.g. refinement of the baseline, interferogram filtering, phase unwrapping) and differential interferograms can be used in interferometric processing (e.g. to estimate the coherence).*"(Wegmüller and Werner, 2007, p.4)

---

[3]Conversion of geographic data from a given coordinate system to another.
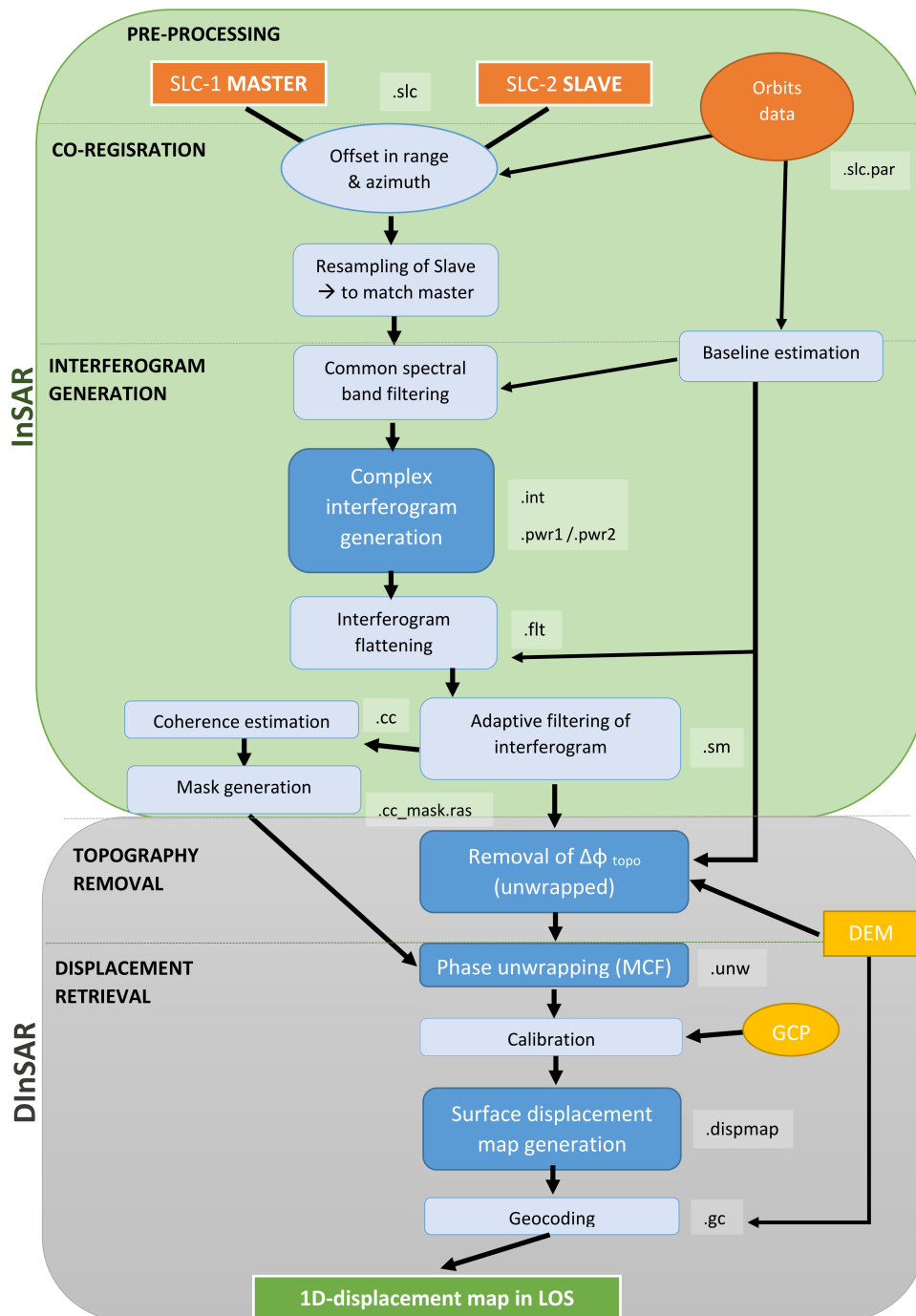
Figure 3.2: <u>InSAR and DInSAR schematic processing steps.</u> A 1D-displacement map is obtained, starting from two SLC images. The process involves schematically two distinct steps: the classic SAR interferometry (**InSAR** = the big green box) and the differential SAR interferometry (**DInSAR** = the grey box). The blue rounded rectangles represent the steps (more important step are coloured in darker blue). Rectangles indicate image/map data whereas ellipses denote other types of data. And finally, orange, yellow and green colours represent input, independent and output data, respectively. Besides, the symbolization of the step in the processing-file names has been added (e.g *.gc* signifies "geocoded").

3.1 Interferometric SAR processing

The first part of the processing belongs to the classical InSAR approach and corresponds to the upper green part of the figure 3.2. From two SLC images, it is possible to deduce one interferogram (figure 3.5) whose colour lines depict the topographic- and motion-induced phase shifts (between the two acquisitions). We detail in what follows the three main steps of InSAR method: the pre-processing, the co-registration and the generation of the interferogram.

3.1.1 Pre-processing

The InSAR processing starts from two Single Look Complex (SLC) images (an SLC is a complex image containing both amplitude and phase information, see 2.2.2). The images of the SLC pair have to be coherent (i.e. not too much decorrelated). SLCs are derived from raw SAR images and are either furnished by the space agencies or processed by the users themselves. It is possible, for instance, to obtain SLC data from the GAMMA's package Modular SAR Processor (MSP). A major advantage of self-processing is the ability to handle long segments (several frames) as single data input. Pre-processing concatenation of data is much convenient than post-processing adjustments and avoids discontinuities where the frames overlap(Massonnet and Feigl, 1998). In this thesis, the data used were mainly processed with the MSP module but some scene were ordered directly into SLC form to the European Space Agency (ESA). In addition to the image acquisition, ancillary information needs to be collected. This information must specify the time reference and the interval of each SLC, the processing parameters and the chosen resolutions (Bürgmann et al., 2000).

Baseline estimation

It is also important, for further processing, to estimate the spatial baseline accurately. The baseline estimation is indeed needed for several operations such as flattening or topographic fringes synthesis (see chapter 2) and is estimated from orbital state vectors of the spacecrafts (Wegmüller and Werner, 2007). It should be noted that it is also possible to re-estimate the baseline from the unflattened interferogram (Wegmüller and Werner, 2007), we did however not perform such refinement of the baseline because we had not enough data available to do it.

3.1.2   Co-registration

Once the SLCs are ready to be used, the SAR interferometry really begins with the *co-registration* of the two SLCs. It means that, for each imaged target in one SLC image, we have to register (or match), with a sub-pixel accuracy, the same target in the other SLC, because "*any ground objects do not usually locate at the same pixel coordinates in each SLC image*" (Furuya, 2011, p.1044). In practice, the offset in range and in azimuth directions must be found and then implemented to make the second SLC (the slave) match the first (the master) by resampling the slave. This is a key step, non-trivial at all because of the different look angles and skewed SAR trajectories involved (Massom and Lubin, 2006). The quality of final interferogram depends on the quality of the co-registration.

To co-register accurately two SLCs, precise knowledge of the offset between the two images is required. There are diverse ways to deduce this offset but it is usually carried out in two stages (Massom and Lubin, 2006):

A **coarse matching** has to be first led in order to obtain offsets in range and azimuth with an accuracy of a few pixels. These initial offsets are obtained either by cross-correlation of the SLCs (with the GAMMA function *init_offset*) or based on orbit data related to the SLCs (this is done with the GAMMA function *init_offset_orbit*). There is finally an alternative way, in case the two GAMMA functions do not work, it consists in displaying the two SLC images and determining visually an approximation of the offset.

Figure 3.3: Principle of co-registration (Furuya, 2011, p.1043). The Slave image is resampled to match the master image. The residual offset is considered as displacement.

At the next stage the coarse matching is refined by **fine co-registration** whereby the matching reaches sub-pixel accuracy levels, "*typically by comparing roughly corresponding areas and solving a set of local transformation parameters*"(Massom and Lubin, 2006, p.81).
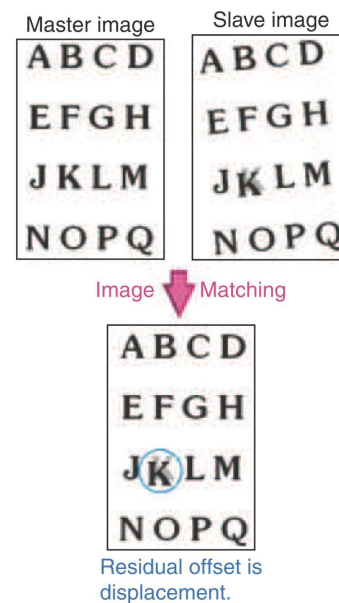
There are also several ways to achieve this step and, in our case, the offset determination was based on correlations in intensity (with the GAMMA function *offset_pwr*).

Once the offsets are determined, the SLC-slave is resampled to match the master (with the function *offset_fit*) and the phase and amplitude information is recalculated. For more information about this crucial initial step please refer to literature (e.g. Massonnet and Feigl, 1998, Massom and Lubin, 2006) or to GAMMA reference manual (Wegmüller and Werner, 2007).

3.1.3   Complex interferogram generation

Even though the computation of the complex interferogram is the central step of this section, additional operations are required either upstream or downstream. All the steps related to the generation of the interferogram are presented in here. This includes: common band filtering, interferogram flattening and reduction of phase noise. Moreover, we also detail how an interferogram should be interpreted and finish the section with a word about coherence.

A)   Common spectral band filtering

Since the perpendicular baseline between the sensor positions is hardly ever zero, the same scene is viewed under slightly different look angles for the two acquisitions. As a result, a frequency shift is introduced between the signals received by the two radars. "*The consequence is that the two signals do not fully correlate, i.e. in other words the interference pattern between the images is somewhat corrupted.*" (Wegmüller and Werner, 2007, p.11)

The *common spectral band filtering* aims at correcting this effect: a filter is applied to remove the uncorrelated contribution (Ferretti et al., 2007) of the two signals, by preserving frequencies within a certain range and rejecting frequencies outside the range.

B)   Interferogram computation

The interferogram is formed by multiplying each complex pixel of the master SLC by the complex conjugate of the corresponding pixel in the slave SLC. Supposing E_1 and E_2 are the complex signals (backscattered to the sensors) of two co-registered master and slave SLCs, the interferogram generation can be expressed like this (based on equations (2.7)

and (2.8)) (Høgda et al., 2011, Furuya, 2011) :

$$E_1 E_2^* = E_{0,1} e^{i\phi_1} . E_{0,2} e^{-i\phi_2} = E_{0,1} E_{0,2} . e^{i\Delta\phi} = E_{0,1} E_{0,2} . e^{i\frac{4\pi\Delta R}{\lambda}} \tag{3.1}$$

E_2^* denotes the complex conjugate of the slave E_2, $E_{0,1}$ and $E_{0,2}$ correspond to the amplitude of the complex signals. We see from equation (3.1) that an interferogram is thus a complex image whose argument corresponds to the interferometric phase (i.e. $\Delta\phi$, the phase shift, see chapter 2) and whose modulus is a measure of the cross correlation of the images.

C) Interferogram flattening

This operation consists in removing the orbital contribution to the interferometric phase (cf. equation (2.9)). The interferogram is *flattened* by subtracting the expected phase from a surface constant elevation on a spherical earth (Bürgmann et al., 2000, Simons and Rosen, 2007), leaving thereby only fringes related to changes in elevation, surface displacement and noise. To do so, a precise estimation of the perpendicular baseline is needed (see equation (2.10)). Figure 3.4 presents an interferogram before and after flattening. In the unflattened interferogram 3.4a, most of the fringes (i.e. coloured contour lines of equal interferometric phase, cf. section 2.3) are parallel and close to each other. This is the typical pattern of orbital fringes, because the baseline varies across the scene. Once the interferogram is flattened (figure 3.4b, the orbital fringes leave room for fringes caused by topography and displacement). In what follows, (D) we present how an interferogram must be interpreted.

D) Interferogram interpretation

An interferogram is an intermediate product of SAR interferometry but can still provide valuable information about topography and dynamics of a scene. There are three kinds of information we can deduce from interferogram showing ice shelves. Those are summarized in figure 3.5. The most visible information is the transition between the ice sheet and the ice shelf. The boundary, or in other words the grounding line, is very recognizable as it is a long, continuous and narrow band of several fringes (part (c) in figure 3.5). Such fringes are caused because tidal displacements affects the ice shelf but not the ice sheet. Secondly, the fringes on the sea-side (figure 3.5 b)) of the grounding line, thus belonging to the ice shelf are typical motion-related fringes. Ice shelves are indeed too flat to provoke such close

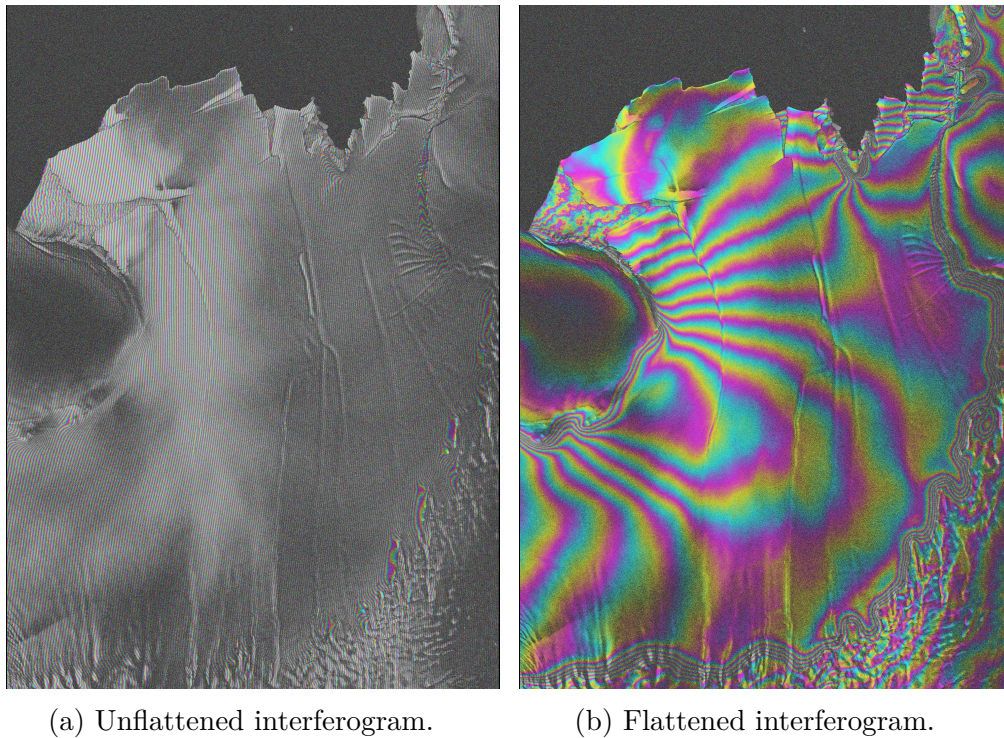(a) Unflattened interferogram.   (b) Flattened interferogram.

Figure 3.4: <u>Interferogram showing an ice shelf before and after flattening.</u> The colour lines depict the interferometric phase, forming *fringes* (=isophase lines), while the brightness of the interferogram depends on the coherence. The bright/coloured portion of the images (in the lower part) corresponds mostly to the ice shelf, whereas the dark portion is the ocean and has a very low coherence. The unflattened interferogram (a) is dominated by orbital fringes, whereas the flattened interferogram displays information about motion and topography. (Figure 3.5 describes how to interpret a flattened interferogram). Please note that the images are still in radar coordinates.

topographic fringes. And finally, on the ice sheet, we find typical topographic fringes where ice flows very slowly, for instance on the promontory highlighted by figure 3.5 (a).

E)   Interferogram filtering and phase noise reduction

The goal of filtering the interferogram is to reduce phase noise in order to make the phase unwrapping more robust and simpler (Wegmüller and Werner, 2007). There are different non-exclusive ways to achieve this objective. Two filtering techniques are detailed below: interferogram multi-looking and interferogram filtering.

Multi-looking   Multi-looking is the operation that averages spatially the complex values of neighbouring pixels with a moving window of a fixed dimension. It is an important step that improves the Sound to Noise Ratio (SNR)[4] by reducing the standard deviation of the interferometric phase. It also improves the computational efficiency because it creates

---

[4]The Sound to Noise Ratio (SNR) is a measure that compares, with a ratio, the level of desired signal (sound) to the level of background noise.
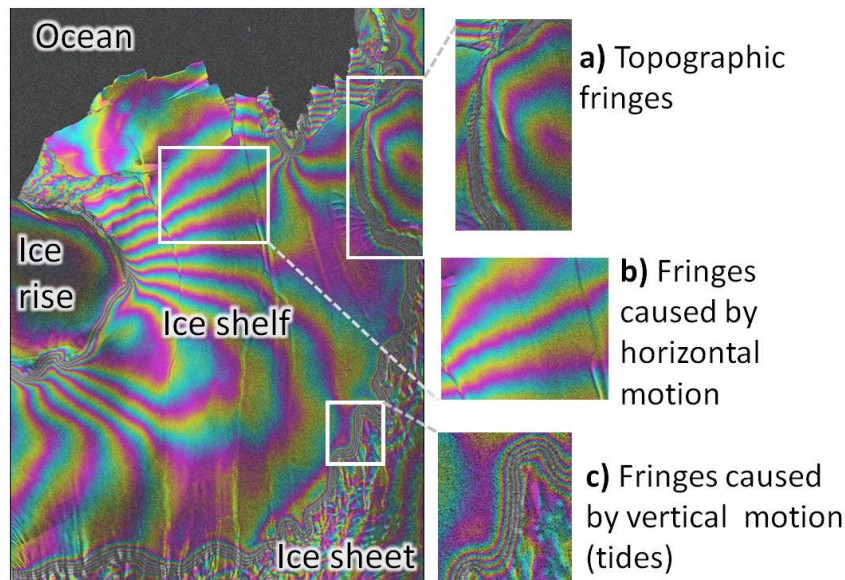
Figure 3.5: <u>Interpretation of a flattened interferogram</u>. The figure presents the different elements visible on an interferogram:(**a**) topographic fringes on the ice sheet; (**b**) horizontal-motion fringes on the ice shelf and (**c**) vertical motion fringes due to tidal displacement at the transition between ice sheet (or other grounded features) and ice shelf. (The interferogram is not geocoded.)

more manageable datasets but at the expense of spatial resolution (Massom and Lubin, 2006). It allows moreover to set the problem of differential range and azimuth resolutions by obtaining square pixels. Following Massonnet and Feigl (1998, p.455), "*for a typical pixel size of 4 m along the track and 20 m across, 2 looks in range and 10 looks in azimuth, for a total of 20 looks, is a reasonable choice.*" That was the choice for this thesis.

Adaptive filtering   Filtering aims at reducing phase noise and thus improving coherence without degrading spatial resolution. This is done by an algorithm based on Goldstein and Werner's (1998), which designs a filter based on the power spectrum of the interferogram. For more information about adaptive filtering, please refer to the *adf* function in ISP reference guide (Wegmüller and Werner, 2010b).

F)   Coherence

We have seen in the previous chapter (cf. 2.3.2) that the coherence provides a measure of the quality of the interferogram. During the generation of the interferogram, the coherence is also computed and determines the brightness of a complex interferogram. One practical application of coherence is its use to generate a validity mask (with the GAMMA function rascc_mask) for the phase unwrapping. A mask is an image whose hue corresponds to the coherence level except for the pixels with a coherence value below a chosen threshold (0.3 in

our case), in this case they appear in black (i.e the value is null) (Wegmüller and Werner, 2010b). During the phase unwrapping, the phase of the masked pixels (in black) is not calculated.

3.2   Motion retrieval

Although motion retrieval typically belongs to the Differential Interferometric SAR (DInSAR) technique[5], a few functions are also linked to classical InSAR. The steps needed to extract motion from an interferogram are illustrated in the lower grey part of figure 3.2. The technique used in this thesis is called the *2-pass differential interferometry without phase unwrapping* but it is good to know that other techniques to differentiate motion and topography exist (cf. previous chapter or Wegmüller and Werner, 2008). The processing method applied in this thesis works with two interferograms and one external DEM in input, and the topographic contribution is removed from the wrapped interferogram. After having isolated the motion contribution in the interferogram, two ambiguities need to be resolved. First, the intrinsic 2π-ambiguity of the phase needs to be addressed by phase unwrapping. Secondly, the unwrapped phase obtained needs to be calibrated (i.e. absolute phase needs to be deduced) because the unwrapped interferogram only records relative changes in phase which means that the contour of null deformation cannot be identified (Massonnet and Feigl, 1998). Once calibrated, it is possible to convert easily the interferogram to geophysical measurement and geocode it to ensure a successful data exportation.

3.2.1   Separation of motion and topography

The operation of removing topography from the interferogram takes place in two steps: first, an unwrapped topographic phase shift ($\Delta\phi_{topo-sim-unw}$) is simulated thanks to an external DEM, then the $\Delta\phi_{topo-sim-unw}$ is subtracted from the complex interferogram which leads to a *wrapped differential interferogram.* In practice, to simulate the topographic contribution, the DEM needs to be previously reprojected into SAR geometry and baseline information is required to simulate the interferometric fringes (Wegmüller and Werner, 2008).

---

[5]DInSAR aims at separating motion and topography from an interferogram and produces differential interferograms (with the motion contribution isolated in our case.
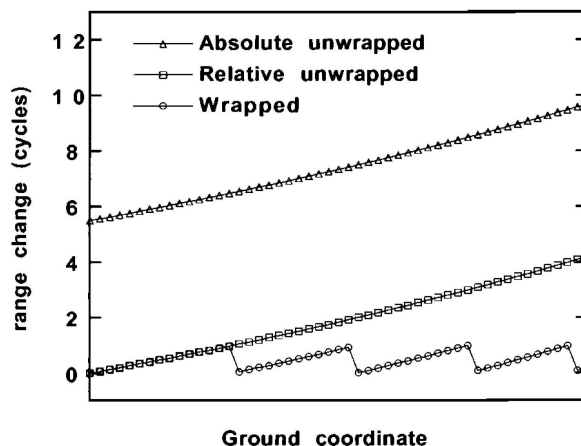
Figure 3.6: Three types of phase measurements (Massonnet and Feigl, 1998, p.453). This image shows profiles of range changes measured by three types of phase measurements: absolute unwrapped (triangles), relative unwrapped (squares), and wrapped (circles) phases. The absolute and relative unwrapped phases differ by a constant offset. The wrapped phase is confined in one range cycle (i.e. phase changes only between $[-\pi, \pi]$) and corresponds to modulo 2π of the relative signal. If we exclude the discontinuities of the wrapped phase, all curves have the same slope.

3.2.2 Phase unwrapping

Phase unwrapping is the most crucial step in SAR interferometry because this operation enables to recover continuous phase information from discrete wrapped phase (Wegmüller and Werner, 2007, Massom and Lubin, 2006). As interferometric phase is only known to *modulo* 2π (cf. chapter 2 and figure 3.6), it is necessary to add to each pixel the correct multiple of phase cycle (i.e. of 2π) so that the phase shift in slant range can be derived. An important assumption made for the unwrapping is that the phase field is relatively smooth, which means that there is no jumps of the unwrapped phase (Massom and Lubin, 2006, Wegmüller and Werner, 2007). It implies mathematically that interferometric phase differences should range between $-\pi$ and π, between adjacent samples. In principle, the unwrapped phase can be obtained by a path-independent integration of phase gradients or, in other words, by counting the fringes along a path starting at a reference point and adding to the wrapped phase, 2π times the number of fringes from the start. However in practice difficulties are introduced by jumps in local phase gradients ($|\Delta\phi| > \pi$). Such leaps are caused by noise, insufficient sampling rate or discontinuities (Wegmüller and Werner, 2007).

Although different algorithms exist for the phase unwrapping, this thesis exclusively used the Minimum Cost Flow (MCF) algorithm, developed by Costantini (1998). It is based on a global optimization technique with minimal user-computer interactions (Wegmüller and

Werner, 2007). "*It aims to locate a phase unwrapping path through the interferogram that minimizes the number of global phase-unwrapping errors*" (Massom and Lubin, 2006, p.87). MCF takes into account the coherence of the interferogram as a weight factor to calculate where discontinuities are preferred (Wegmüller and Werner, 2010b). That is why regions of low coherence and thus low weight have low costs for phase jumps (discontinuities), on the contrary to area with high coherence. Phase unwrapping is the processing step that requires the greater computational power, for this reason it is not useless to mask areas with low coherence.

Remark In case of *2-pass differential interferometry without phase unwrapping* processing method, phase unwrapping is performed after the removal of topography which gives according to Wegmüller and Werner (2008), more robust differential interferogram and fringe pattern easier to unwrap, compared to the original interferogram.

3.2.3   Calibration

The relative unwrapped phase obtained by phase unwrapping needs to be calibrated to derive ice displacement. As the count of the fringe number depends on the starting point, calibration is indeed required to identify fringes of zero phase change (i.e. zero motion). As we see in figure 3.6, relative and **absolute unwrapped phase** only differ by a constant offset. To calibrate the unwrapped phase, we need at least one Ground Control Point (GCP), i.e. a point whose location is precisely known and for which it is possible to deduce an unwrapped phase value. There are two ways to get GCPs: either thanks to independent measurements of velocities at precisely known locations or we can also make assumption of a zero speed at specific points, for instance at stationary ice-free areas (Rosen et al., 2000) or at the top of grounded features (ice rises, pining points etc.), tidal uplift makes this task more difficult (cf. section 3.4). Anyway it should be noted that finding calibrating points is not always an easy task: Antarctic ice shelves are remote areas, in-situ measurements are therefore sparse and it is also very hard to find exposed rocks within the ice shelf.

In our case, we used Global Positioning System (GPS) measurements from the *Buttressing effect: Why ice shelves are essential? (Be:Wise)* campaign field (cf. section 4.3) for the scene related to the 3D-flowfield. Although it seems easy, in theory, this stage can be tricky to achieve because angles needed are expressed in different units (radians><degrees), they are defined with respect to different directions (easting><northing), angles increase clockwise vs anti-clockwise etc. For all these reasons a more detailed explanation is worth.

Calibration with GPS points This operation requires a precise knowledge of the velocity measurement, its location, and its orientation. Starting from these data, one python script (*rangeflow_correction_lookvectors.py*) is used to calculate the unwrapped phase offset, and then, another python script (*substract_constant_offset.py*) is needed to subtract the offset from the relative unwrapped phase interferogram. These two scripts were adapted from Neckel's (2010) thesis.

To retrieve the offset value, one must project the horizontal[6] velocity of the GCP (V_{gps}) on the Line of Sight (LOS) (see figure 3.7). This involves projecting V_{gps} on the ground range direction (i.e. the horizontal projection of the LOS), which provides $V_{g.r}$ (figure 3.7b):

$$V_{g.r} = V_{gps} \cos \beta \tag{3.2}$$

where β is the angle between V_{gps} and $V_{g.r}$, it corresponds to the difference $\beta = \alpha - \Phi$, if α and Φ represents the orientation angles, with respect to east, of the two vectors.

The second step is to project $V_{g.r}$, the ground range projection of V_{gps}, on the slant range direction to obtain $V_{s.r}$ as it is depicted in figure 3.7c:

$$V_{s.r} = V_{g.r} . \cos \Theta \tag{3.3}$$

Θ being the elevation angle. It should be noted that Φ and Θ are in capital to avoid the confusion with ϕ and θ, the phase and the look angle, respectively. The names of these two Greek letters has nevertheless been maintained because it is their denomination in GAMMA. Φ and Θ values are extracted from images produced by the GAMMA function *look_vector*. However, Φ and Θ value extraction involves a previous transformation of the GPS coordinates into SAR coordinates. This conversion is required to find the pixel corresponding to elevation and orientation angles of the GPS point in the unwrapped interferogram (not geocoded yet).

Once we have the speed projected onto the LOS, it should be transformed in displacement value in slant range ($\Delta r_{r.s}$) by multiplying it by the temporal baseline (T), before finally getting unwrapped phase values ($\Delta\phi_{gps}$) when multiplied by the factor $\frac{4\pi}{\lambda}$ (see equa-

---

[6]As we deal with ice shelves vertical displacement speed has been neglected, because we were not interested in tidal motion. The calibration is therefore used to remove tidal effect on velocities.
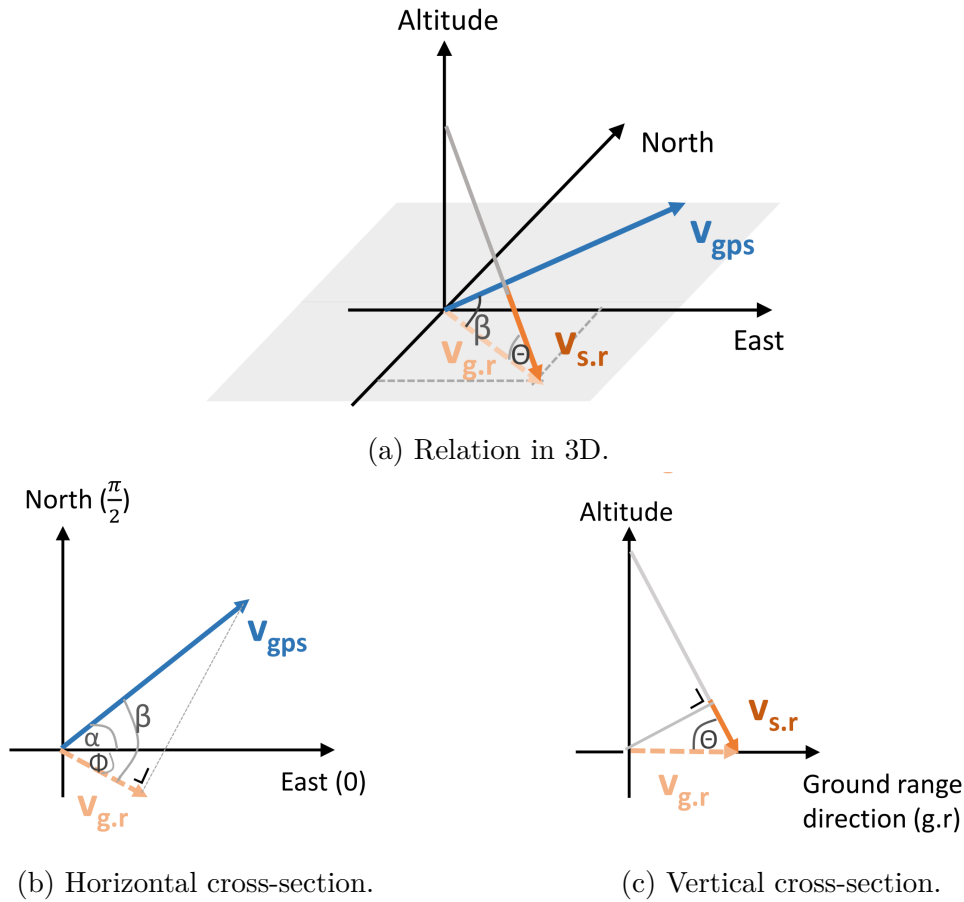
(a) Relation in 3D.

(b) Horizontal cross-section.

(c) Vertical cross-section.

Figure 3.7: Relation between the GPS derived velocity (V_{gps}) and their projection on the satellite LOS ($V_{s.r}$). V_{gps} is first projected on the ground range direction ($V_{g.r}$), on the horizontal plan. $V_{g.r}$ is then projected on the slant range direction. Θ is the elevation angle and β the horizontal angle between the GPS motion and ground range directions, it depends on the angles α and Φ.

tion (2.13)). This operations allows to retrieve the constant offset k:

$$k = \Delta\phi - \Delta\phi_{gps} \tag{3.4}$$

that will be subtracted from the relative unwrapped interferogram to get an absolute unwrapped interferogram.

If no in-situ measurements are available, the alternative way is to calibrate the unwrapped interferogram, assuming a zero displacement at a specific place.

Calibration based on zero motion assumption : This kind of calibration is much easier to perform but rely on the presence of particular features in the scene. Once we have found spots where zero motion can be assumed, it is then easy to retrieve the constant offset: we just have to look at the value of the unwrapped interferogram at these precise points to get directly the constant offset expressed in unwrapped phase values. As previously said,

there are only a few kind of features where displacement can be assumed to be null: exposed bedrock and top of pinning points/ice rises.

3.2.4 Surface velocities deduction and geocoding

With the previous step, we obtained an absolute unwrapped interferogram which means that interferometric phase has a meaning in term of displacement. From equation (2.13) it is straightforward to deduce **displacement** values (in slant range):

$$\Delta r_{s.r} = \frac{\lambda.\Delta\phi}{4\pi} \tag{3.5}$$

If we divide displacement images by their temporal baseline ($T = 1$ day in our case), we can produce 1D-velocity images. Positive values indicates displacements/velocities towards the sensor (Wegmüller and Werner, 2008). This operation was performed with de GAMMA function *dispmap*.

As most (D)InSAR products are expressed in SAR coordinates, we have so far called them *images*, but it is possible to transform them into *maps*. This operation is the **geocoding**: each point defined in SAR coordinates is resampled into a standard map projection system (Wegmüller and Werner, 2008). The chosen map projection was the *WGS 84 / Antarctic Polar Stereographic* (EPSG=3031) projection. This operation requires the use of a DEM, for more information, refer to (Wegmüller and Werner, 2010a). Once transformed into map, the results obtained are widely exportable because they are spatially referenced (=georeferenced) and they can be loaded into a Geographical Information System (GIS) to be used in combination we other spatial information.

3.3 Derivation of three-dimensional ice flow

We have seen it in chapter 2, SAR systems are side looking and InSAR technique enables to retrieve 1D-displacement in LOS. As a result, InSAR is not able to measure displacement along the flight track of the sensor (Rott, 2009). It also means that three linearly independent satellite passes need to be combined to determine fully the 3D components of the velocity vector (Joughin et al., 1998). It is nevertheless desirable to need less than

three passes to derive 3D-flowfield. Starting from the equation of a velocity vector :

$$\vec{v} = v_x \overrightarrow{1_x} + v_y \overrightarrow{1_y} + v_z \overrightarrow{1_z} \tag{3.6}$$

(v_x, v_y and v_z are the velocities in x, y and z directions, with $\overrightarrow{1}$ indicating unit vectors in these directions). This equation can also be rewritten as follows, if we gather the two horizontal components of the velocity into one horizontal vector $\overrightarrow{v_h}$:

$$\vec{v} = \vec{v_h} + v_z \overrightarrow{1_z} \tag{3.7}$$

Starting from equation (3.7), Joughin et al. (1998) have demonstrated that it was possible to deduce information about the velocity vector, combining interferometric data from ascending and descending satellite passes, provided to know the surface slope. Their demonstration relies indeed on the assumption of a flow parallel to the ice-sheet surface. The latter allows then to relate unequivocally horizontal velocity to vertical velocity. Overall, it is possible to retrieve a three dimensional velocity field from two linearly independent satellite orbits passing above the same scene, which is the case with ascending and descending orbits. The need of a third independent observation geometry has however to be replaced by the use DEM, to take into account the surface slope.

The combination of two 1D-displacement maps was performed with the function *dispmap_vec2* in GAMMA.

It should eventually be noted that for ERS satellites, horizontal motion in East-West direction is much more accurately determined than North-South motion (Wegmüller and Werner, 2008). ERS have indeed a near-polar orbit, which means that the satellites fly over a scene northward (ascending) or southward (descending) (see chapter 4). Knowing that a SAR system is side-looking, the horizontal projection of the LOS (=ground-range) is more likely to have an East-West orientation than North-South. As a result, the sensitivity (and thus accuracy) to an East-West motion is higher than North-South displacement.

3.4 Particularities of the floating ice shelves

Particularities of ice shelves for flowfield deduction have been mentioned several times. We know, by definition, that an ice shelf is a floating extension of an ice sheet. This means that tides affecting ice shelves cause vertical displacements that are included in the total

interferometric phase and that complicate the deduction of horizontal flowfields of the shelf. There are two main reasons behind the strong sensitivity of the interferometric phase to vertical displacement :

- As the look angle of the ERS SAR sensor is steep (about 23°), its sensitivity to the vertical motion is very high, that is why transition zones between grounded and ungrounded feature are easily detectable on an interferogram.

- Moreover, Goldstein et al. (1993) explained that interferometric phase is more sensitive to tidal uplift than to horizontal displacement because instantaneous vertical velocities caused by tidal movement are considerably greater than horizontal flow velocities.

As a result the decomposition of the displacement into two horizontal components is corrupted (Mohr and Madsen, 1997). Another kind of corruption can also be introduced through different tidal uplift in the two interferograms (ascending and descending).

For the sake of simplicity, we neglected the role of the tides by assuming a parallel vertical displacement. This assumption can partly be verified by counting the number of fringes at the grounding line, a constant value along the grounding line would support the assumption. Furthermore, we masked (removed) the velocity of grounded feature as they were not affected by tidal uplift and so would have need a special calibration, and this because the offset we found during the calibration step also compensate for the tidal displacement. But, on the other hand, this means that calibration with zero-motion points is very difficult on the ice shelves, since grounded features where no motion can be assumed are not affected by tides, unlike ice shelves.

Remark: From now on, we will not talk about 3D-flowfield anymore, but rather about **horizontal flowfield** as we are not interested in the tidal displacement of the ice.

Chapter 4

Datasets

This chapter provides a brief description of the data used in this thesis:

- SAR data: needed as input for the interferometric processing.

- DEM: used to remove the topographic contribution in an interferogram and needed to geocode our images.

- 2012 field data: used to calibrate interferometric results and generate a local DEM.

- Radarsat mosaic: used as an overview map to visualize and help interpreting the results.

4.1 European Remote Sensing satellites 1 and 2 - tandem mission

We have seen in chapter 3, that interferometric processing started with Single Look Complex (SLC) images. The SLCs we used came from already processed Synthetic Aperture Radar (SAR) images. The satellites exclusively used in this study were European Remote Sensing (ERS) satellites 1 and 2. ERS-1 and ERS-2 are two satellites of the European Space Agency (ESA), designed to be identical twins[1] (D'Elia and Jutz, 1997, ESA, n.d.). ERS-1 was launched on 17 July 1991. As the satellite was successful, ESA decided to launch ERS-2 (on 21 April 1995), with the purpose of providing a follow-on of ERS-1 and ensuring continuity

---

[1]Besides showing different activity periods, the only difference between the two satellites is that ERS-2 carried an extra instrument, compared to ERS-1.

in the data (Duchossois and Martin, 1995). Because ERS-1 was remaining technically operational beyond expectations, it was even decided to operate the two spacecrafts in tandem, i.e. to adjust the two satellite orbits to make sure that ERS-2 follows ERS-1 with a 24 hours delay. This is known as the *tandem mission*, it lasted for around 9 months (from mi-August 1995 until mid-May 1996). The configuration of the tandem mission is a typical case of along-track repeat-pass acquisition geometry (see chapter 2). The tandem mission provided suitable data for ice sheet and glacier studies and, for this reason, was and is still very valuable for the field of glaciology (Massom and Lubin, 2006, Ferretti et al., 2007). Data acquired during the tandem mission present indeed several advantages (Duchossois and Martin, 1995):

- Since the temporal baseline equals 1 day, temporal decorrelation is minimized (due to similar acquisition conditions) and thus SAR images pairs are more likely to be coherent than what would have been achieved with a longer temporal baseline.

- The spatial decorrelation is also minimized because, spacecrafts are subject to more similar forces, the spatial baseline is consequently better controlled.

- The number of acquisitions within a repeat-cycle is doubled and the time interval between two acquisitions are strongly decreased which allows to better monitor fast flowing ice.

After the tandem mission, ERS-1 and-2 continued their operations and data acquisitions separately and were retired on March 2000 and September 2011, respectively. ERS-1

sensor parameters	symbol	**ERS-1/2**	units
Agency		ESA	
Launch		1991/1995	
Frequency	f	5.3	[GHz]
Wavelength	λ	5.6	[cm]
Orbit altitude		~ 780	[km]
Revisit time		35	[days]
Incidence angle	θ	23	[°]
Swath width		100	[km]
Along-track (azimuth) resolution	r_a	5	[m]
Across-track (ground range) resolution	$r_{g.r}$	20	[m]
Antenna dimensions	L_a	10x1	[m]
Pulse Bandwidth	$\mathcal{B}_c$	15.5	[MHz]

Table 4.1: Main ERS sensor parameters, from (ESA, n.d.).

and-2 carried various observation instruments including an imaging Synthetic Aperture Radar (SAR) and equipments to records satellites positions (for further details about the

instruments, please refer to ESA's website ESA, n.d.). Main technical features of ERS 1-2 SAR sensors are listed in table 4.1, the most important parameters are their 5.6 cm wavelength and 5×20m resolutions in azimuth and range, respectively. Both satellites had a near-polar orbits which means that during an orbital cycle (i.e. a full rotation of the satellite around the earth), ERS satellites passed nearly above each pole. One cycle can be divided into two passes: one northward, the *ascending* pass and the other southwards, correspond to the *descending* pass. Satellite orbits in combination with the rotation of earth (East-West), enabled to acquire images of the same scene from different look angle (Ferretti et al., 2007). Ascending and descending passes had indeed different viewpoints, because we have seen in section 2.2, that synthetic aperture radars were side-looking sensors. ERS antenna were right looking with an approximate look-angle of 23°. The combination of ascending and descending passes are particularly important to derive three dimensional (or horizontal) flowfields (see section 3.3). All the scenes used to generate interferograms
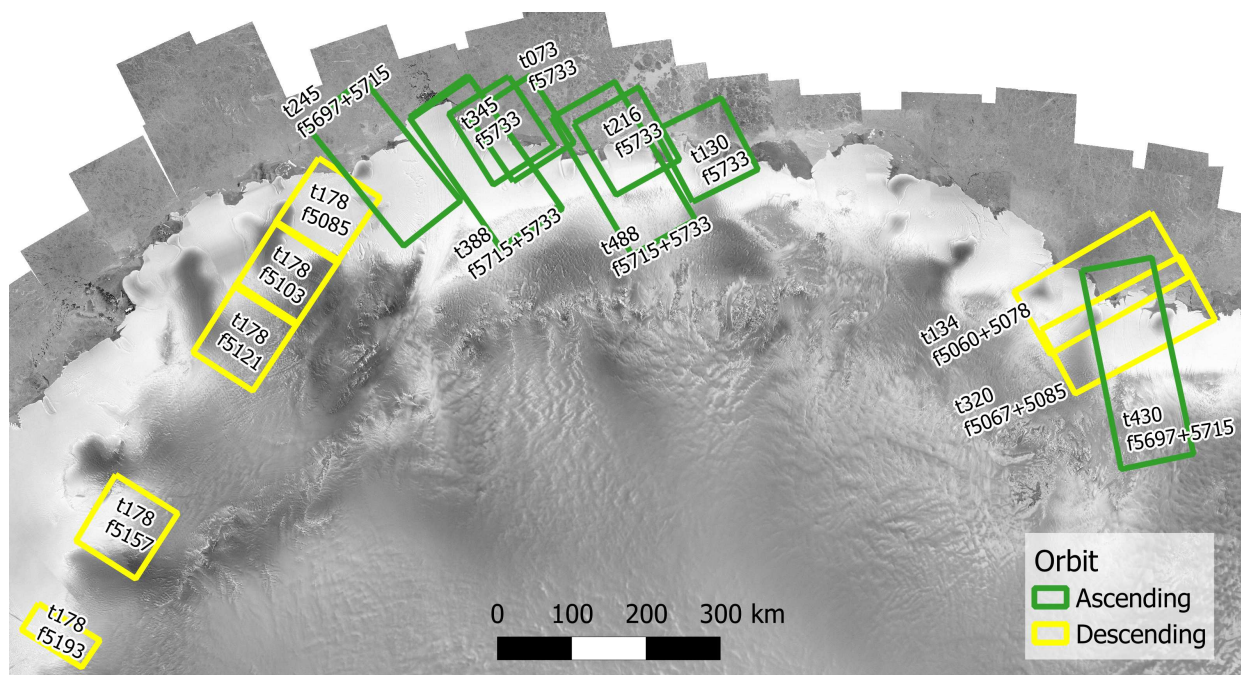

Figure 4.1: <u>Map of the ERS scenes analysed in the study</u>. The ESA references of the scenes are given through tracks and frames numbers. Ascending tracks are depicted in green and descending in yellow. Additional information is supplied in table 4.2. (The map in background is the radarsat mosaic (cf. section 4.4).

are showed in figure 4.1, additional information such as date of acquisition and status of slave/master are also provided by table 4.2. The data were chosen to cover major outlet glaciers in DML (Vestraumen in the west, Jutulstraumen in the centre, and Ragnhild in the east) as well as to fit ongoing field work. Each scene is referenced by its track number. Tracks are divided into different frames also designated with numbers. Table 4.2 shows

Track	Frame	Date	Pass	
073	5733	20-21/01/1996	Ascending	
130	5733	08-09/05/1996	Ascending	
134	5060+5078	03-04/04/1996	Descending	
178	5085	06-07/04/1996	Descending	
178	5103	06-07/04/1996	Descending	
178	5121	06-07/04/1996	Descending	
178	5157	06-07/04/1996	Descending	
178	5193	06-07/04/1996	Descending	
216	5733	09-10/04/1996	Ascending	
245	5715+5733	07-08/03/1996	Ascending	
320	5067	21-22/05/1996	Descending	MASTER
320	5067+5085	21-22/05/1996	Descending	MASTER
320	5085	21-22/05/1996	Descending	MASTER
345	5733	26-27/10/1995	Ascending	
388	5715+5733	11-12/02/1996	Ascending	
388	5715+5733	17-18/03/1996	Ascending	
430	5697+5715+5726	28-29/05/1996	Ascending	SLAVE
488	5715	02-03/06/1996	Ascending	

Table 4.2: References of the SAR scenes used. The table shows track and frame numbers, date acquisition and specifies if the orbit was ascending or descending.

that all the ERS data were collected between 1995 and 1996. We must finally precise that only two tracks were combined to derive horizontal flowfield The master track is *320* and the slave *430* (for track 320, the frames 5067 and 5085 were processed either together or separately, the separate frames of t320 were provided by ESA into the SLC form).

4.2   Digital Elevation Model

A Digital Elevation Model (DEM) is a 3D representation of a terrain surface, it usually takes the form of a raster where columns and rows correspond to x and y coordinates, respectively and where cell/pixel values represent the elevation and are displayed with a colour scale. DEMs have many applications in glaciology and are needed for several processing steps of SAR interferometry, especially for the *topography removal* and *geocoding* steps (cf. section 3.2). Moreover, as we made a parallel flow assumption to fully retrieve the flowfield (in section 3.3) a DEM is also required at the essential step.

In this study we mainly used the DEM from Bamber et al. (2009b), which is referred as *Bamber's DEM* throughout the thesis. Detailed descriptions of the data and method, on the one hand and of validation and error estimation on the other hand, are presented in Bamber et al. (2009a) and in Griggs and Bamber (2009), respectively. Bamber's DEM is covering the whole Antarctic continent with a gridding of 1 km. It has been formed by combination of spaceborne radar and laser data. Radar data were provided by the

Satellite Radar Altimeter (SRA) onboard the satellite ERS-1, while laser data came from the instrument Geoscience Laser Altimeter System (GLAS) onboard Ice, Cloud and land Elevation Satellite (ICESat). Such a combination of radar and laser measurements was performed to maximize vertical accuracy and spatial resolution. Radar altimeter provides indeed dense spatial coverage but relatively low vertical accuracy whereas laser altimeter shows higher vertical accuracy at the cost of lower spatial resolution (Bamber et al., 2009a). Elevation data were collected during 1994-1995 by the radar altimeter of ERS-1 and during 2003-2008 by the laser altimeter of ICESat. In addition to the creation of the DEM, Bamber and his colleague also assessed the accuracy of their DEM. To do so they used airborne altimeter data sets available to develop a multiple linear regression model with the variables known to influence elevation errors (Griggs and Bamber, 2009). Once obtained, their regression model enabled them to interpolate errors for the entire continent and thus to produce a map showing the error distribution of the Bamber's DEM. According to Griggs and Bamber (2009) ice shelves areas typically present errors of ~ 1 m.

4.3   Be:Wise field data

Buttressing effect: Why ice shelves are essential? (Be:Wise) is a research project under the supervision of the *Laboratoire de Glaciologie*, ULB. This project aims at examining the influence of ice grounded features, such as ice rises and pinning points, on ice sheet and ice shelf dynamics. The ongoing project is constituted of two fields campaigns on the Roi Baudouin Ice shelf (RBI) (see chapter 1). The first field campaign occurred during November-December 2012 and gathered various in-situ measurements on RBI. This thesis made use of two data types, they are presented on figure 4.2.

First, displacements of three points within the ice shelf were measured with GPS (cf. the bottom graph in figure 4.2) and the surface velocities were deduced. These three points are showed with the red arrows on the overview map, in the right part of figure 4.2. The fastest point (L4M5) served as Ground Control Point (GCP) for the calibration of the unwrapped phase (see section 3.2), while the two other points were used as validation point, to check the quality of final 3D-flowfield. The use of these points as GCPs relies on a steady-state flow assumption, or in other words, we assumed that the ice flow did not substantially changed between 1996 (the date of image acquisitions) and 2012 (the time of GPS measurements).

Other Be:Wise data served to generate, by spatial interpolation, a local DEM (see
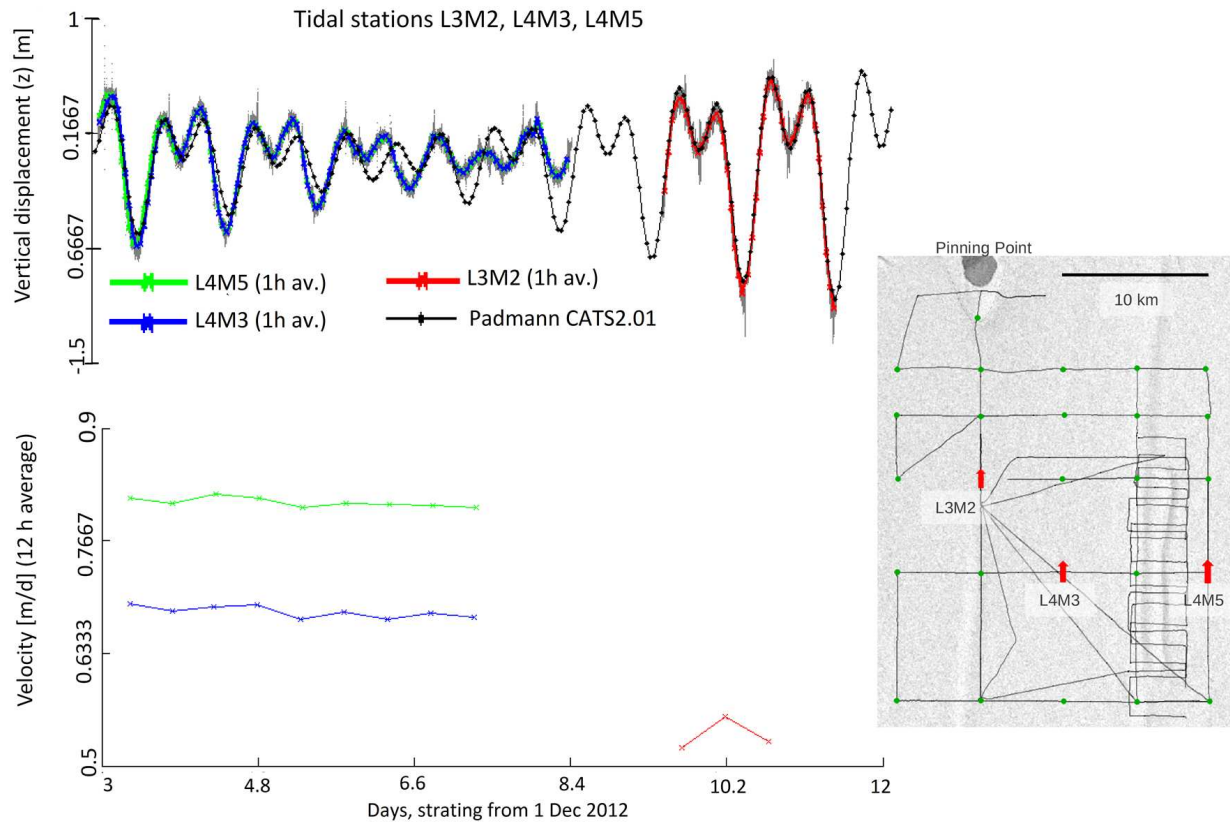
Figure 4.2: Data collected on the Roi Baudouin Ice shelf during the Be:wise campaign field (November - December 2012). The graphs show the velocity (bottom) of three points, measured by GPS and the vertical displacement (top) of the three points, compared to Padman et al.'s (2002) tidal model. On the right, there is an overview map that shows the ice shelf, seen from above, with the location of the three GPS points and the tracks of a GPS survey recording elevations in the area.

section 5.1.5). During the campaign, a GPS survey was performed to collect elevation at numerous sampling points along different tracks. The data were also collected on the RBI, as shown with the black lines on the right-side of figure 4.2. The survey site was chosen because it shows local topographic depression or trench which are invisible on Bamber's DEM.

Remark The top graph in figure 4.2 displays the vertical displacement relative to time of the three GCP/GPS points. Vertical displacement is assumed to originate solely from tidal motion of the ice shelf. Tidal elevations estimates from Padman et al.'s (2002) model are moreover superimposed on the graph (black line). We see that the model usually fits the measurements pretty well. There is only one point (L3M2) for which measurements and estimations disagree more. This particular point is located upstream of the pinning point. Moreover, the bottom graph, show no substantial temporal variation of velocities, at least on short timescales and if we except point L3M2 whose recording time is shorter and seems to vary more.
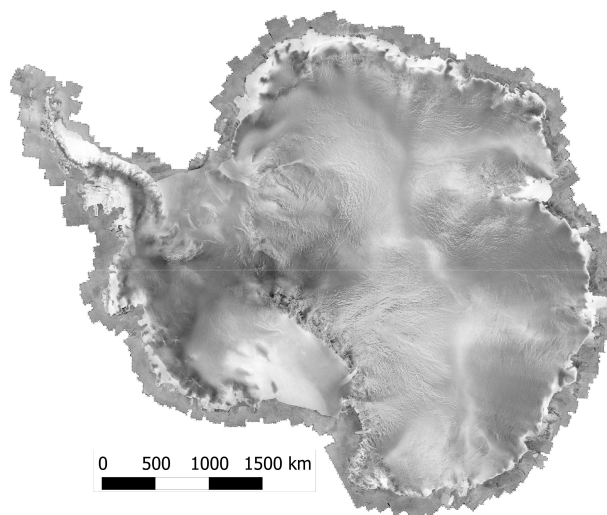
Figure 4.3: Radarsat mosaic of Antarctica

4.4   Radarsat mosaic

The *radarsat mosaic* (Jezek and RAMP Product Team, 2002) (cf. figure 4.3) is a SAR map that displays at high-resolution the entire continent of Antarctica. The map was formed by assembling numerous intensity SAR images[2] taken with the satellite Radarsat-1 in 1997. Radarsat is a satellite similar to ERS but, unlike ERS, which is only right looking, radarsat is characterized by a right and left looking geometry. This enables a greater coverage of the earth surface. Radarsat intensity images present in addition good contrast between sea ice, glaciers and rocky outcrops and enables to distinguish features such as crevasses within ice (Jezek, 2002). There are different versions of the mosaic with different spatial gridding. In our case we used the mosaic with a 250 m gridding, which served as an overview map. It was useful as background to display computed maps such as interferograms or velocity maps.

---

[2]It should be recalled that **intensity** SAR images represent the backscattered intensity (=amplitude^2) of the radar beam. They are very similar to black and white pictures but can be acquired in all weather conditions and during day- and night-time (see section 2.2).

Chapter 5

Results

This chapter presents our results. It is subdivided into two sections. The first part focuses on the Roi Baudouin Ice shelf (RBI) and presents very local results whereas, in the second section, we try to partly extend our result to the region of Dronning Maud Land (DML).

5.1 Roi Baudouin Ice shelf

We begin this section with an overview map (figure 5.1) recalling the spatial configuration of the RBI and underlining the location of several elements taken into account in what follows. After that, the ascending and descending interferograms of the RBI are showed and analysed. We then present the horizontal flowfield of the ice shelf and its related results, which includes a comparison with the GPS flow measurements for validation, and the derivation of the strain rates. We finally spend time, presenting a local DEM within the RBI. Before proceeding with the rest of the section, we would like to emphasize that T_1 and T_2, in figure 5.1 are particular topographic trenches not visible in Bamber's DEM, but localizable on SAR intensity maps (see figure 5.1). The role of these trenches will be discussed in the following chapter.

5.1.1 Interferograms

The first interesting results to show about RBI are the two flattened interferograms of the scene. As a reminder: a flattened interferogram displays, in a range between $-\pi$ and π, information about topography, displacement and other noise in the satellite LOS (see sections 2.3 and 3.1). Information from these two interferograms is supposed to be linearly
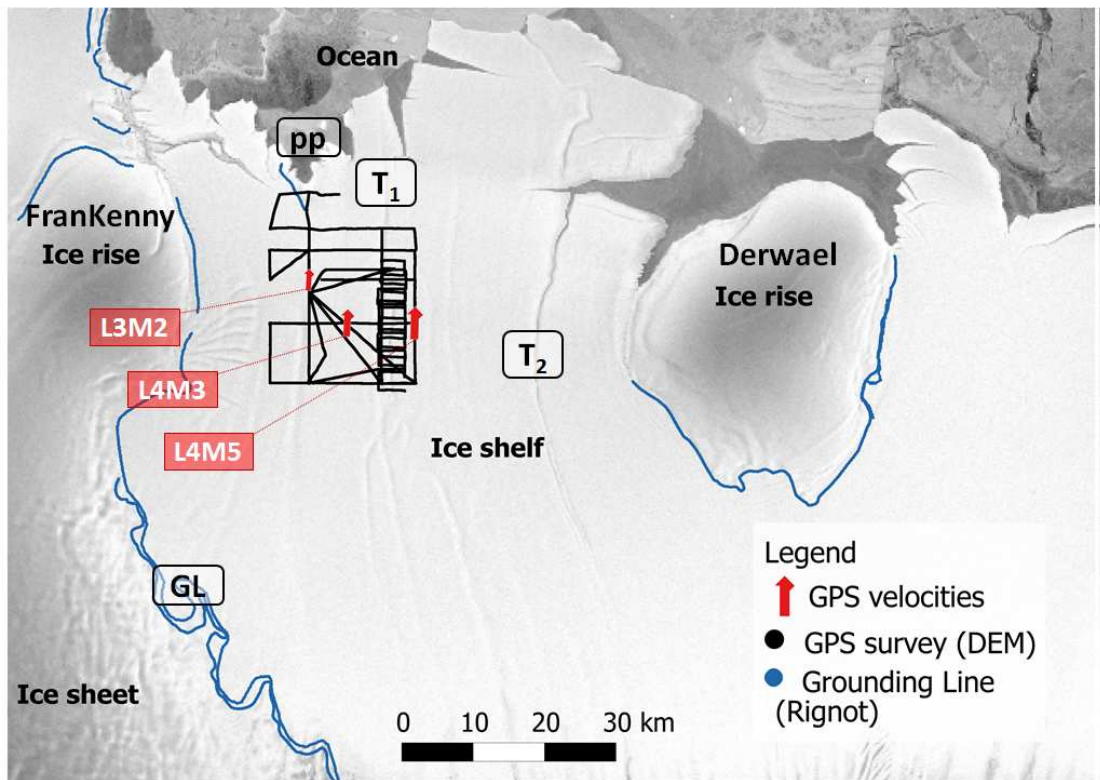
Figure 5.1: <u>Overview map</u> of the Roi Baudouin Ice shelf (RBI), showing in addition particular elements such as pinning point (pp), and trenches (T_1 and T_2) that will be discussed. The map also locates the GPS measurements used for different purposes. (GL=grounding line).

independent because, they originate from ascending (t430) and descending (t320) orbits. Figure 5.2 presents a map of each interferogram, the mask used to mark off the ice shelf for subsequent treatments is also shown.

The distinction between ice-covered surfaces and ocean is straightforward: ice-covered surfaces show a fringe pattern (coloured contour lines) while ocean shows a speckle pattern, due to lack of coherence (high phase variability) between the SAR acquisitions. It is then possible discriminate grounded (ice sheet, ice rises, pinning points) and floating ice. The limit manifests itself as a very dense fringe pattern caused by tidal motion (see section 3.1). Three limits of this kind are especially obvious in interferogram t430. They are situated in the north, the west and the east parts of the scene and enable to identify a pinning point (*pp* in figure 5.2), the grounding line (*GL*) and the ice shelf-ice rise boundary, respectively. Moreover, we would like to emphasize the presence of a specific pattern at the emplacement of the trenches.

5.1.2   Horizontal flowfield

Our main result is presented on figure 5.3, it consist of a high resolution map (50m) of the surface velocities of the Roi Baudouin Ice shelf.
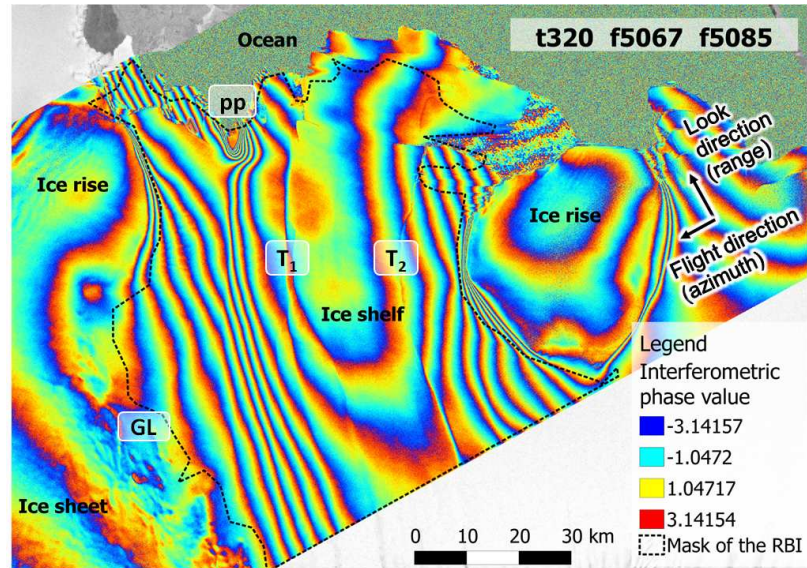
(a) Descending pass (t320).
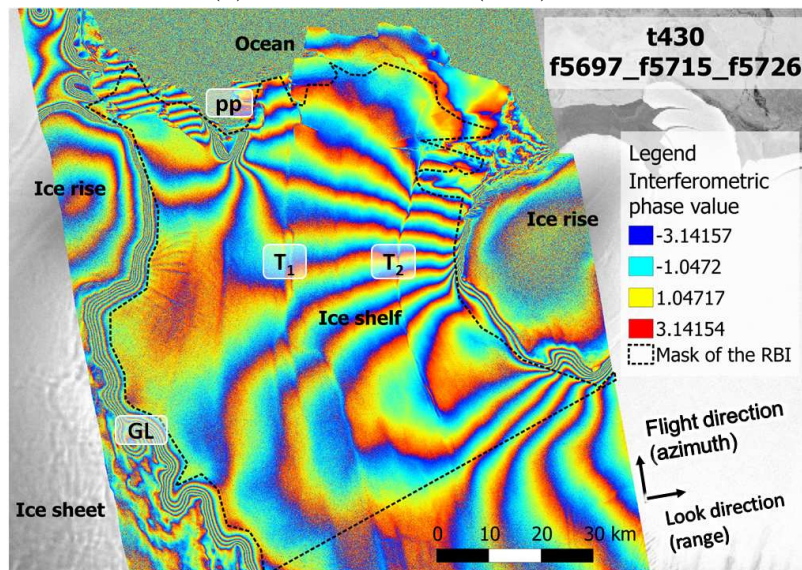
(b) Ascending pass (t430).

Figure 5.2: <u>Descending and ascending Interferograms</u> of Roi Baudouin Ice shelf (RBI). The shape delimited by the black dotted line is the mask used to mark off the ice shelf for subsequent treatments. Annotations have been superimposed to locate particular features: a pinning point (pp), the grounding line (GL) and topographic trenches (T_1 and T_2).
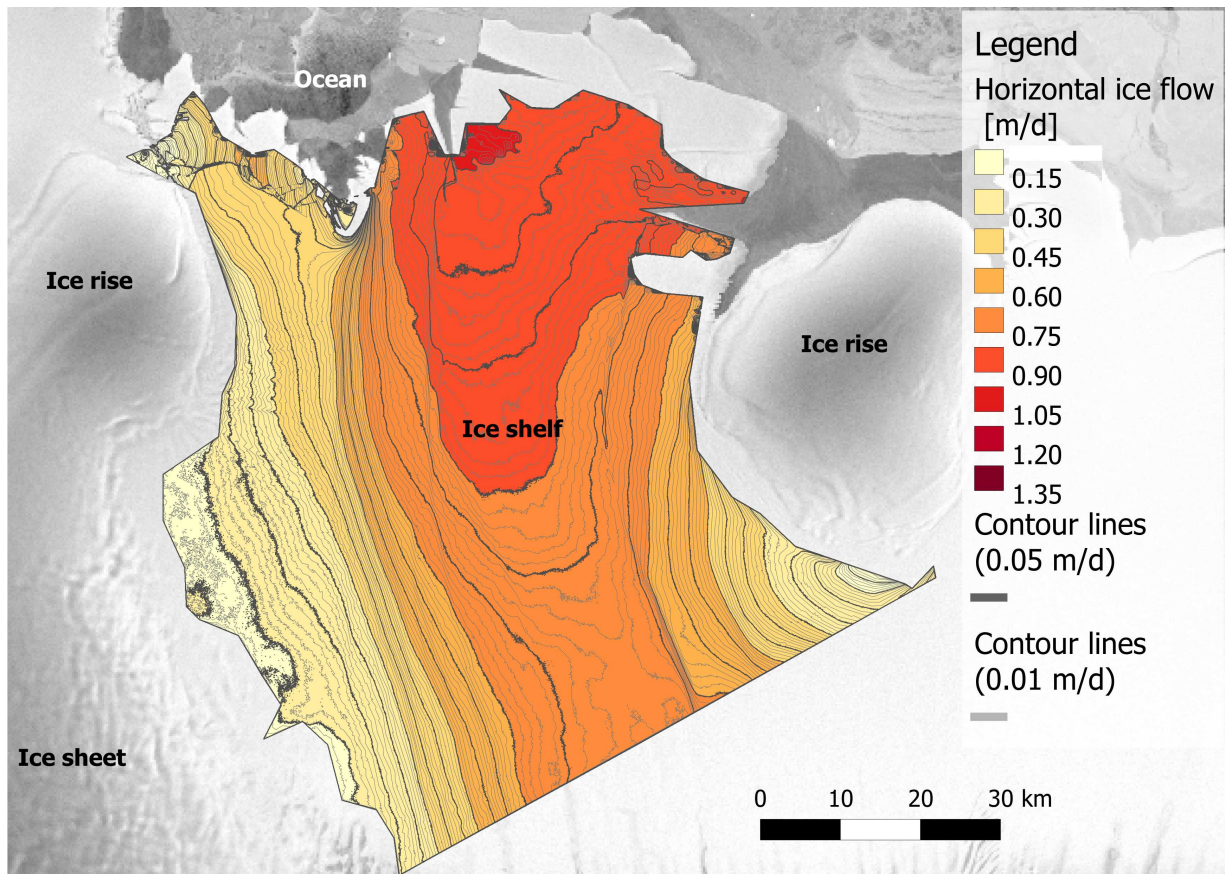
Figure 5.3: <u>Horizontal flowfield</u> [m/d] of Roi Baudouin Ice shelf. The resolution of the map is 50m.

The RBI velocities presented range from 0 to 2.36 m/d, with a 0.54 m/d average. Speed increases more or less regularly from the sides of the ice self to its centre and downstream. As a result, the fastest moving areas are situated in the middle of the ice shelf front. We see from figure 5.4a that velocities are not totally symmetrical to the central flowline: eastern velocities are faster than on the west side of the ice shelf. Besides small irregularities/slope breaks are observable around 12, 24 and 46 km in the profile. These particular locations seem to roughly correspond to the level of the pinning point, the trenches T_1 and T_2, respectively.

5.1.3 Horizontal flowfield and GPS measurements

We explained in the previous chapter that horizontal velocities and other related parameters were measured at three distinct points of the ice shelf (cf. figure 5.1). The easternmost and fastest point (L4M5) served as a GCP for the calibration of our unwrapped interferograms. As a result, two other GPS points remain to validate our flowfield, and examine the accuracy of the velocity measurements. We should however keep in mind that the use of GPS points
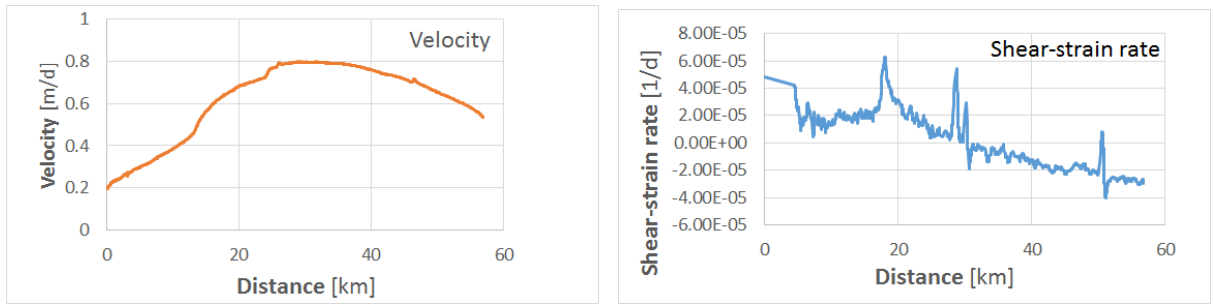
(a) Across-flow profile of the flowfield.

(b) Across-flow profile of the of the shear-strain rates map.

Figure 5.4: <u>Across-flow profiles of the velocity and shear-strain rates maps</u> The profile has been sampled from east to west, between the two ice rises, approximately in the middle of the ice shelf.

Points	$V_{GPS}[m/d]$	V_{INSAR} [m/d]	$V_{GPS} - V_{INSAR}$ [m/d]
L4M5	**0.812**	**0.809**	**0.003**
L4M3	0.682	0.680	0.002
L3M2	0.537	0.519	0.018

Table 5.1: <u>Comparison between GPS and InSAR flow measurements at the three GCPs.</u> The point used to calibrate the results appears in bold letters. (The location of the GCPs is presented in figure 5.1).

as ground-truth data requires a steady-state flow assumption. As explained in chapter 4, GPS data were collected in 2012 whereas SAR images were gathered in 1995-1996. We have therefore to assume that no significant changes in velocity occurred between these two dates, if we want to use the GPS points as GCPs. Table 5.1 proves that errors subsist in our flowfields, even after calibration. Our fitting is thus not entirely correct but the magnitude of uncertainty is still valuable. With a speed deviation of 3 mm at the point of calibration, the absolute deviation is estimated at 0.37%. Despite a similar deviation at the second GCP (*L4M3*), the deviation of the third one (L3M2), upstream of the pinning point, is much higher. It could either be due to a larger distance from the fitting point, which would mean a decrease of the fitting quality with distance from the calibration point, or increased deviation could be related to a more complex flow regime in the vicinity of the pinning point. The major error sources will be addressed in the following chapter (section 6.5).

5.1.4 Strain rates

Following Pattyn and Derauw (2002), we also calculated the strain rates (i.e. spatial deriva-tion of velocity). For each pixel in a local coordinate system (with y-axis oriented in the direction of the main component of the flow) we deduced the velocity gradient. Shear-strain
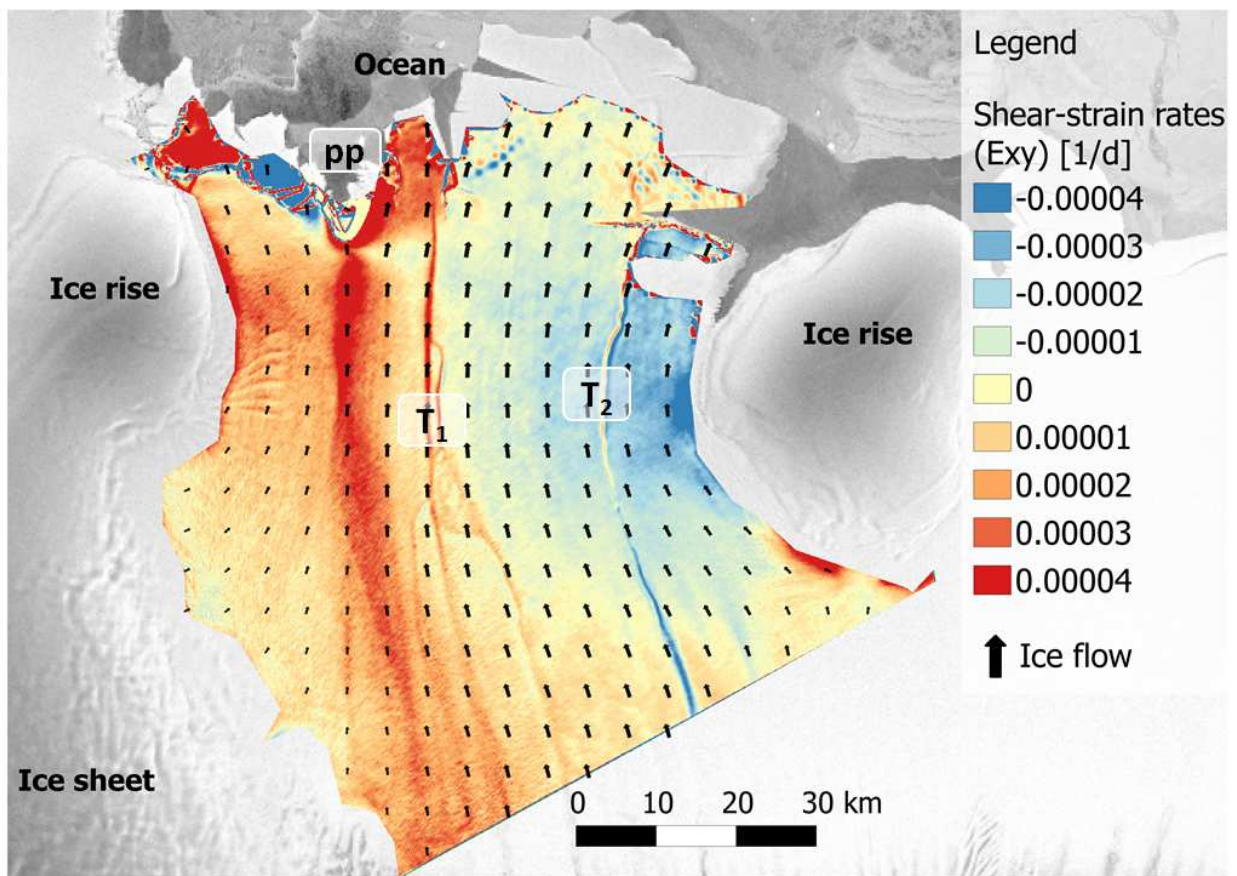
Figure 5.5: <u>Surface shear-strain rates</u> $\dot{\varepsilon}_{xy}$ $[d^{-1}]$ on Roi Baudouin Ice shelf, deduced from InSAR velocity results. The black arrows present the ice flow direction and its relative magnitude.

rates ($\dot{\varepsilon}_{xy}$) is defined as

$$\dot{\varepsilon}_{xy} = \frac{1}{2}\left(\frac{\partial V_y}{\partial x} + \frac{\partial V_x}{\partial y}\right) \tag{5.1}$$

where V_x and V_y are the horizontal components of the velocity in x and y directions. Surface shear-strain rates are presented in figures 5.5 and 5.4b. (Figure 5.5 also shows, with black arrows, the direction of the ice flow and its relative magnitude). The global aspect of the map is coherent: it is normal to have positive values on the west side and negative on the east, as the velocity profile (figure 5.4a) globally increases then decreases from the east to the west. There are three different things related to the shear-strain rates we would like to highlight.

First, the higher absolute shearing values are found around and upstream of the pinning point.

Secondly, at the level of the trenches the profile takes a suspicious saw-tooth shape, with positive and negative values in alternation, which suggests computations artifacts.

And finally, if we except the irregularities due to the pinning point and the trenches, we see higher shearing at the sides of the ice shelf. It should nevertheless be noted that, the coarseness of the mask may hide higher shearing at the side of the ice shelf.

The dynamics of the RBI seems therefore to be associated with lateral drag and mostly with drag caused by the pinning point.

5.1.5 Digital Elevation Model

In addition to the horizontal flowfield and its derivatives, a local Digital Elevation Model (DEM) was computed. This DEM was generated by interpolating elevation data of a 2012 GPS survey (cf. chapter 4). The GPS survey was realized in the vicinity of the pinning point and the trench T_1 (cf. figure 5.1). The goal of the GPS survey was to investigate the role played by the trenches on the ice shelf dynamics or on the result accuracy. We computed the DEM with the idea of generating new a horizontal flowfield (using the local DEM to remove the topographic phase contribution) to assess uncertainties related to the presence of these trenches. To be usable, the DEM needs however to be shifted backward, so that the trench configuration of 1996 is retrieved and processing uncertainties related to the non-inclusion of the trenches can be evaluated. Unfortunately, a lack of time prevented us from performing further analyses with the local DEM.

As the processing was completely unrelated to InSAR treatment, we preferred to present
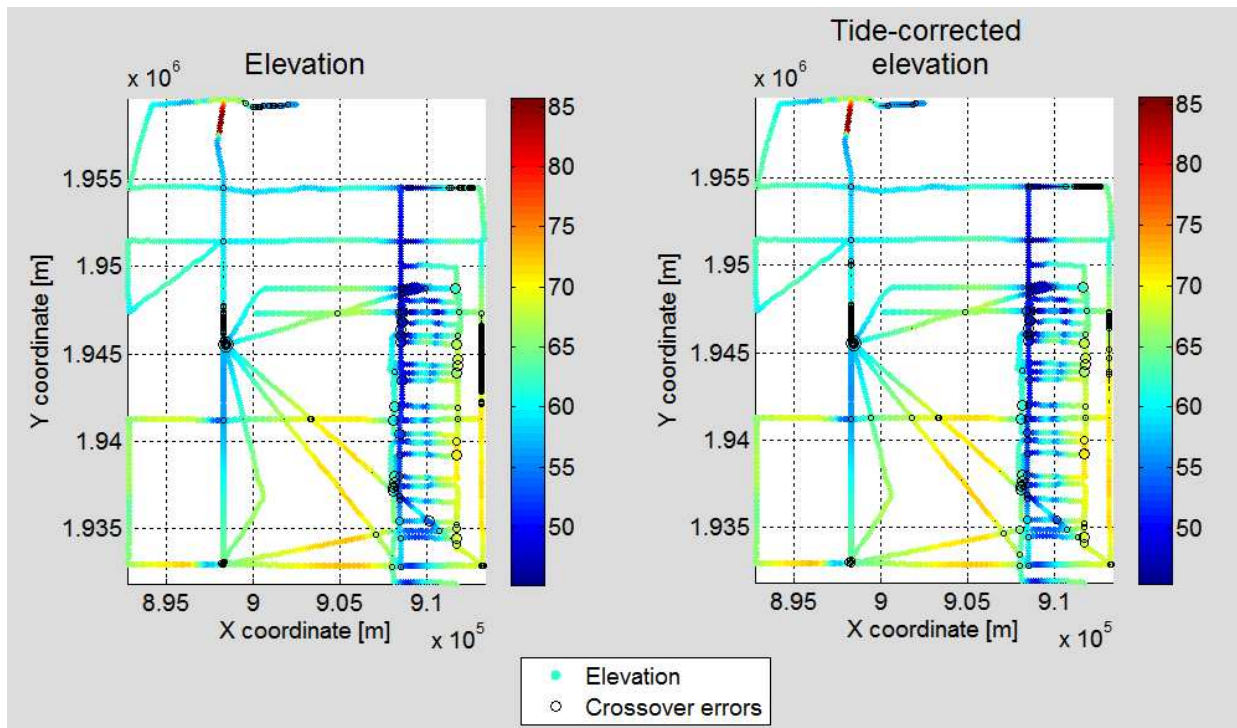
Figure 5.6: GPS survey and crossover analysis, with and without tide-correction. The graph on the left shows the measured elevations (in colour) during the GPS survey. Black circles were superimposed, to represent crossover errors, their size is proportional to the amplitude of the crossover error. The right graph displays the same information as the left one, only tidal effect was removed from measured elevations.

how we proceeded to get the DEM in this section.

A)   DEM generation

We first imported separately each track of the GPS survey in the *matlab* software. The data were then filtered to eliminate static points, and smoothed.

To compensate for differential tidal uplift during the survey, we used Padman et al.'s (2002) tide model. The model provided tide elevations according to the time, which were also imported in matlab. Tide elevations needed to be interpolated in time, in order to ensure compatibility with the GPS survey. The next step was to get a tide elevation correction for each point of the GPS survey, by combining time information from the two data sources. Once we got the correction factor, we were able to eliminate tidal effect on our data. Figure 5.6 shows the elevations measured along the tracks (left) as well as corresponding elevations corrected for tidal uplift (right). The order of magnitude of tidal uplift is unfortunately too small to detect colour differences in the two plots. Tidal correction ranges indeed between [-0.97;0.58] m with a 0.19 m average whereas elevation measurements are in the [45.15;85.72]m range. To verify the effectiveness of the tide-correction, we conducted, in

	Average	Standard deviation
ELEVATION	0.1708	0.79824
TIDE-CORRECTED ELEVATION	0.02201	0.70427

Table 5.2: Statistics of the crossover errors.

parallel, a crossover analysis for both datasets (corrected and uncorrected). The crossover analysis aimed at finding and calculating differences in elevation where GPS tracks overlapped. The calculations were carried out with the Generic Mapping Tool (GMT) software. The results of this analysis are superimposed on figure 5.6 by means of black circles, whose size is proportional to the crossover error. Statistics of crossover analysis (table 5.2) indicate that the tidal correction improves the result: the average of crossover errors significantly moves toward zero and the standard deviation also decreases but in a minor fashion. As a result tide-correction elevation should preferably be used. We explain the fact that tide-correction did not decrease significantly the standard deviation by the presence of noise in the data.

We finally obtained our local DEM after a spatial interpolation (in 2D). This was achieved with two different matlab functions: *griddata* and *gridfit.* Griddata, linearly interpolated the GPS tracks while gridfit which is based on a modified ridge estimator was used to get a smooth surface approximating data.

B)   DEM results

The two variants of the local DEM are presented in figure 5.7. The two subplots look globally similar, with nevertheless, a smoother appearance for the gridfit DEM. The only striking difference between the two DEMs in figure 5.7, is the presence of computational artefacts in the gridfit DEM. Such artefacts are fake topographic features introduced by the calculation algorithm during the DEM computation. They are depicted in figure 5.7 by grey numbers. From the figure it is possible to identify four non-existent topographic highs (1-4) and one fake depression (5). Figure 5.8 presents different profiles comparing the two computed DEMs (griddata and gridfit) with Bamber's. Profiles 5.8b and 5.8c, are sampled across the ice-flow and aim at examining the differences between the DEMs around the trench T_1. Profile b and c differ in their location: b is situated along one track of the GPS survey used to interpolate our DEMs unlike c. Griddata and gridfit DEMs agree and show substantial differences with Bamber's DEM around the distance of 15,000m (the maximum deviation equals ∼15m in b and ∼10m in b). This location corresponds to the trench T_1,
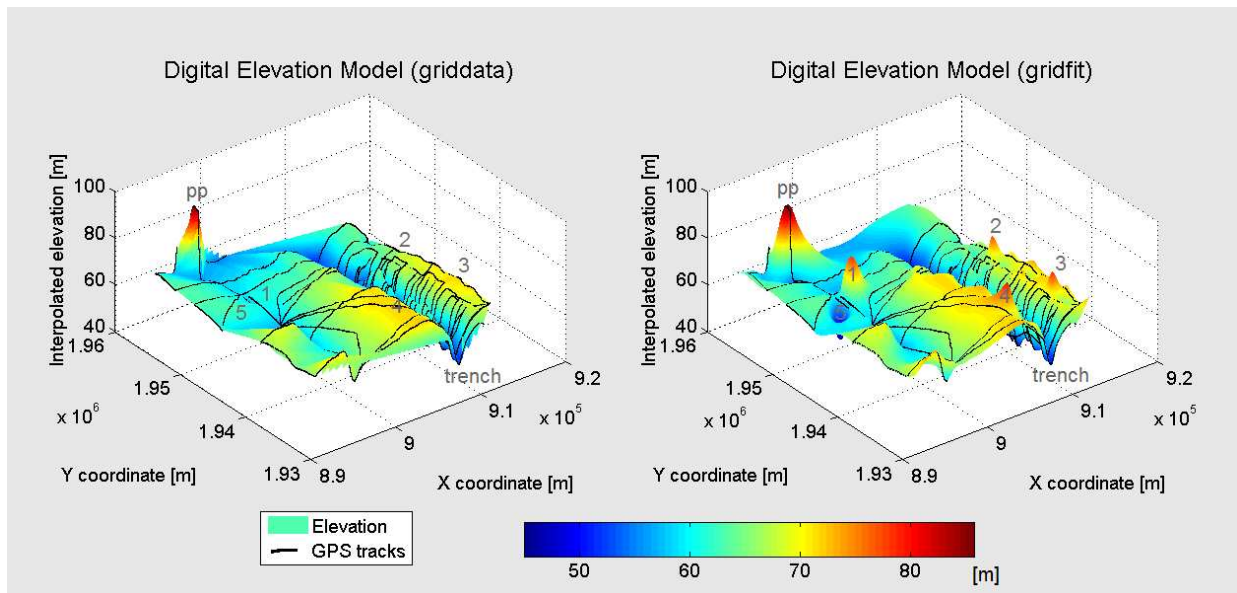
Figure 5.7: <u>3D-plots of the Digital Elevation Models generated and GPS tracks from which DEMs were interpolated.</u> The subplot on the left was generated with the matlab function *griddata*, while the subplot to the right comes from the *griddfit* function. We see that the subplot on the right is smoother but also contains computational artefacts (grey numbers), either as non-existent topographic high (1-4) or as depression (5). Other grey annotations denote remarkable topographic features of the map: the presence of a pinning point in the north (pp) and a "trench" with a north-south orientation in the east.

which means that such feature as trench, visible on intensity radar image are not sufficiently represented in global DEMs such as Bamber's. Moreover, we can see that in profile c, the trench T_1 is subdivided in two parts and another less deep trench clearly appear around 5,000m. This new trench is not as apparent in profile b. Although griddata and gridfit DEMs look very similar in profile b, this is not the case for profile c. In the latter, the gridfit curve moves away from the two other curves around 5,000m. Griddfit shows indeed a steep depression followed by a topographic high that are to relate with artefacts previously discussed. Finally the along-flow profile (a) does not show substantial variation between the three DEMs, if we except another artefactual depression of gridfit (around 17,500m) and very different behaviours of the computed DEMs and Bamber's at the level of the pinning point (25,000m and beyond). The pinning point is indeed not resolved in Bamber's DEM and the topographic elevation we see in Bamber's DEM corresponds to the edge of the ice shelf.

To sum up we can say that our DEMs prove that an ice shelf is not necessarily as flat as we could think. The local topographic variations are not precisely enough depicted in global DEMs such as Bamber's. As a consequence, error in the DEM could seriously impact on the final interferometric results. This will be discussed in the following chapter. We can
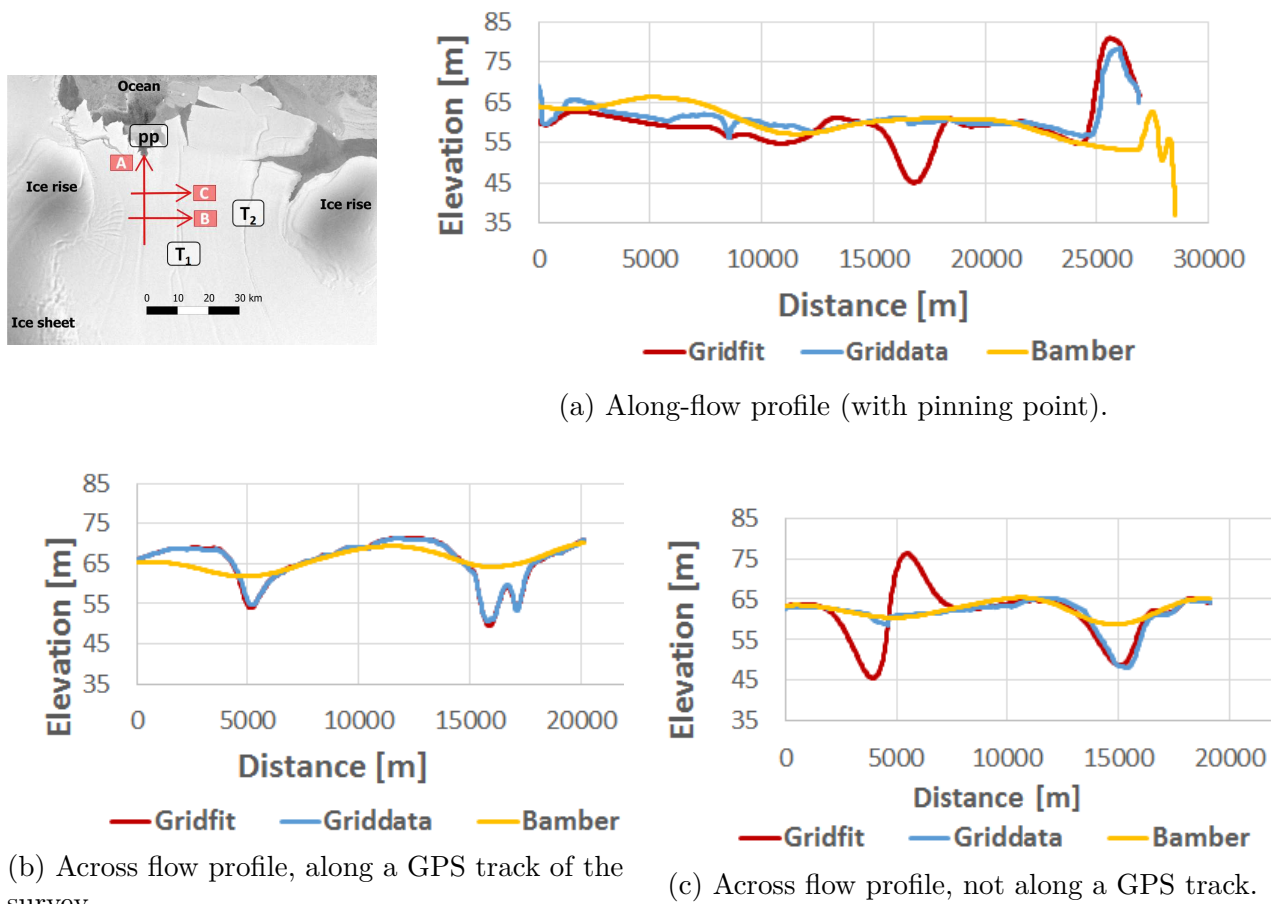
(a) Along-flow profile (with pinning point).

(b) Across flow profile, along a GPS track of the survey.

(c) Across flow profile, not along a GPS track.

Figure 5.8: Comparison between griddata, gridfit and Bamber's DEMs. The top left map locates the three different profiles. Profile a is along the ice flow and parallel to the trenches T_1 and T_2, while the two other profiles are across the flow and the trenches. As opposed to profiles b and c profile a was sampled along a track of the GPS survey. All the profiles are displayed on the same scale.

also conclude that it is better to base any further analysis on griddata DEM instead of gridfit. This is because of computational artefacts presented in figures 5.7 and 5.8.

5.2 Generalization to Dronning Maud Land

Interferograms of other parts of ice shelves in Dronning Maud Land were also analysed, similarly to what was performed with interferograms *t320_f5067_f5085* and *t430_f5697_f5715* of Roi Baudouin Ice shelf. This led to the identification and the mapping of numerous pinning points and island-type ice rises (like Derwael ice rise, on the east side of RBI). The map of pinning point and ice rises is presented on figure 5.9.

Unfortunately data were not available to combine other ascending and descending passes and getting other horizontal flowfields.
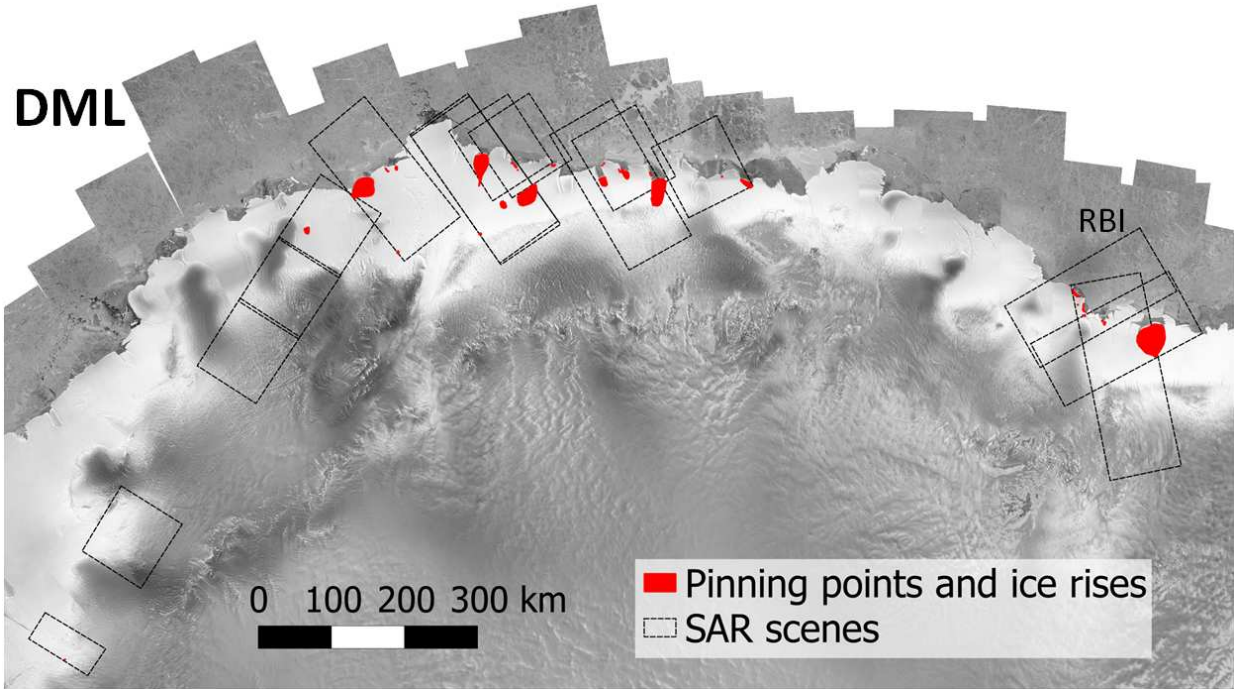
Figure 5.9: Map of pinning points and island-type ice rises, identified from interferograms. The extent of all the interferograms is presented in dashed line. DML = Dronning Maud Land and RBI=Roi Baudouin Ice shelf.

Chapter 6

Discussion

Some of the goals presented in the introduction have been completed. However, most of them constitute the framework of the discussion. The chapter is introduced by a comparison between our local flowfield and two existent flowfields (Smith's and Rignot's), which used data acquired at different times and with different sensors. This comparison can be seen as a sort of validation of the results and also as a quick investigation on the temporal variability of the ice shelf. The next section focuses on the dynamics of the Roi Baudouin Ice shelf, and more particularly on the role played by its pinning point. The discussion is even extended to two neighbouring ice shelves showing different flow regimes, with the purpose of explaining the observerd diferences in flow. The third part of the chapter is devoted to a discussion of the trenches previously pointed out and on their impacts on both the result accuracy and ice shelf dynamics. Aferward, the scale of the discussion is extended to the whole region of Dronning Maud Land and the temporal variability of the pinning point is discussed. Finally the last part of the chapter concerns limitations of InSAR and the error sources of our results.

6.1 Comparison of velocity-related results with Rignot's and Smith's

Rignot et al. (2011c) and Smith (2012, personal communication) also mapped ice motion in Antarctica, but at a wider scale and with a coarser gridding. They both used different sensors and data acquired at different times.

Rignot et al. (2011c) mapped the ice velocity for the whole Antarctic continent, with a 900m gridding. To do so, they combined information from different SAR sensors[1]. Even if the time span of the data acquisition ranges between 1996 and 2011, for Dronning Maud Land, most of the data was collected between 2007 and 2009 by the sensors ASAR on Envisat and PALSAR on ALOS satellites. InSAR was used to process the data, similarly to what we did in this thesis, for further information please refer to Rignot et al.'s (2011b) paper.

On the other hand, (Smith, 2012, personal communication) applied InSAR technique on Radarsat data and produced a surface velocity map with a 500m gridding. SAR images were acquired during the austral spring of 2000. The technique applied to infer velocities is a combination of phase information and speckle tracking offset as detailed by Joughin (2002). The results cover the vicinity of the Roi Baudouin ice shelf, as well as the West Ragnhild Glacier, its tributary ice stream.

In what follows, the three flowfields are referred as Rignot, Smith and Local. The flowfields are first compared to each other, they are then compared to the GPS-measurements.

6.1.1   Flowfields

The general aspect of the three flowfields seem to be coherent; however, a simple visual analysis of the three maps is not sufficient. That is why we mapped the differences between our flowfield and the two others (see figure 6.1). Two elements should be noticed: first, the colour pattern **does not seem random**, and secondly, **negative** (blue) and **positive** (red) colour classes are significantly **represented** in any case.

Related to the first observation, we can distinguish in each map a special pattern associated with the two trenches and upstream of the pinning point. The trenches are nevertheless harder to distinguish in the Rignot-Smith difference map, which is probably due to coarser spatial resolution of these two flowfields compared to the local one. In the two other difference maps, the trench pattern should probably be induced by higher errors in the local flowfield whose finer resolution makes it more sensitive to the trench. Furthermore, the particularly large differences in velocity in a narrow-band upstream of the pinning point are suspicious. The special pattern upstream of the pinning point probably reflects a more

---

[1]This includes ASAR sensor from the satellite Envisat, PALSAR onboard ALOS and SAR sensors of Radarsat 1-2 and ERS 1/2 satellites.

complicated flow-regime in this area. Both, the trenches and the pinning require a more focused attention. That is why entire sections (6.2 and 6.3) are dedicated to these specific issues.

The representation of positive as well as negative classes in each map means that if the differences between the maps reflect temporal variability of the ice shelf (and not only variations from the data processing), this variability of the flow is not indisputably faster or slower, but displays instead more complicated variations, especially upstream of the pinning point. More generally, compared to Rignot and Smith, the local flowfield shows faster velocities at the front of the ice shelf and slower at the back.

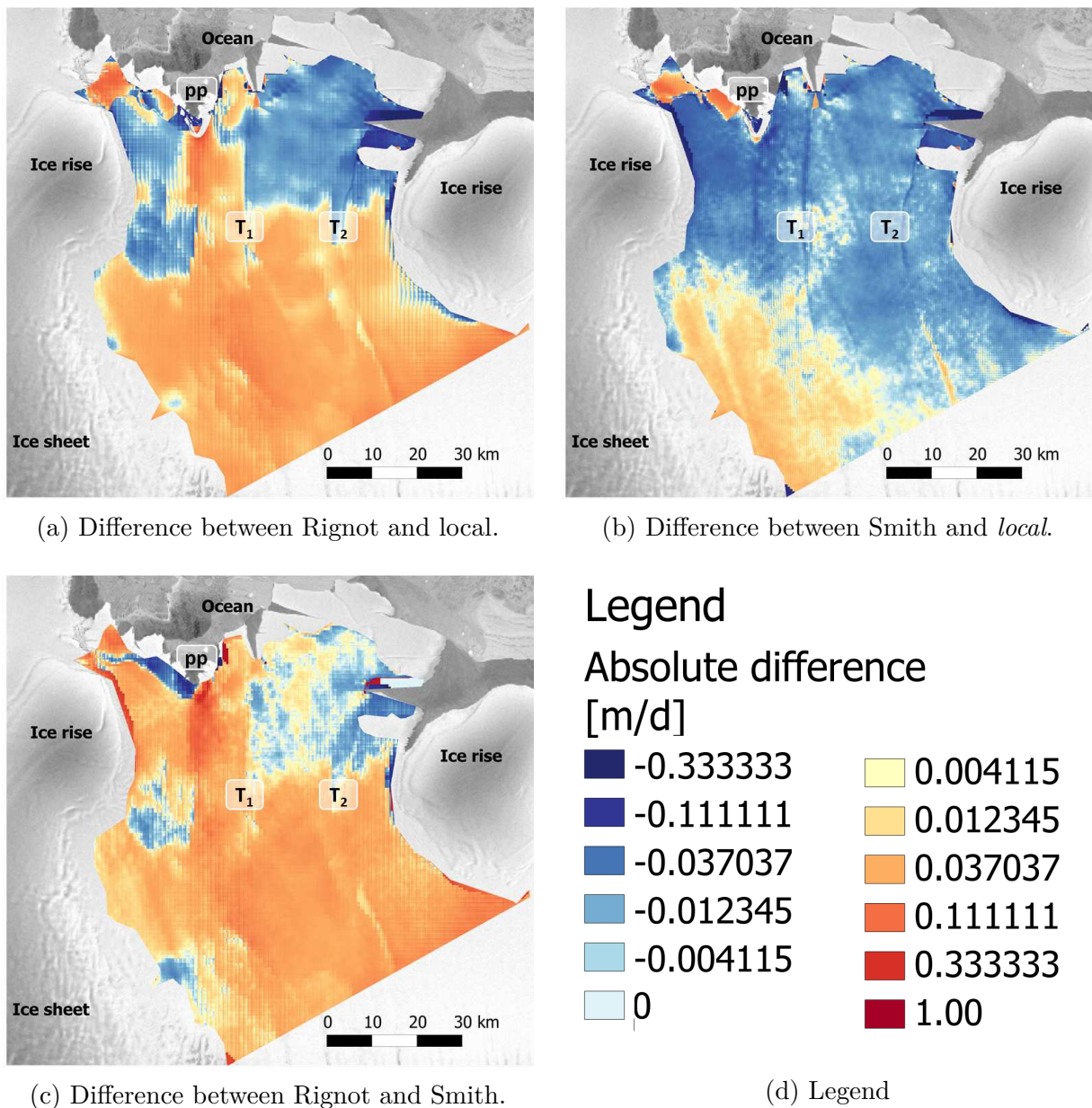(a) Difference between Rignot and local.

(b) Difference between Smith and *local.*

(c) Difference between Rignot and Smith.

(d) Legend

Figure 6.1: <u>Difference maps of the flowfields.</u> Please note that the colour-scale is logarithmic and symmetrical to zero.

Figure 6.3: Comparison between the three flowfields and the GPS measurements.

Points	$V_{GPS} - V_{LOCAL}$ [m/d]	$V_{GPS} - V_{RIGNOT}$ [m/d]	$V_{GPS} - V_{SMITH}$ [m/d]
L4M5	0.003	0.003	0.014
L3M4	0.002	-0.011	0.019
L3M2	0.018	-0.060	0.063

Figure 6.2: Deviation of the three flowfields (local, Rignot and Smith) from the GCPs.

6.1.2 Comparison with GCPs

From figures 6.3 and 6.2, we see that the local flowfield fits the most to our GCPs. The two other flowfields show nevertheless that the maximal deviation is in the order of centimetres, with a greater deviation for Smith, which is surprising as Smith's spatial resolution is finer than Rignot's. Figure 6.2 also shows that the greatest absolute deviation to the GCPs is for the slowest point (L3M2). This evidence supports the hypothesis of a more complex flow upstream of the pinning point (as opposed to a less good quality of the fitting away from the calibration point, see section 5.1.3).

6.2 The pinning point

Up to now, we have emphasized several elements suggesting that despite its modest size, the pinning point of the RBI could play an important role in the ice shelf dynamics:

- There is an east-west asymmetry of the velocities, with slower speeds on the side of the pinning point (east).

- A break in the slope of the velocity profile seems to be associated with the location of the pinning point.

- A lot of shearing is observed upstream of the pinning point and in its vicinity, which suggests that the pinning point causes this shearing.

- More differences between the three flowfields are observed upstream of the pinning point.
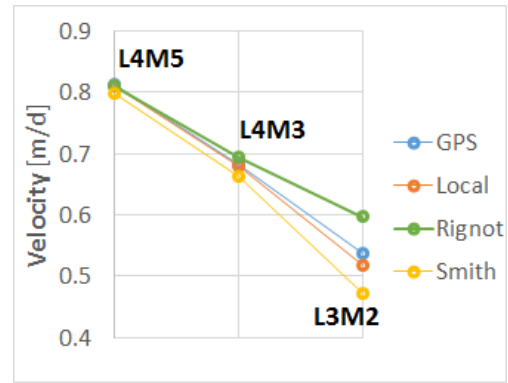
- The largest deviation from the GPS measurements are found for the point upstream of the pinning points.

- On figure 4.2, the GPS point upstream of the pinning point seems to show the less stable velocity.

The first three of these points proves that the pinning point influences the dynamics of the ice shelf, while the last three points suggest a more complicated and variable flow regime upstream of the pinning point. The first deduction is detailed below whereas for the second one a further investigation would be needed.

Velocity and shearing maps indicate together that Derwael ice rise blocks and redirects the ice flow, which is not very surprising given the area occupied by this ice rise (roughly a 1200 km^2). What is more astounding is the fact that even a small pinning point- whose area covers no more than 8.5 km^2- seems to play, in the ice shelf dynamics, an almost as important role as the ice rise. Derwael ice rise and the pinning point constraint together the flow of the ice shelf and define a gateway for the ice, while comparatively, the role played by *FranKenny* ice rise seems to be minor.

A)   Comparison with the neighbouring ice shelves

To put our results in perspective, we will now compare velocities of the Roi Baudouin Ice shelf with those of two neighbouring ice shelves, denoted as *west* and *centre* (figure 6.4). The two additional ice shelves have been chosen because they show similar coastal geometry as RBI: all the three shelves are indeed confined by two lateral ice rises. It should nevertheless be noted that RBI is the only one presenting an *island*-ice rise on its eastern part, the two other shelves are only constrained by *peninsula*-ice rises. We clearly see on figures 6.4b and 6.4a that the near-front velocities of RBI and centre ice shelves are comparable and significantly lower than for west ice shelf. On the contrary, velocities upstream of the grounding line show a very different pattern: ice flowing into west and centre ice shelves shows similar speed and is slower than ice from West Raghnild Glacier. **How can we explain such differences in velocities along the ice-flow?**

We deduce from figure 6.4 that differences of speed are attenuated at the grounding line (GL) but exist, as RBI is still faster than the two other ice shelves. This is why the relative slowdown of RBI and the relative speedup of West shelf must occur within ice shelves. Across-flow profiles A and B (figure 6.4) verify this assumption. Compared to profile C,

west shelf shows an important acceleration, RBI coarsely levels-off and the speed of centre shelf slightly increases in profile B and A.

We explain such flow differences by the presence of the pinning points and more precisely their presence at key emplacement to constraint the flow.

In west shelf, there is only one small pinning point, in the east, near the grounding line that seems too marginal to substantially retain the ice-flow. Besides the strain-rates map (figure 6.5) suggests that the pinning point acts like an extension of the lateral ice rise (in the east), this map also suggests that the major restraining force on the ice shelf is the lateral drag with the embayment.

On the contrary, the pinning point of the RBI, being an important source of shearing, seems to be a decisive factor in the velocity and the displacement of the ice. We have deduced, above, that its presence delimited a gateway for the ice. It should explain major differences in dynamics relative to west shelf.

The centre shelf, for its part, represents a kind of intermediate situation: it is not fed by a major ice stream and it does not show as substantial acceleration as west shelf. We suppose this is to relate to a less important role of the pinning points of centre shelf. They are indeed located in the east of the shelf, more or less aligned to the FranKenny ice rise. Unlike the pinning point of RBI, the pinning points of centre shelf do not induce visible break in slope of the velocity profile. Rather, on the strain-rates map, they appear as if they belonged to the side of the ice shelf, slightly redirecting the flow. Similarly to west shelf, lateral drag seems to be also dominant for this shelf.
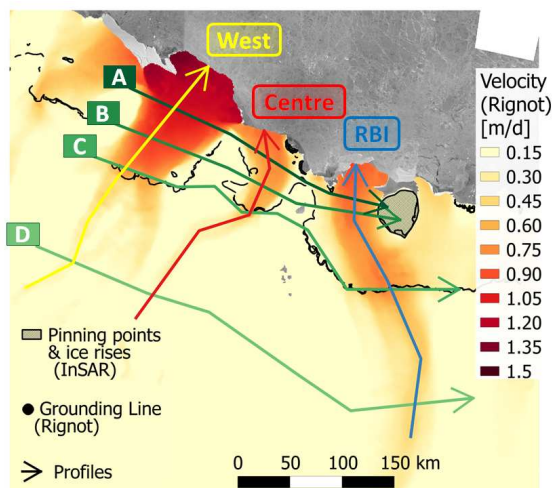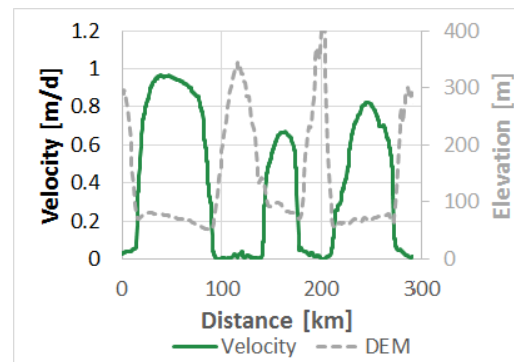
(a) Situation map of the three ice shelves and profiles.
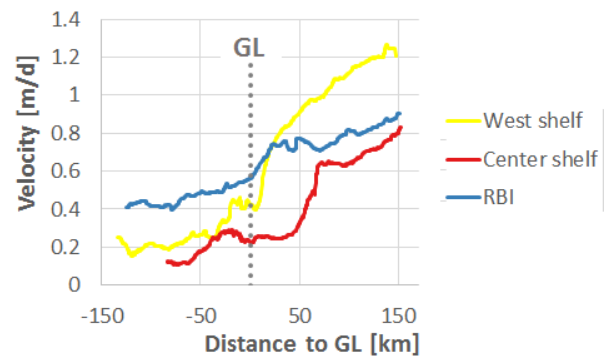
(b) Along flow profiles.
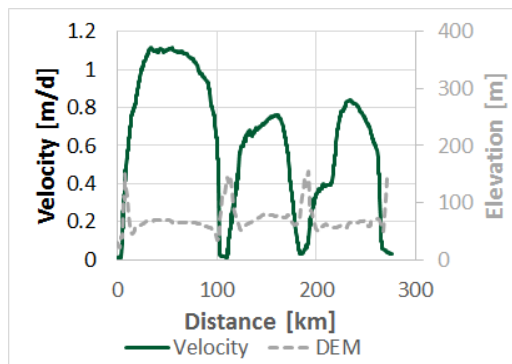
(c) Profile **A**, near the front of the ice shelves (between 20 and 40 km upstream of the front).

(d) Profile **B**, in the middle of the ice shelf.
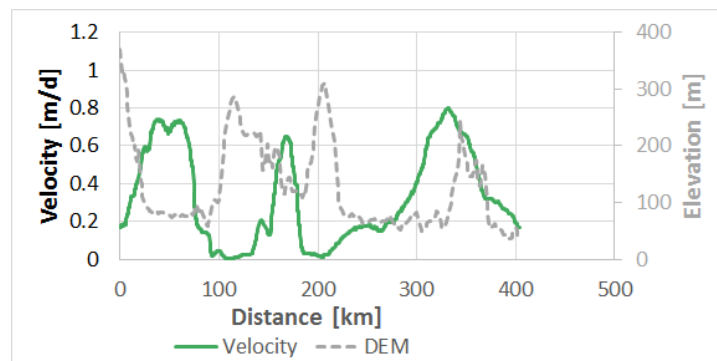
(e) Profile **C**, at the grounding zone.
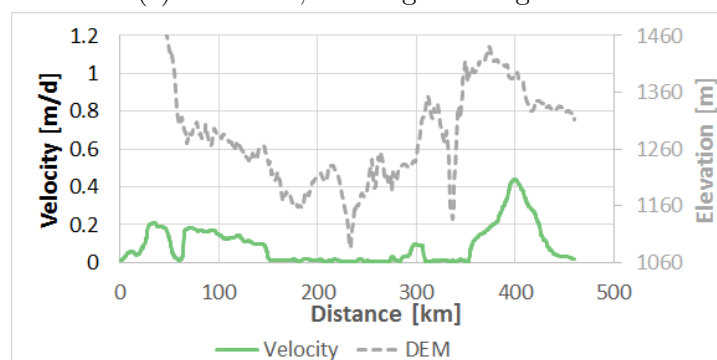
(f) Profile **D**, 100 km upstream of the grounding line.

Figure 6.4: <u>Comparison profiles of the RBI and two neighbouring ice shelves</u>. This figure presents, one along flow profile of the three ice shelves and their main feeding ice stream (b) and the four profiles (A,B,C,D) across the flow of the ice shelves and their tributary glaciers. (The dotted grey line correspond to Bamber's DEM.

Figure 6.5: Strain rates of the three ice shelves (derived from Smith). The map compares two ice shelves dominated by lateral drag (west and centre shelves) and one dominated by friction with a pinning point in its front (RBI). Note that Smith does not cover the upper-left corner, as a result, we completed the map with Rignot's strain rates. Moreover, the colour scale is exactly the same as for the strain rates map of the RBI
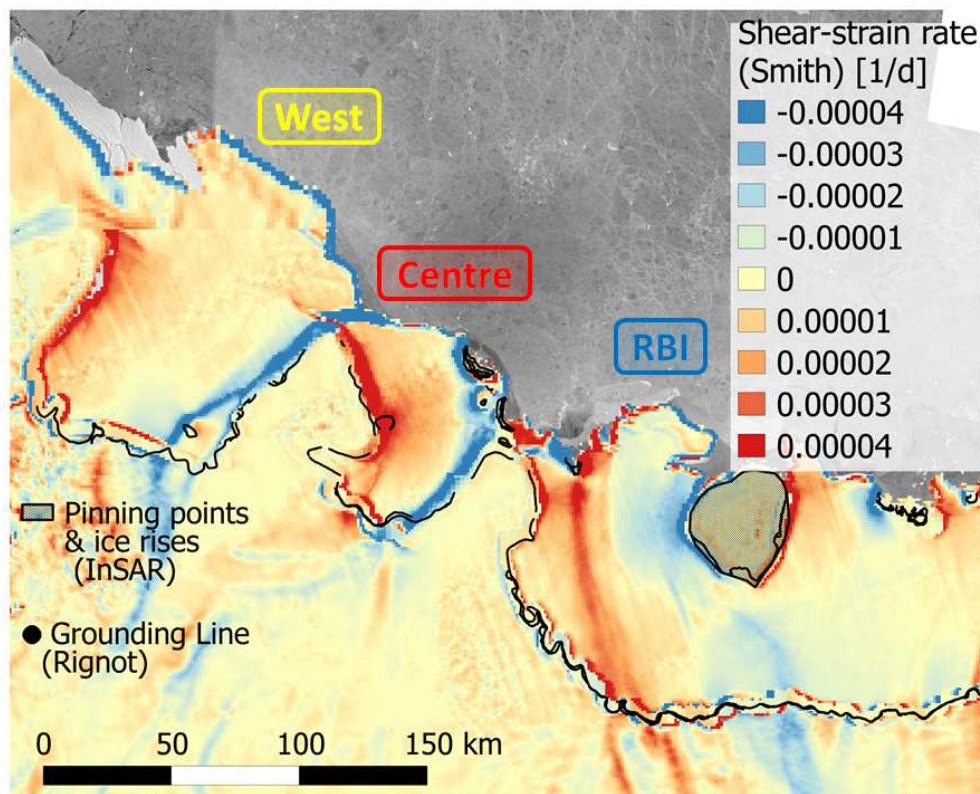
6.3 The trenches

We have seen, in chapter 5, that Bamber's DEM does not resolve local steep variations of the topography such as the two trenches previously underlined. As a consequence the use of Bamber's DEM introduces local flaws in the flowfield and therefore in the subsequent strain-rates. Velocities are indeed overestimated in the trenches (cf. figure 5.4a). As these trenches show steep slopes, it manifests itself in high spatial velocity gradients (shearing), successively positive and negative. That is why the trenches appear so clearly on the strain-rates map. The red-blue alternation around the trenches in the strain-rate map indicates therefore computation artefact due to topographic effect. It is indeed unthinkable that we observe such high velocity gradients evolving so rapidly in ice flow. However, in numerous parts of the trench T_1, strong shearing is displayed without sign change (i.e. colour variation). It is important to find out whether this apparent shearing is real or if it is introduced by computation. Real shearing would indeed mean that this trench represents a weak-spot on the ice shelf, which would have serious implications for the ice shelf dynamics.

To verify the weak-spot hypothesis, we calculated the shear-strain rates between the GPS stations L4M3 and L4M5, the first one being on the west side of the trench T_1 while the other is on the eastern side. The results obtained, $\dot{\varepsilon}_{xy} \ (GPS) = 6.14 \times 10^{-4} \ d^{-1}$ and $\dot{\varepsilon}_{xy} \ (InSAR) = 8.24 \times 10^{-4} \ d^{-1}$ are not fully coherent and would deserve a further investigation, InSAR results seem to suggest more shearing than the reality.

6.4 Temporal variability of pinning points

The pinning points and ice rises map, presented on figure 5.9, was compared Rignot et al.'s (2011d) work. As explained in their paper (Rignot et al., 2011a), the searchers mapped the grounding line of the entire Antarctic continent, from differential satellite radar interferometry, using several sensors. They differentiated interferograms to remove the horizontal signal of the velocity. As a result, the fringe pattern in their differential interferograms was related to vertical motion, and therefore to tides. We have indeed seen in section 3 that the interferometric phase was very sensitive to vertical motion. Dense fringe pattern (i.e. high displacement gradients) are found at transition zones between grounded and ungrounded parts, as shown in figure 5.2. Ice sheet, ice rises (and pinning points), which are grounded, are indeed not affected by tidal uplift, unlike ungrounded ice shelves.

Even if most of pinning points and ice rises we identified match with Rignot's, we found a few disagreements. Rignot identified pinning points we did not see and vice versa. Some of the "missing" pinning points may be only ephemerally grounded. Ephemeral pinning points are topographic highs of the seafloor that ground the ice shelves at low tide only. They are indeed not high enough to ground the ice shelf when tide is high. Schmeltz et al. (2001) proposed the technique of counting fringes on differential interferograms at the grounding line and around the pinning points, to identify ephemeral grounding. A lower number of fringe around a pinning point than at the grounding line, means a lower vertical velocity gradient relative to the grounding line. This implies that one part of the ice above the pinning point has been uplifted by tides. Their technique, however, requires the combination of two interferograms with the same time interval and acquired from the same orbital geometry, which was, unfortunately, unavailable for us. When it was possible, we still tried to count fringes around pinning point and at the grounding line. Counting fringes on a non-differential interferogram implies that vertical motion was not isolated and requires the assumption of negligible contribution of the horizontal motion to the fringes pattern we were counting. By this technique we could identify potential ephemeral pinning points (such as the one of track 388 shown on figure 6.6) with less fringes than the surrounding grounded area (ice sheet or ice rises). To be certain that the point is really ephemeral, once again further investigation is needed. According, to Schmeltz et al. (2001) ephemerity of pinning point is an indication for ice shelves thinning. Investigation of the influence the sea level exerts on the pinning points and their ability to restraint ice-flow is also important for projecting the behaviour of the ice shelves in the future.
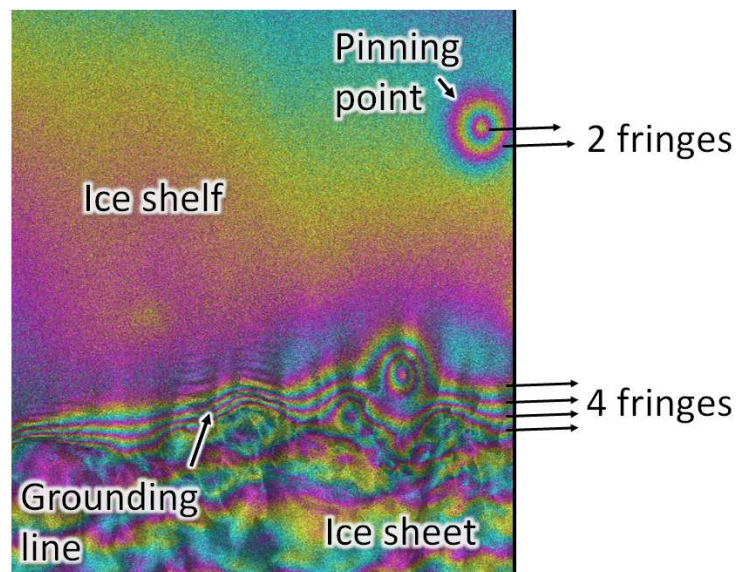

Figure 6.6: Potential ephemeral pinning point.

6.5   Limits and sources of errors

It is now essential to mention the limitations of the InSAR technique. In this section, we principally deal with two major limitations: the availability of the data and the uncertainties/errors related to the processing.

6.5.1   Data availability

Ice shelves are fast moving and flat parts of an ice sheet, they are thus more likely to show stronger temporal decorrelation. This is a fundamental constraint that limits the potential of suitable (coherent) data for interferometry. Finding coherent SAR pairs is not always an easy task. Moreover, once we have our data ready to be processed, another problem of data availability arises: the lack of GCPs. We have seen that control points were essential to performing InSAR. Unluckily, finding such points on ice shelves can be tricky: Antarctica is a remote continent difficult to reach, which limits in-situ measurements; and secondly, particular features of the ice shelves where zero ice flow can be assumed are not always available on ice shelves and can be biased by a differential tidal uplift, compared to the ice shelf.

6.5.2   Processing uncertainties

In here, we focus more particularly on errors generated by data processing. This includes: imprecise baseline model, SAR processing and inaccuracy of the DEM. To assess uncertainties related to the processing, ESA provided us with another version of the scene/track *t320*. The SAR processing of this new version was already led by the ESA[2] and, as a result each frame of t320 (f5067 and f5085) were treated separately. Once we acquired the ESA-pre-processed frames, we generated two new horizontal flowfields using exactly the same processing parameters as for the principal flowfield previously presented. The comparison between the different flowfields (figure 6.7) allows us to deduce information about processing uncertainties. Subfigures 6.7a, 6.7b and 6.7c inform us about both uncertainties related to baseline estimation and different raw data processing. However, subfigure 6.7c differs from the two other because the same SAR processor was used for both frames. As a results uncertainties not related to baseline estimation originate from individual estimations of

---

[2]For all other scenes, the SAR processing was performed at the Laboratoire de Glaciologie with GAMMA MSP module.

parameters during the SAR processing. Each individual frame was indeed similarly raw-processed by the ESA, but the overlap area is unfortunately much smaller. Before starting with a discussion about baseline uncertainties and effects of raw data processing, it should be noted that uncertainties related to processing are minor, comparing to the difference map previously presented.

(a) Difference between 2frames and f5085.

(b) Difference between 2frames and f5067.

(c) Difference f5085 and f5067.

(d) Legend.
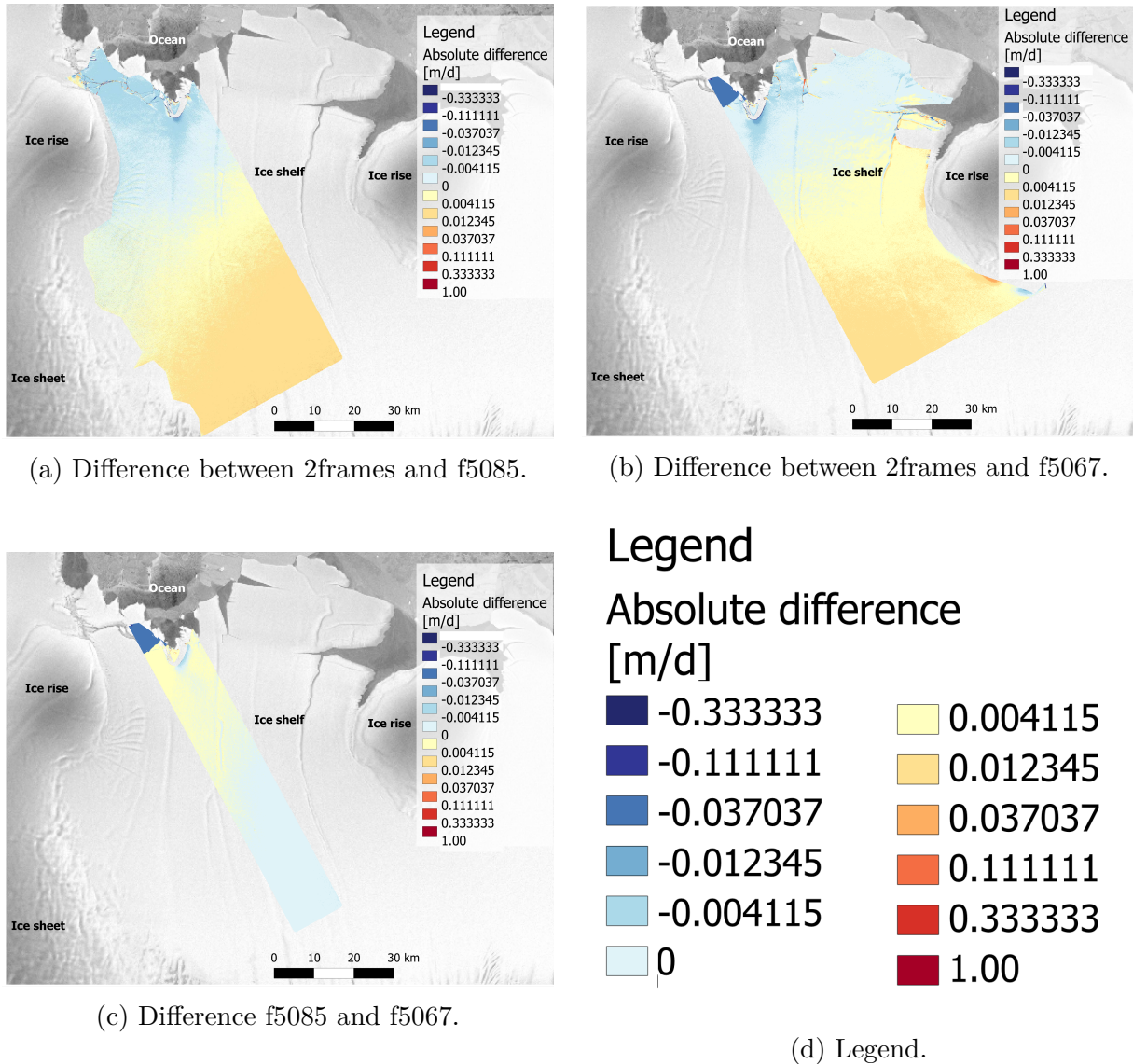
Figure 6.7: Difference maps of the flowfields. Please note that the colour-scale is exactly the same as in figure 6.1, i.e. this is a logarithmic scale, symmetrical to zero.

A) Baseline model

One source of processing uncertainties is related to imprecise baseline model. It is actually technically difficult to determine precisely the baseline between the two sensor positions during image acquisition. Estimates of baseline are indeed only accurate with several decimetres (Massom and Lubin, 2006) while very precise estimations are required at several

processing steps (cf. sections 3.1 and 3.2). Although the motion contribution ($\Delta\phi_{motion}$) to the interferometric phase is, in principle, not influenced by the spatial baseline (see equation (2.13)), errors in baseline estimation still lead to errors in the final flowfield. Such errors are caused by imperfect cancellation of the topographic contribution ($\Delta\phi_{topo-sim-unw}$) (Joughin et al., 1996). We have indeed seen in section 3.2, that baseline was needed to simulate the topographic phase from a DEM. To overcome this issue it is generally possible to refine baseline estimation with independent derived control points with known position, elevation and velocity (Massom and Lubin, 2006). We were nevertheless not able to implement this operation because it requires at least four points (Joughin et al., 1996), which were not available for the Roi Baudouin Ice shelf. According to Massom and Lubin (2006), if the baseline estimation is not refined, baseline errors result in a *near-linear phase ramp* in the interferogram. As a matter of fact, their assertion is supported by figure 6.7. Each of the three maps displays a colour gradient along the south-east to north-west direction, which corresponds to the near-range to far-range direction of track 320 (see figure 5.2). Figure 6.8 showing the profiles of difference maps in the range direction of the radar, also confirms the near-linear ramp. The linear trend of each profile has been added and we can see that the trend fits the curves very well.

(a) Overview map.

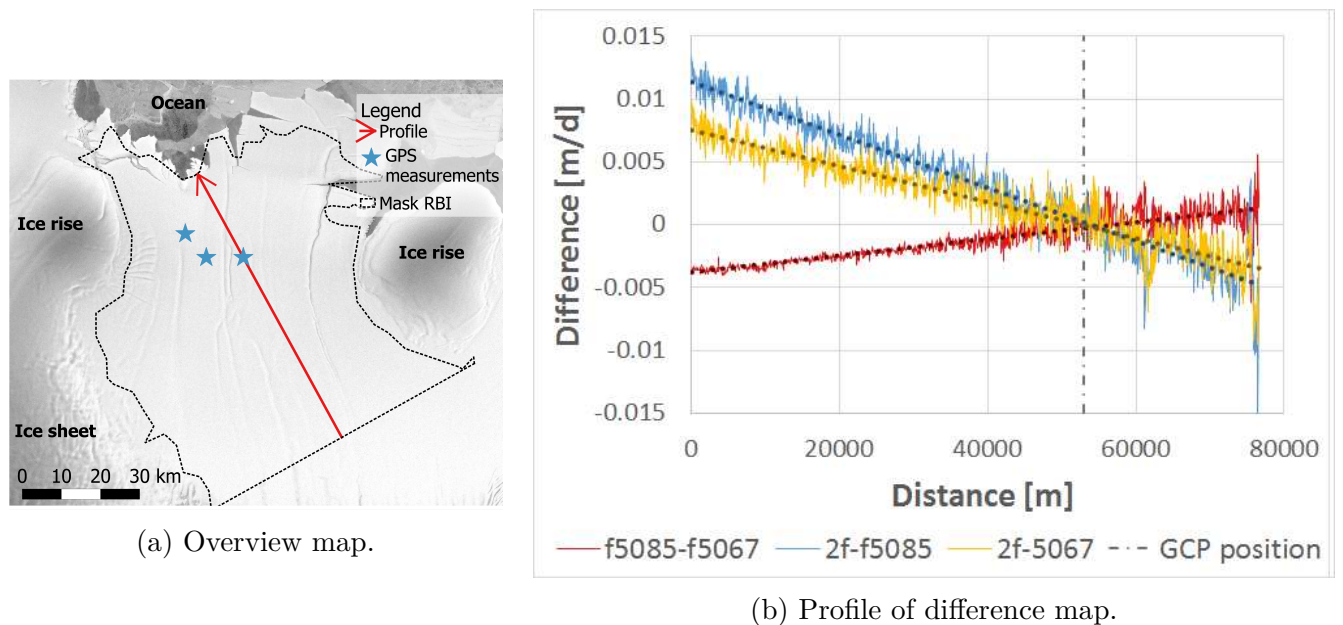(b) Profile of difference map.

Figure 6.8: Profile of the difference maps related to processing uncertainties.

B)   SAR processing

Another source of error potentially explaining the slight difference in magnitude between maps 6.7a and 6.7b on the one hand and map 6.7c on the other hand originates from the

raw data processing. Drews et al. (2009) carried out a cross-comparison between InSAR products (DEMs, in their case) based on the same raw data but different SLC products obtained by various SAR processors. This is how they demonstrated that SAR processing could lead to significant uncertainties, even in case of frames SAR-processed with the same processor but either individually or together. They also concluded that it is "*difficult to evaluate and adjust possible inaccuracies originating in the raw data to SLC processing, which may superimpose other geophysical effects.*"(Drews et al., 2009, p.8).

We used the overlap between frames f5085 and f5067 of the track t320, to assess in a quantitative way, the contribution of SAR-processing uncertainties to the difference map observed (figure 6.7c). To do so, we computed an *auto-interferogram*, i.e. an interferogram generated from an identical scene with different SAR processing history. In other word, the interferometric phase of the autointerferogram, should be null because it is, in theory, the same phase that is subtracted, any non-zero interferometric is provoked by SAR processing history. Figure 6.9 shows the profile of an autointerferogram generated in the overlap area of frames f5067 and f5085. Despite the noise, we see in this figure that ESA differentiated SAR-processing of frames f5067 and f5085 introduced a small offset in the autointerferogram (the autointerferometric phase mean equals -0.021 rad), which is not sufficient to explain the differences between the flowfields f5085 and f5067. We can consequently attribute the linear trend we observe in figure 6.8 to baseline estimation errors.

C) DEM-induced errors

Inaccuracy in DEMs necessarily leads to errors in the final flowfield. Such errors are introduced during simulation of the topographic contribution ($\Delta\phi_{topo}$). In section 3.2, we have seen that a DEM was needed to simulate such topographic contribution. The simulated topographic phase is then removed from the interferogram by subtraction. We found two different kinds of *DEM-induced errors*: errors related to inaccurate altitude estimation and errors in ice shelf extent. Concerning the first one, if the DEM misjudges the real altitude, the simulated topographic phase will not totally fit the real topographic phase, leading to residues in the differential interferogram (motion-only). These residues will be transformed into velocities leading to errors. This is what was observed at the level of the trenches. We have seen that Bamber's DEM did not resolve these trenches, or at least not sufficiently, inducing irregularities/slope breaks in the velocity and strain rates profiles. Ideally, to quantify this uncertainty, an additional flowfield should be generated using the
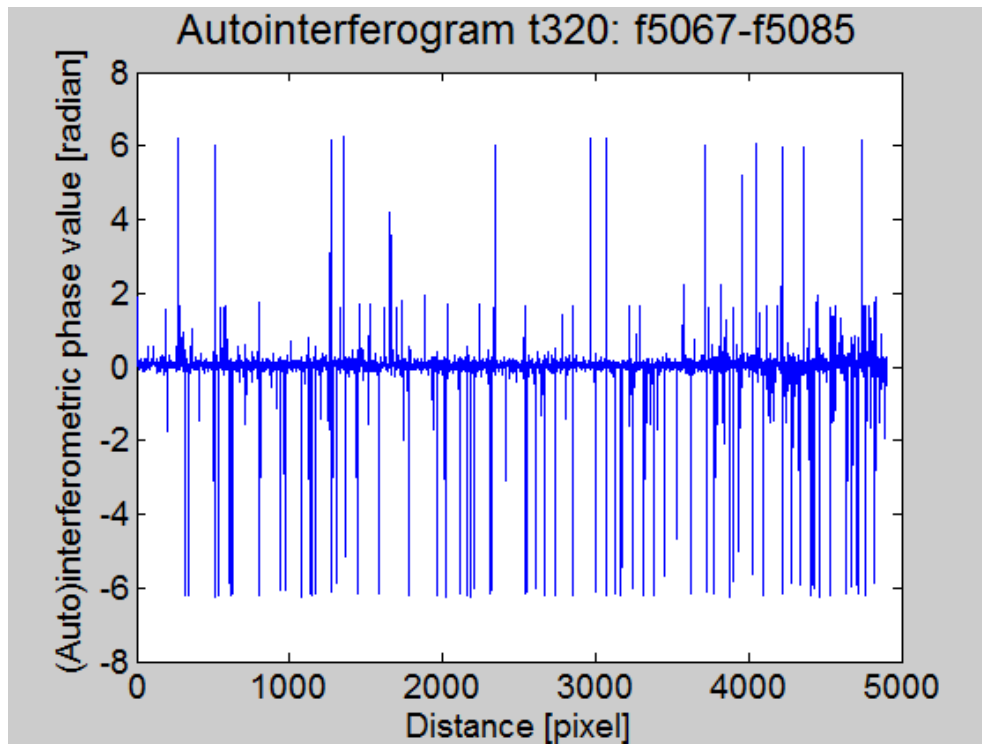
Figure 6.9: <u>Profile in the autointerferogram of frames f5067 and f5085.</u> In theory the autointerferometric phase value should be 0. Deviations originates from differentiated SAR processing of each frame.

local interpolated DEM (cf. section 5.1) to remove the topography. We were however not provided with sufficient time to fully assess the magnitude of this error source. It should finally be noted that errors induced by a DEM depend on the altitude of ambiguity and thus on the size of the spatial baseline. This is why interferograms with smaller baselines are less sensitive to topography.

The second kind of errors is more specific of ice shelves. If the DEM and the radar images do not show the same extension for the ice shelf, it will induce errors and loss of information. This was our case at the front of the ice shelf. There is a ~ 8 km long gap between Bamber's DEM prediction of ice shelf-ocean boundary and the limit we detected in intensity image. The boundary of Bamber's DEM introduced a major discontinuity in the differential interferogram (i.e. where the topographic contribution has been removed) As a results parts beyond Bamber's boundary were not reliable in the final flowfield and had to be masked. We are consequently not able to estimate terminal velocities of the RBI.

Chapter 7

Conclusion and perspectives

In this thesis, SAR interferometry was successfully applied to 18 SLC image pairs from the ERS 1/2 tandem mission (1995-1996), thus generating 18 interferograms, covering ice shelf boundaries with major outlet glaciers termini of Dronning Maud Land. All the interferograms were examined to identify the location of pinning points and island-ice rises. All these pinning points were then compared to Rignot's map of grounding line and grounded features and potential ephemeral pinning points have been underlined. A more in-depth investigation of these particular points is needed to determine if they really are ephemeral and to understand the implication of ephemerality, using for instance Radarsat data. However, ephemerality of the pinning point could be an indication for ice shelves thinning.

In addition, two of the interferograms were combined to produce a high resolution map (50m) showing the horizontal flowfield of the Roi Baudouin Ice shelf. The map shows an average speed of 0.54 m/d. From this map, the shear-strain rates were calculated and used to highlight the role of the pinning point at the front of the Roi Baudouin Ice shelf (RBI) in term of ice dynamics. It was found that the pinning point is an important source of shearing, diverting the ice flow. The pinning point defines, together with the imposing Derwael ice rise, a gateway for the ice shelf. By comparing, our results with flowfields of Smith and Rignot, we showed that the pinning point was the main suspect, explaining the large difference in flow regimes of Roi Baudouin and two neighbouring ice shelves (named west and centre shelves in this study).

In this study we also investigated the accuracy of our flowfield and of the limits of SAR interferometry for mapping velocities. An absolute deviation of 0.003 m/d (which represents a relative deviation of 0.37%) was found at the calibrating point.

We showed that the major sources of processing uncertainties are due to a lack of precision in the baseline estimation, SAR processing of raw data into SLC form, and errors in the DEM used to remove the topographic effect on the phase. Errors in the baseline estimation introduce a linear phase ramp. However, it is possible to refine the estimation of the spatial baseline if at least four Ground Control Points are available, which was not the case in our study. SAR processing uncertainties are hard to evaluate as they are introduced upstream of InSAR processing; nevertheless, we produced one autointerferogram and showed that SAR uncertainties were negligible compared to baseline uncertainties. Finally Digital Elevation Models (DEMs), especially at Antarctic-wide scale, can also introduce significant errors. To illustrate this fact, errors induced by local trenches on the Roi Baudouin Ice shelf have been highlighted. To assess this uncertainty a local DEM resolving the topography of one trench was computed, unfortunately a lack of time prevented us to implement this local DEM in the processing chain.

The study was limited by a lack of available data, starting with a limited amount of satellite SAR data and a recurrent difficulty to find coherent interferometric pairs especially for fast flowing features, such as ice shelves . For this reason, data from the ERS tandem mission are still one of the most suitable in our case, despite their 1995-1996 acquisition. The disposal of GCPs is another limiting factor, particularly on the ice shelves that are affected by tides, while it is essential for the processing.

On the whole InSAR is an accurate method for providing flowfields with a dense spatial coverage. It is however limited by the availability of interferometric pairs and very dependent on external data (GCPs and DEM). These InSAR limitations could be partly overcome by combining InSAR with speckle tracking offsets (Joughin, 2002).

Bibliography

Alley, R., Clark, P., Huybrechts, P. and Joughin, I. (2005). Ice-sheet and sea-level changes, *science* **310**(5747): 456–460.

Ballou, G. (2005). *Handbook for sound engineers*, Focal Press, Elsevier/Focal.

Bamber, J., Gomez-Dans, J. and Griggs, J. (2009a). A new 1 km digital elevation model of the antarctic derived from combined satellite radar and laser data–part 1: Data and methods, *The Cryosphere* **3**(1): 101–111.

Bamber, J. L., Gomez-Dans, J. L. and Griggs, J. A. . (2009b). Antarctic 1 km digital elevation model (DEM) from combined ERS-1 radar and ICESat laser satellite altimetry., Boulder, Colorado USA: National Snow and Ice Data Center. Digital media. Digital media.

Bamber, J., Layberry, R. and Gogineni, S. (2001). A new ice thickness and bed data set for the greenland ice sheet 1. measurement, data reduction, and errors, *Journal of Geophysical Research* **106**(D24): 33773–33.

Bamler, R. and Hartl, P. (1998). Synthetic aperture radar interferometry, *Inverse Problems* **14**(4): 1–54.

Barry, R. and Gan, T. (2011). *The Global Cryosphere: Past, Present and Future*, Cambridge University Press.

Benson, H. (1996). *University physics*, John Wiley.

Bürgmann, R., Rosen, P. and Fielding, E. (2000). Synthetic aperture radar interferometry to measure earth's surface topography and its deformation, *Annual Review of Earth and Planetary Sciences* **28**: 169–209.

Cazenave, A. (2006). How fast are the ice sheets melting?, *Science* **314**(5803): 1250–1252.

Chuvieco, E. and Huete, A. (2010). *Fundamentals of Satellite Remote Sensing*, Environmental Science and Engineering, Taylor & Francis Group.

Cloud, G. (2008). Basics of optics, *in* J. Sharpe, William N. (ed.), *Springer Handbook of Experimental Solid Mechanics*, Springer US, pp. 447–480.

Costantini, M. (1998). A novel phase unwrapping method based on network programming, *IEEE Transactions on Geoscience and Remote Sensing* **36**(3): 813–821.

Cumming, I. and Wong, F. (2005). *Digital Signal Processing of Synthetic Aperture Radar Data: Algorithms and Implementation*, The Artech House Remote Sensing Library, Artech House, Norwood.

Curlander, J. and McDonough, R. (1991). *Synthetic Aperture Radar: Systems and Signal Processing*, Wiley Series in Remote Sensing Series, John Wiley & Sons, New York.

D'Elia, S. and Jutz, S. (1997). SAR mission planning for ers-1 and ers-2., *ESA Bulletin* **90**.

Drews, R., Rack, W., Wesche, C. and Helm, V. (2009). A spatially adjusted elevation model in dronning maud land, antarctica, based on differential sar interferometry, *IEEE Transactions on Geoscience and Remote Sensing* **47**(8): 2501–2509.

Duchossois, G. and Martin, P. (1995). ERS-1 and ERS-2 tandem operations, *ESA Bulletin* **83**: 54–60.

Dupont, T. and Alley, R. (2005). Assessment of the importance of ice-shelf buttressing to ice-sheet flow, *Geophysical Research Letters* **32**(4).

Dupont, T. and Alley, R. (2006). Role of small ice shelves in sea-level rise, *Geophysical research letters* **33**(9): L09503.

Dutton, A. and Lambeck, K. (2012). Ice volume and sea level during the last interglacial, *science* **337**(6091): 216–219.

ESA (n.d.). Earth observation missions. ERS. Accessed 06/05/2013.
    URL: *https://earth.esa.int/web/guest/missions/esa-operational-eo-missions/ers*

Ferretti, A., Monti-Guarnieri, A., Prati, C. and Rocca, F. (2007). *InSAR Principles: Guidelines for SAR Interferometry Processing and Interpretation.*, ESA.

Furuya, M. (2011). SAR interferometry, *in* H. Gupta (ed.), *Encyclopedia of Solid Earth Geophysics*, Encyclopedia of Earth Sciences Series, Springer Netherlands, pp. 1041–1049.

Giancoli, D. (2000). *Physics for Scientists & Engineers With Modern Physics*, third edn, Prentice Hall.

Goldstein, R., Engelhardt, H., Kamb, B. and Frolich, R. (1993). Satellite radar interferometry for monitoring ice sheet motion: Application to an antarctic ice stream, *Science* **262**(5139): 1525–1530.

Goldstein, R. and Werner, C. (1998). Radar interferogram filtering for geophysical applications, *Geophysical Research Letters* **25**(21): 4035–4038.

Goldstein, R., Zebker, H. and Werner, C. (1988). Satellite radar interferometry: Two-dimensional phase unwrapping, *Radio Science* **23**(4): 713–720.

Graham, A. (2011). Ice sheet, *in* V. Singh, P. Singh and U. Haritashya (eds), *Encyclopedia of Snow, Ice and Glaciers*, Encyclopedia of Earth Sciences Series, Springer Netherlands, pp. 592–608.

Graham, L. (1974). Synthetic interferometer radar for topographic mapping, *Proceedings of the IEEE* **62**(6): 763–768.

Griggs, J. and Bamber, J. (2009). A new 1 km digital elevation model of antarctica derived from combined radar and laser data-part 2: Validation and error estimates, *The Cryosphere* **3**: 113–123.

Høgda, K., Storvold, R. and Lauknes, T. R. (2011). Sar imaging of glaciers, *Remote Sensing*

of Glaciers: Techniques for Topographic, Spatial and Thematic Mapping of Glaciers, Taylor & Francis, chapter 9, pp. 153–178.

Jenkins, A. (2011). Ice shelf, *in* V. Singh, P. Singh and U. Haritashya (eds), *Encyclopedia of Snow, Ice and Glaciers*, Encyclopedia of Earth Sciences Series, Springer Netherlands, pp. 613–616.

Jezek, K. (2002). RADARSAT-1 antarctic mapping project: change-detection and surface velocity campaign, *Annals of Glaciology* **34**(1): 263–268.

Jezek, K. and RAMP Product Team (2002). RAMP AMM-1 SAR image mosaic of antarctica, Fairbanks, AK: Alaska Satellite Facility, in association with the National Snow and Ice Data Center, Boulder, CO. Digital media. Version 2.

Joughin, I. (2002). Ice-sheet velocity mapping: a combined interferometric and speckle-tracking approach, *Annals of Glaciology* **34**(1): 195–201.

Joughin, I., Kwok, R. and Fahnestock, M. (1996). Estimation of ice-sheet motion using satellite radar interferometry: method and error analysis with application to humboldt glacier, greenland, *Journal of Glaciology* **42**(142): 564–575.

Joughin, I., Kwok, R. and Fahnestock, M. (1998). Interferometric estimation of three-dimensional ice-flow using ascending and descending passes, *IEEE Transactions on Geoscience and Remote Sensing* **36**(1): 25–37.

Kopp, R., Simons, F., Mitrovica, J., Maloof, A. and Oppenheimer, M. (2009). Probabilistic assessment of sea level during the last interglacial stage, *Nature* **462**(7275): 863–867.

Lemke, P., Ren, J., Alley, R., Carrasco, J., Flato, G., Fujii, Y., Kaser, G., Mote, P., Thomas, R. and Zhang, T. (2007). Observations: Changes in snow, ice and frozen ground, *in* S. Solomon, D. Qin, M. Manning, Z. Chen, M. Marquis, K. Averyt, M. Tignor and H. Miller (eds), *Climate Change 2007: The Physical Science Basis. Contribution of Working Group I to the Fourth Assessment Report of the Intergovernmental Panel on Climate Change*, Cambridge University Press, Cambridge, United Kingdom and New York, USA, pp. 337–384.

Li, F. and Goldstein, R. (1990). Studies of multibaseline spaceborne interferometric synthetic aperture radars, *IEEE Transactions on Geoscience and Remote Sensing* **28**(1): 88–97.

Lythe, M., Vaughan, D. and the BEDMAP Group (2001). Bedmap: A new ice thickness and subglacial topographic model of antarctica, *Journal of Geophysical Research: Solid Earth* **106**(B6): 11335–11351.

Marino, A. (2012). Synthetic aperture radar, *A New Target Detector Based on Geometrical Perturbation Filters for Polarimetric Synthetic Aperture Radar (POL-SAR)*, Springer Theses, Springer Berlin Heidelberg, pp. 9–27.

Massom, R. and Lubin, D. (2006). *Polar Remote Sensing*, Vol. II- Ice Sheets of *Springer Praxis Books. Geophysical Sciences Series*, Springer.

Massonnet, D. and Feigl, K. (1998). Radar interferometry and its application to changes in the earth's surface, *Reviews of Geophysics* **36**(4): 441–500.

Massonnet, D., Rossi, M., Carmona, C., Adragna, F., Peltzer, G., Feigl, K. and Rabaute, T. (1993). The displacement field of the landers earthquake mapped by radar interferometry, *Nature* **364**: 138–142.

Matsuoka, K., Pattyn, F., Callens, D., Conway, H. et al. (2012). Radar characterization of the basal interface across the grounding zone of an ice-rise promontory in east antarctica, *Annals of glaciology* **53**(60): 29.

Mohr, J. J. and Madsen, N. S. (1997). Multi-pass interferometry for studies of glacier dynamics, *in* T.-D. Guyenne and D. D. (eds), *ERS SAR interferometry, Proceedings of the Fringe 96 Workshop, held in Zurich, Switzerland, 30 September-2 October 1996.*, Vol. 406, European Space Agency, Paris, pp. 345–352.

Neckel, N. (2010). *Surface velocities in the hinterland of the neumayer iii station (antarctica) derived from sar-interferometry*, Master's thesis, Universitat Heidelberg.

NEEM community members (2013). Eemian interglacial reconstructed from a greenland folded ice core, *Nature* **493**: 489–494.

Padman, L., Fricker, H. A., Coleman, R., Howard, S. and Erofeeva, L. (2002). A new tide model for the antarctic ice shelves and seas, *Annals of Glaciology* **34**(1): 247–254.

Pattyn, F. and Derauw, D. (2002). Ice-dynamic conditions of shirase glacier, antarctica, inferred from ers sar interferometry, *Journal of Glaciology* **48**(163): 559–565.

Raney, R. (2005). Synthetic aperture radar systems, *in* M. Schwartz (ed.), *Encyclopedia of Coastal Science*, Encyclopedia of Earth Science Series, Springer Netherlands, pp. 937–939.

Richards, J. (2009). *Remote Sensing with Imaging Radar*, Signals and Communication Technology, Springer-Verlag Berlin Heidelberg.

Rignot, E., Mouginot, J. and Scheuchl, B. (2011a). Antarctic grounding line mapping from differential satellite radar interferometry, *Geophysical Research Letters* **38**(10).

Rignot, E., Mouginot, J. and Scheuchl, B. (2011b). Ice flow of the antarctic ice sheet, *Science* **333**(6048): 1427–1430.

Rignot, E., Mouginot, J. and Scheuchl, B. (2011c). MEaSUREs InSAR-based antarctica ice velocity map, Boulder, Colorado USA: National Snow and Ice Data Center. Digital media.

Rignot, E., Mouginot, J. and Scheuchl, B. (2011d). MEaSUREsantarctic grounding line from differential satellite radar interferometry, Boulder, Colorado USA: National Snow and Ice Data Center. Digital media.

Rogers, A. and Ingalls, R. (1969). Venus: Mapping the surface reflectivity by radar interferometry, *Science* **165**(3895): 797–799.

Rosen, P., Hensley, S., Joughin, I., Li, F., Madsen, S., Rodriquez, E. and Goldstein, R. (2000). Synthetic aperture radar interferometry, *Proceedings of the IEEE* **88**(3): 333–382.

Rott, H. (2009). Advances in interferometric synthetic aperture radar (insar) in earth system science, *Progress in Physical Geography* **33**: 769–791.

Schmeltz, M., Rignot, E. and Macayeal, D. R. (2001). Ephemeral grounding as a signal of ice-shelf change, *Journal of Glaciology* **47**(156): 71–77.

Shepherd, A. and Wingham, D. (2007). Recent sea-level contributions of the antarctic and greenland ice sheets, *science* **315**(5818): 1529–1532.

Simons, M. and Rosen, P. (2007). Interferometric synthetic aperture radar geodesy, *in* G. Schubert (ed.), *Treatise on Geophysics*, Vol. 3-Geodesy, Elsevier Press, pp. 391–446.

Smith, B. (2012). personal communication.

Wegmüller, U. and Werner, C. (2007). *Interferometric SAR Processing, Documentation-Theory.*, GAMMA remote sensing. Version 1.0.

Wegmüller, U. and Werner, C. (2008). *Differential Interferometry, Documentation – User's Guide.*, GAMMA remote sensing. Version 1.2.

Wegmüller, U. and Werner, C. (2010a). *Geocoding and Image Registration. Documentation – User's Guide.*, GAMMA remote sensing. Version 1.5.

Wegmüller, U. and Werner, C. (2010b). *Interferometric SAR Processing, Reference Manual.*, GAMMA remote sensing.

Zebker, H. A. and Goldstein, R. M. (1986). Topographic mapping from interferometric synthetic aperture radar observations, *Journal of Geophysical Research: Solid Earth* **91**(B5): 4993–999.

Zebker, H. A. and Villasenor, J. (1992). Decorrelation in interferometric radar echoes, *IEEE Transactions on Geoscience and Remote Sensing* **30**(5): 950–959.

Zebker, H., Rosen, P. A., Goldstein, R. M., Gabriel, A. and Werner, C. L. (1994). On the derivation of coseismic displacement fields using differential radar interferometry: The landers earthquake, *Journal of Geophysical Research: Solid Earth* **99**(B10): 19617–19634.

Zhou, X., Chang, N.-B. and Li, S. (2009). Applications of sar interferometry in earth and environmental science research, *Sensors* **9**(3): 1876–1912.

Zisk, S. (1972). A new, earth-based radar technique for the measurement of lunar topography, *The moon* **4**: 296–306.

Appendix A

Complex numbers

This appendix about complex numbers is massively inspired from Richards (2009, pp.321-325). Complex numbers are convenient tool to deal with some quantities used in radar imaging, especially to depict electromagnetic energy sent by a sensor and backscattered to it.

The theory of complex numbers is based on the symbol i that describes the square root of minus one.[1]

$$i = \sqrt{-1} \ \ or \ \ i^2 = -1$$

The i enables to express the square root of any negative number.

For instance, $\sqrt{-16} = \sqrt{16 \times -1} = \sqrt{16}.\sqrt{-1} = 4i$ or $\sqrt{-12} = \sqrt{-1 \times 3 \times 4} = 2i\sqrt{3}$

In the two previous examples, the numbers multiplying the i (4 and $2\sqrt{3}$) are called *imaginary numbers* and have to be differentiated from the real numbers: those that are not associated with the symbol i (e.g. 24, -89, $\sqrt{23}$...) and that are used for counting real things.

A *complex numbers*, z, is a number made of two parts : a real part, $a = \mathcal{Re}\{z\}$, and an imaginary part, $b = \mathcal{Im}\{z\}$. A complex number can therefore be expressed like this:

$$z = a + bi$$

Addition and subtraction of complex numbers correspond simply to the addition and

---

[1]The symbol i is used in mathematics while j is sometimes preferred by physicists to avoid confusion with the symbol for current.

the subtraction of their components:

$$z_1 \pm z_2 = (a_1 \pm a_2) + (b_1 \pm b_2)i$$

Multiplication and division give however a less convenient form due to the distributive properties in arithmetics:

$$z_1 z_2 = (a_1 + b_1 i)(a_2 + b_2 i) = (a_1 a_2 - b_1 b_2) + (a_1 b_2 + a_2 b_1)i$$

$$\frac{z_1}{z_2} = \frac{a_1 + b_1 i}{a_2 + b_2 i} = \frac{(a_1 + b_1 i)(a_2 - b_2 i)}{(a_2 + b_2 i)(a_2 - b_2 i)} = \frac{1}{a_2^2 + b_2^2}[a_1 a_2 + b_1 b_2 + (a_2 b_1 - a_1 b_2)i]$$

A complex number is usually represented on a plane with Cartesian coordinates where a, the real part, corresponds to the abscissa and b, the imaginary part to the ordinate. This graph is represented on figure A.1 and is called the *Argand diagram*.
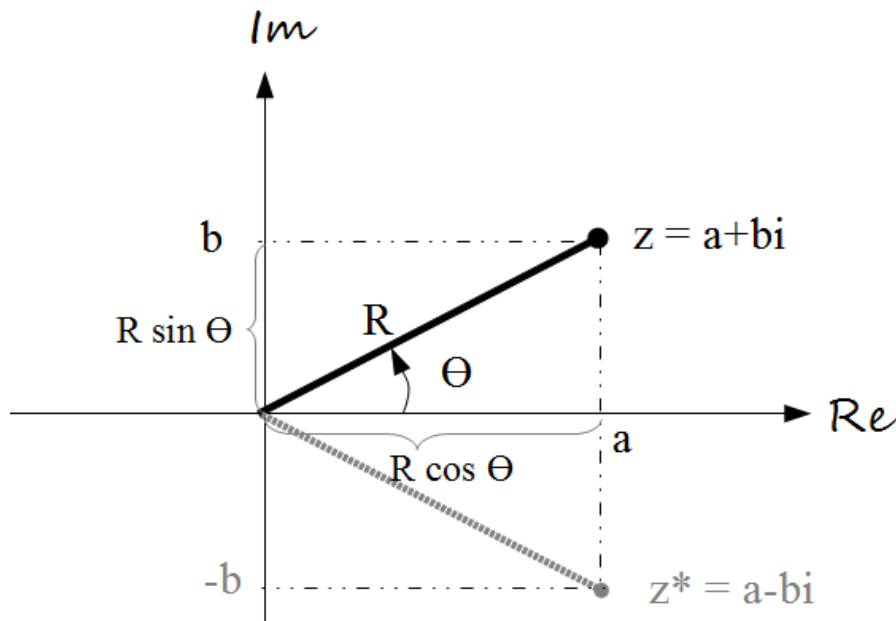

Figure A.1: <u>Argand diagram</u> is used to graphically represent complex numbers. The abscissa corresponds to the real axis whereas the imaginary part of the number is represented on the ordinate. The complex conjugate (z^*) is also represented.

From figure A.1, it is easy to convert Cartesian coordinates in their polar form. Polar coordinates depend on two parameters : R, the length of the vector from the origin or the **modulus** and θ, the **argument**, that is the angle measured up from the positive abscissa.

Polar components can easily be related to Cartesian coordinates:

$$R = \sqrt{a^2 + b^2} \;\; and \;\; \theta = \tan^{-1}\frac{b}{a} \tag{A.1}$$

On the contrary, we can also transform Cartesian coordinates into their polar form :

$$a = R\cos\theta \;\; and \;\; b = R\sin\theta \tag{A.2}$$

We can now deduce from equation (A.2) that a complex number can be written in different forms

$$z = a + bi = R(\cos\theta + i\sin\theta) \tag{A.3}$$

The use of Maclaurin's power series expansion of sine and cosine functions :

$$\sin\theta = \theta - \frac{\theta^3}{3!} + \frac{\theta^5}{5!} - \frac{\theta^7}{7!} - \ldots$$

$$\cos\theta = 1 - \frac{\theta^2}{2!} + \frac{\theta^4}{4!} - \frac{\theta^6}{6!} + \ldots$$

leads to the following relationship:

$$\cos\theta + i\sin\theta = 1 + i\theta - \frac{\theta^2}{2!} - i\frac{\theta^3}{3!} + \frac{\theta^4}{4!} + i\frac{\theta^5}{5!}\ldots \tag{A.4}$$

Knowing that Maclaurin's power series expansion for the exponential function gives :

$$e^x = 1 + x + \frac{x^2}{2!} + \frac{x^3}{3!} + \frac{x^4}{4!} + \ldots$$

If we simply replace x by ix, we find that

$$e^{ix} = 1 + ix - \frac{x^2}{2!} - \frac{x^3}{3!} + \frac{x^4}{4!} + \ldots \tag{A.5}$$

Putting equations (A.4) and (A.5) together, we get the following equality :

$$\cos\theta + i\sin\theta = e^{i\theta} \tag{A.6}$$

This is known as the *Euler's theorem.* As a result, a complex number can also be expressed

in an exponential form :

$$z = Re^{i\theta} \qquad (A.7)$$

which is particularly useful for multiplying and dividing complex numbers, thanks to properties of exponential numbers. Thus, we have for these two operations:

$$z_1 z_2 = R_1 R_2 e^{i(\theta_1 + \theta_2)} \quad and \quad \frac{z_1}{z_2} = \frac{R_1}{R_2} e^{i(\theta_1 - \theta_2)}$$

As we can see, different ways of expressing complex numbers have various properties so that the form that will be used depends on the purpose and on the manipulation performed on the numbers. Exponential form is for instance very convenient for manipulating numbers while Cartesian form discriminates better real and imaginary parts.

It should finally be noted that for each complex number, its *complex conjugate* exists (cfr figure A.1). The only difference between a complex and its conjugate is that the signs of the imaginary components are inverted. As a consequence, if $z = a + bi$, its conjugate, denoted as z^* (with a superscript asterisk), will be $z^* = a - bi$. Graphically, this means that the angles θ and θ^* have the same amplitude with an opposite sign. That is why we have $z^* = Re^{-i\theta}$ if $z = Re^{i\theta}$. If conjugates play a very important role in electromagnetism and signal analysis field (Richards, 2009), this is partly because the multiplication of a number by its conjugate gives a very interesting result :

$$zz^* = RR^* e^{i0} = (a + bi)(a - bi) = a^2 + b^2 = R^2$$

The product of a complex and its conjugates leads thus to a real number equal to the square of its modulus.

In the radar field, most signals considered have a sinusoidal form[2]. Thanks to equation (A.6), these signals can be expressed with complex numbers. For this reason

$$\cos\theta = \mathcal{R}e\{e^{i\theta}\}$$

and a traveling sinusoid in direction x can be expressed as

$$\cos(kx - \omega t) = \mathcal{R}e\{e^{i(kx - \omega t)}\}$$

As long as we remember to take the real part of the result of any operation, the sinusoidal

---

[2]Or can be reduced to a sinusoid.

form can be replaced by the exponential, in orther to facilitate calculations.

Appendix B

Automation of the processing chain

In chapter 3, all the processing steps were detailed but it would take much time to get interferograms and displacement maps by running commands and their parameters each in its turn. For this reason, an automation script was implemented (Neckel, 2010). This script, called *DISP_3D.py* was written with the python programming language and its operational principle is described in figure B.1. The first step is to fill in the *SLC_list* which is a text file
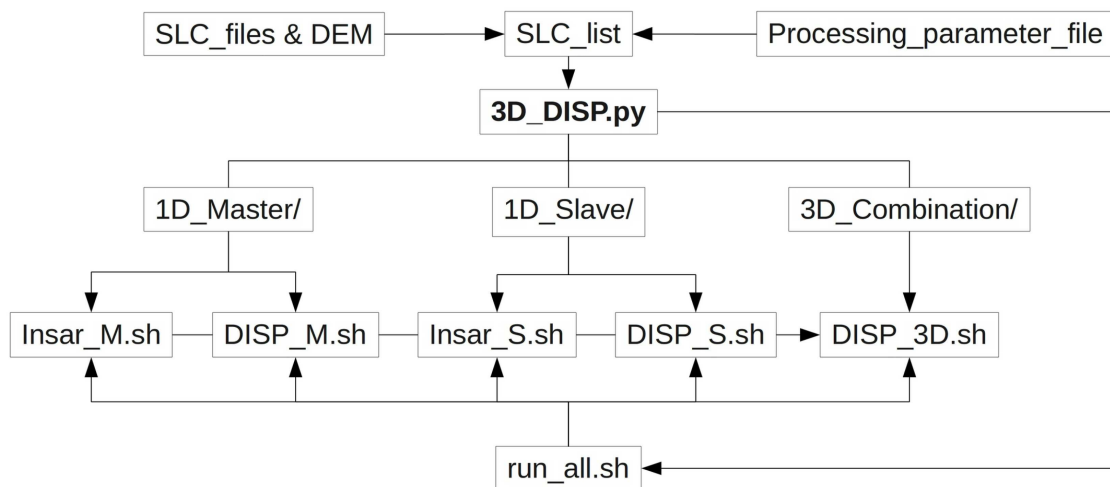

Figure B.1: Schematic structure of the python 3D_DISP.py automation script (Neckel, 2010, p.67)

needed as input parameter, to run the DISP_3D.py script. The SLC_list provides indeed essential information to the automation script. This includes names and abbreviations of SLCs to be processed and their location on the computer, as well as the DEM used and the name and link of the processing_parameter_file. The latter is a text file that contains all the essential parameters needed during the processing. Among others we can cite: the initial (coarse) offsets between SLC pairs and between interferometric pairs, correlation threshold,

temporal baseline, etc. This file is initialized at first with the default value contained in a standard file but the user can modify/update the parameters in the file along the way.

Once we have the SLC_list completed, we are able to run the DISP_3D.py script. It starts with the creation/update of the directory structure (denoted by a "/" in figure B.1). One folder is created for each SLC pair and each 3D combination of pairs. The folders for SLC pairs (1D_MASTER/ or 1D_SLAVE/) contain the shell scripts[1] *Insar.sh* and *DISP.sh*. The first one aims at performing the interferometric (InSAR) processing, whereas the second shell script, DISP.sh, manages the differential interferometic processing (DInSAR) and the geocoding. Once the processing of two compatible interferometric pairs is accomplished, it is possible to retrieve the 3D flowfield thanks to the *3D_DISP.sh* shell script, which is located in the combination directory. All the shell scripts use information provided by the parameter_file, and are based on GAMMA's pre-written automation scripts (in another programming language).

It should finally be noticed that, in theory, it is possible to run all the shell scripts from the unique commanding shell script *run_all.sh*.

---

[1]A shell script is a sequence of linux commands stored in a file. The commands are written in linux programming language, which means that they are designed to be executed in a terminal.